This contribution has been published in *Mol. Syst. Des. Eng.*, **2020**, *5*, 820-828 (link)

Competitive hydrogen bonding in supramolecular polymerizations of tribenzylbenzene-1,3,5-tricarboxamides

Mathijs F.J. Mabesoone,[a†] Sinan Kardas,[a,b†] Héctor Soria-Carrera,[c] Joaquín Barberá,[c] Jesús M. de la Fuente,[c] Anja R.A. Palmans,*[a] Mathieu Fossépré,[b] Mathieu Surin,*[b] and Rafael Martín-Rapún* [c,d]

[a.] Laboratory of Macromolecular and Organic Chemistry and Institute for Complex Molecular Systems. Eindhoven University of Technology. Eindhoven (The Netherlands). E-mail: A.Palmans@tue.nl

[b.] Laboratory for Chemistry of Novel Materials. Center of Innovation and Research in Materials and Polymers. University of Mons–UMONS E-mail: Mathieu.Surin@umons.ac.be

[c.] Department of Organic Chemistry - Instituto de Ciencia de Materiales de Aragón. University of Zaragoza-CSIC. Zaragoza (Spain) E-mail: rmartin@unizar.es

[d.] Instituto de Nanociencia de Aragón. University of Zaragoza. Zaragoza (Spain)

† These authors contributed equally

Abstract

Despite numerous reports on nucleated supramolecular polymerization, the molecular origin of the properties of these supramolecular polymers remains overlooked. Here, the formation of fibers formed by self-assembly of *N*,*N*',*N*''-tris(alkoxybenzyl)benzene-1,3,5-tricarboxamides (benzylBTAs) has been studied using both simulations and experimental techniques. The simulations show that the fibers exhibit a dynamic behavior with stacking defects that appear and propagate differently depending on the BTA molecular structure. To validate theoretical results, a library of eight tris(alkoxybenzyl) BTAs has been synthesized to compare their supramolecular polymerizations both in the bulk and in apolar solvents. We show that the molecular organization of monomers and dynamics of supramolecular polymers strongly depend on the number and position of the alkoxy substituents on peripheral phenyl rings. By combining theoretical results with experimental measurements, we elucidate the likely role of competitive hydrogen bonding between the central amides and peripheral ether moieties on the stacking behavior of BTAs and the dynamics of structural defects in supramolecular polymers. Our findings open up new design rules for these dynamic materials.

Introduction

To accelerate the application of supramolecular polymerizations in soft materials, control over the molecular organization is of paramount importance.[1] Material properties, such as conductivity and processability, are indeed dependent on the molecular structure of the monomers.[2,3] Unfortunately, prediction of the structure and stability of a supramolecular polymer remains challenging. Pathway complexity,[4] multiple polymer states[5–7] or kinetic trapping[8] pose significant challenges in rational design of material properties from monomer structures. Despite the challenges posed by these facets of supramolecular polymerizations, the competition between several polymerization pathways has given rise to promising

systems, such as living supramolecular polymers,[9–11] thermally bisignate polymerizations[12,13] and kinetically trapped states.[14,15]

Understanding of complex supramolecular polymerizations has been helped with computational approaches. The development of numerical models by among others van der Schoot,[16,17] ten Eikelder and Markvoort,[18–20] and Würthner[21,22] has given great insights into the thermodynamic properties of these supramolecular systems and provided rationales for some of their counterintuitive behavior.[23,24] In addition, MD simulations have given unrivalled atomistic insights into the network of interactions in supramolecular polymers in organic solvents[25–29] and hydrophobically collapsed structures in aqueous media.[30–32] Interestingly, dynamics of defects along the self-assembled BTA fibers have been pointed out thanks to the atomistic information coming from MD simulations.[33] These simulations enable a correlation of molecular features to the macroscopic properties of the materials. However, approaches that correlate microscopic insights from simulations with experimentally obtained material properties to arrive at general structure-property relationships are not commonplace.

To gain further insights into the way hydrogen bonding affects the structure and dynamics of supramolecular polymers, an efficient strategy would be to guide the design of supramolecular systems by systematic molecular modelling techniques. The factors that direct self-assembly and dynamics of supramolecular systems could thus be highlighted to propose structure-property relationships.

In the past, we and other have studied in detail the self-assembly properties of benzene-1,3,5-tricarboxamides (BTAs) **1** and of methylene bridged analogues **2** (Scheme 1) by a combination of experimental and computational studies. Computational studies on **1** have shed light on the molecular principles underlying its strongly cooperative supramolecular polymerization.[25,34,35] Combined experimental and computational studies have revealed

furthermore a subtle influence of the solvent on the geometry and stability of the supramolecular polymers of **1**.[36]

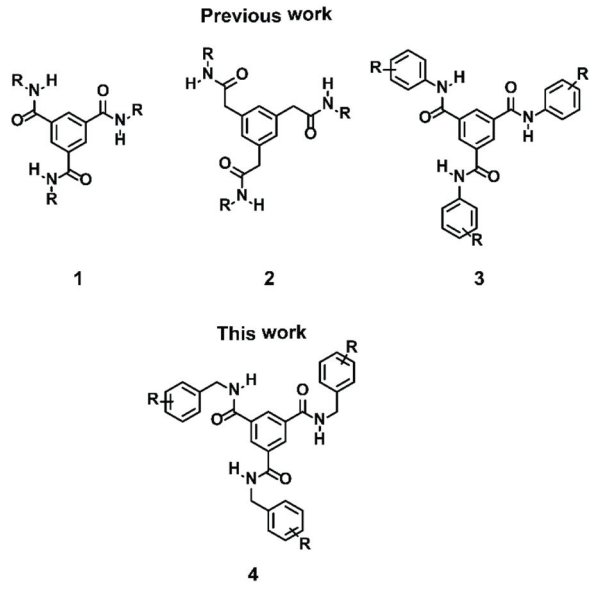

Scheme 1. Chemical structures of previously studied BTAs 1-3 and the BTA 4 studied in this work.

In contrast, when a methylene spacer is installed between the central benzene core and the amides in the conformationally flexible derivative **2**, a strong dependency on solvent structure has been observed.[28] Using a computational approach, this strong solvent dependency could be attributed to subtle differences in stabilization of various amide conformations. In a third structural variation, the addition of a phenyl ring between the soluble alkyl chains and the amide (derivative **3**) resulted in a complete loss of aggregation, presumably due to the loss in intermolecular hydrogen-bond formation.[37] The understanding of the molecular dynamics and how this impacts the experimentally observed behavior of BTA derivatives **1**-**3** prompted us to design a library of more conformationally flexible benzyl-BTA derivatives, **4**. Due to the methylene group between the central amides and peripheral phenyl group, derivatives of **4** were anticipated to be more prone to form intermolecular hydrogen bonds than **3** and therefore more likely to cooperatively self-assemble. The different effects of the number and position

of the alkoxy groups on the phenyl rings have been observed before but are not well understood for supramolecular polymerizations.[38–41] We systematically varied the position and number of alkoxy groups on the peripheral phenyl ring (Scheme 2) to obtain a more detailed understanding of the effect of these substitution patterns on the supramolecular structure. To permit the use of circular dichroism (CD) spectroscopy, which is a sensitive tool to assess the cooperativity and stability of supramolecular polymerizations, all substitution patterns have one representative comprising chiral, non-racemic (*S*)-3,7-dimethyloctyl side chains (**Cit-3**, **Cit-6**, **Cit-9** and **Sym-Cit-6**).

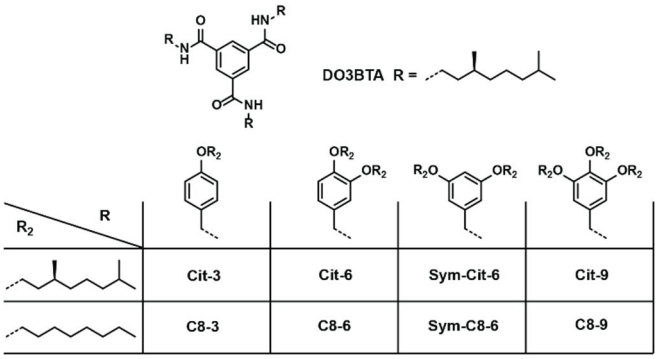

Scheme 2. Library of chiral and achiral alkoxybenzyl-substituted BTAs studied in this work.

Here, we put forward a comprehensive approach to relate the molecular structures to their self-assembly behavior, by starting from MD simulations and subsequently analyzing the systems experimentally. Our results show that the combined computational and experimental approach can elucidate counterintuitive, competitive hydrogen bonding patterns between the central amides and peripheral ethers, which considerably impact the stability of supramolecular polymers. These structure-property relationships may provide important guidelines towards a rational design of functional supramolecular polymers.

Results and discussion

Molecular dynamics simulations of benzyl-BTAs show competitive hydrogen bonding

MD simulations were carried out to evaluate the influence of lateral groups and fiber length on the supramolecular assembly and dynamics of benzyl-BTA fibers. To do so, we compared a model BTA-based compound, **DO3BTA**, with the series of compounds designed in this study (Scheme 2). BTA and benzyl-BTA fibers of 12- and 24-units long were built with an intercore distance between BTAs of 5 Å. Their geometries were initially optimized by energy-minimization, to be used as starting structures for MD simulations on a 500 ns timescale. In the early steps of the MD simulations, the intercore distances drop to 3.4 Å and the cores rotate relative to each other due to π-stacking and hydrogen bonding between BTA monomers. The fibers become helical and organize in short ordered segments of stacked BTAs with structural defects between these segments (see snapshots in Figure 1). These defects consist of minor misalignments and clear kinks that propagate along the MD simulations (Figure 2a). Each ordered segment is made of several BTAs and characterized by intercore distances of around 3.4 Å. For alkoxybenzyl-BTA derivatives, some peripheral phenyl rings are π-stacked in dimers, while alkoxy side chains protrude from the helical fibers and interdigitate between adjacent BTA units along a single fiber (Figure 1). The defects in the fibers are characterized by a large distance (> 4 Å) between centers of mass of pairs of adjacent BTAs (Figure S1) and small angles (well below 180°) between the centers of mass of three consecutive BTAs (Figure S2). A cartoon representation of the particularly disordered **Sym-Cit-6** fiber of 24 units is given in Figure 2a.

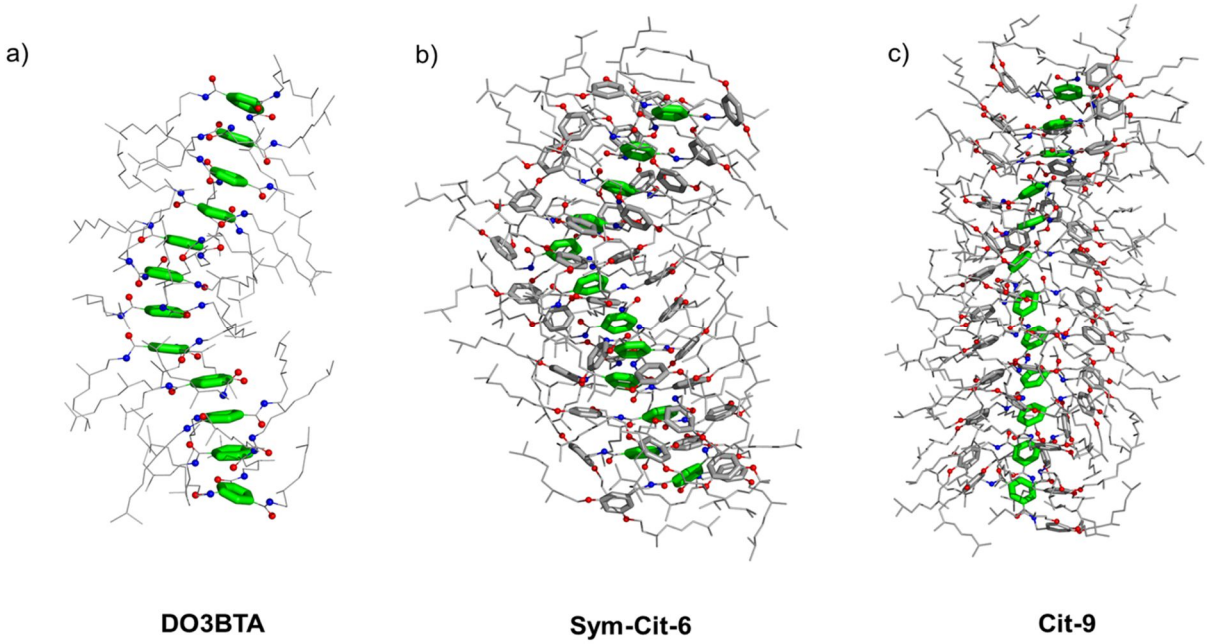

Figure 1. Snapshots extracted in the early steps of the MD simulations (taken at 1 ns) of 12-unit long fibers of **DO3BTA** (a), **Sym-Cit-6** (b) and **Cit-9** (c), showing the helical organization of the BTA cores (green sticks) and the interdigitation of the side chains (grey sticks for benzyl groups and grey lines for alkoxy chains). Oxygen and nitrogen atoms are depicted in red and blue, respectively.

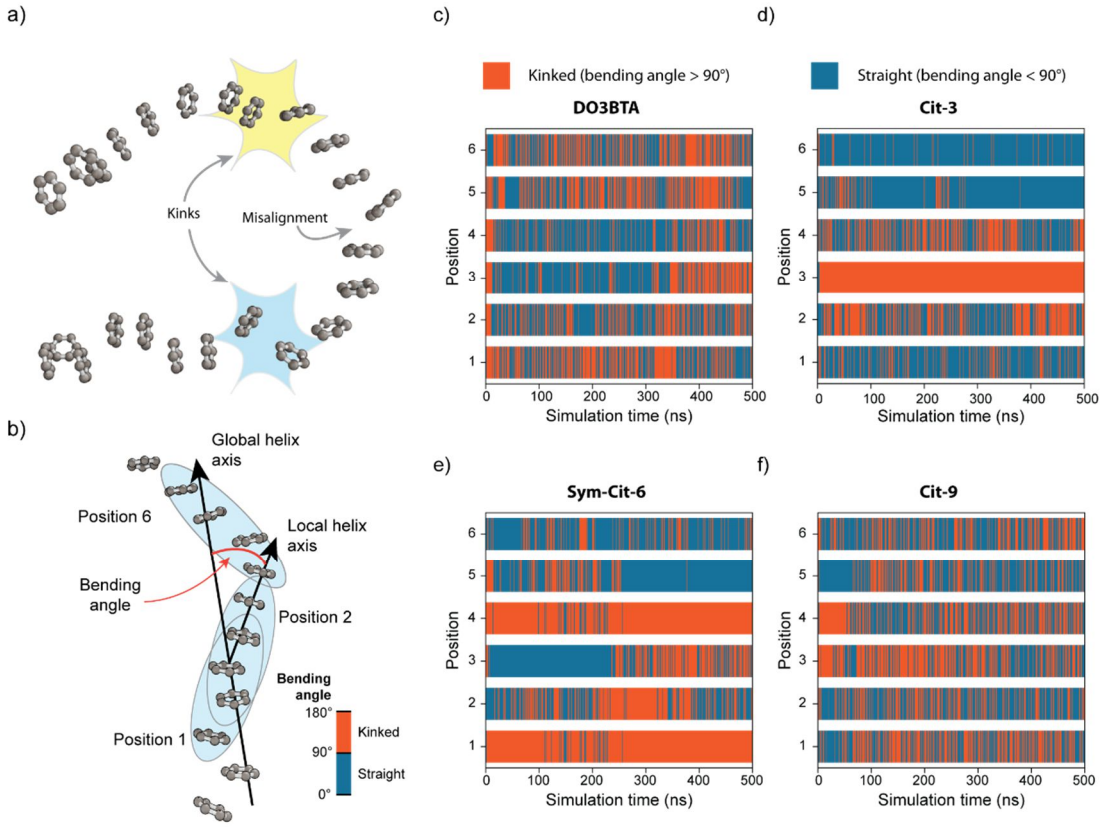

Figure 2. a) Snapshot of the MD simulation of the 24 units long fiber of **Sym-Cit-6** at 250 ns showing the presence of structural defects (minor misalignment, clear kink). Only the benzene cores are shown for clarity. b) The HELANAL-Plus software defines a global helix axis by fitting a helix to the entire fiber of BTAs. Similarly a local helix axis is defined for each position of a sliding window of four consecutive BTA cores, of which examples are indicated by the position markers. The bending angle corresponds to the angle between the global and local helix axes. The energy-minimized structure of BTA cores of the 12 units long fiber of **Sym-Cit-6** is shown. c-f) Evolution of the local bending angles for the 6 positions, as indicated in Figure 1b, as obtained from the HELANAL-Plus analysis over the course of the 500 ns MD simulation for **DO3BTA** (c), **Cit-3** (d), **Sym-Cit-6** (e) and **Cit-9** (f). Kinked regions appear through a binary color code of bending angles (BA): blue regions indicate straight sections of the fiber (BA < 90°), while red regions indicate kinked sections (BA > 90°).

The kinks observed in the simulations are localized in sections of the fibers with large bending angle compared to the helix axis (Figure 2b), as estimated with the helical analysis software HELANAL-Plus[42] (see Computational Details in the Supporting Information for the details).

The results of these analyses (Figure 2c-f, Figure S3,4) show two types of information: a sequential information (Y axis, where does the kink appear in the fiber?), and a temporal information (X axis, when does the kink appear during the simulation?). Interestingly, the number of persistent kinks depends on the monomer structure. For the **DO3BTA** model compound, there is a random alternation between straight sections (Figure 2c, ordered segments in dark blue) and kinked sections (Figure 2c, structural defects in red) along the fiber. The kinked and straight sections are interchanging on a timescale ranging from a few ns to tens of ns. Remarkably, the introduction of the alkoxy moieties in the benzyl-BTA derivatives appears to introduce clear structural defects in the fibers. In contrast to fibers of **DO3BTA**, fibers of **Cit-3** and **Sym-Cit-6** (Figures 2d and e) show relatively short straight (dark blue) sections separated by persistent kinks (red continuous lines) in the middle of the fiber and at positions 1 and 4, respectively. Fibers of **Cit-9** (Figure 2f), which have the highest degree of alkoxy substitution on the peripheral phenyl rings, do not show any persistent kinks. Similar, yet less pronounced results are obtained in the simulations of the supramolecular polymers composed of 24 BTAs or benzyl-BTAs (Figure S4).

The results obtained from the HELANAL-Plus analysis show that the steric hindrance imposed by a high number of alkoxy groups on the peripheral phenyl rings of **Cit-9** reduces the possibility of fibers to kink. This different behavior likely arises from the larger steric hindrance between adjacent chiral alkoxy side chains in **Cit-9** compared to the **Sym-Cit-6** and **Cit-3**. In the case of **Cit-9**, the possibility of the benzyl-BTA units to tilt out of the columnar axis is reduced, resulting in dynamic, but relatively ordered supramolecular polymers.

The striking difference between the structural dynamics of the defects is encoded into the structure of the benzyl-BTAs. To investigate the origin of kinks in the fibers, we examined persistent hydrogen bonds which are present at least 90% of the MD time. Figure 3 reports the number of hydrogen bonds in the different BTA fibers averaged over the entire MD

simulation. The fibers of **DO3BTA** possess the highest number of hydrogen bonds: around 32 hydrogen bonds of the maximum of 33 hydrogen bonds in a fiber of 12 BTA units. Fibers of benzyl-BTAs with the alkoxybenzyl periphery tend to have less amide-amide hydrogen bonds. Rather unexpectedly, however, a considerable number of hydrogen bonds between the central amides and the peripheral ether moieties were observed. These hydrogen bonds, which have an average length of approximately 3.3 Å, are slightly longer than the amide-amide hydrogen bonds, which have an average length of 3.1 Å, which is typical for such hydrogen bonds.[32]

The amide-ether hydrogen bonds are persistently present at kink sites (*vide supra*), where a fraction of the amide-amide hydrogen bonds is broken (Figure 3a, Figure S5). Although a small number of non-persistent amide-ether hydrogen bonds may also be present in straight portions of the fibers, the strong correlation between the amide-ether hydrogen bond and a structural defect strongly suggests kinking of the fiber is related to the amide-ether hydrogen bond.

The presence of the amide-ether hydrogen bonds in the benzyl-BTAs can explain the above described differences in dynamic behavior between the various compounds. When going from polymers of **Cit-3** to **Sym-Cit-6**, the number of amide-ether hydrogen bonds increases as the peripheral phenyl rings have more alkoxy substituents which are, in addition, better positioned to interact with the amide groups at the central phenyl ring. This higher number of amide-ether hydrogen bonds correlates with the higher number of defects in **Sym-Cit-6** polymers. In contrast, fibers of **Cit-9**, which possess the highest number of alkoxy side chains, yet the lowest number of defects, concomitantly show the lowest number of amide-ether hydrogen bonds. Interestingly, this difference is less pronounced in the results obtained for **Cit-9** polymers of 24 units (Figure 3c), where the average of 5.5 amide-ether intermolecular hydrogen bonds is much higher than the double value obtained for a fiber of 12 units (2 x 0.7

in average). In other words, in the 24 units long fiber of **Cit-9** fiber, amide-ether intermolecular hydrogen bonds occur at a higher extent, but there are still less of these competitive hydrogen bonds than in case of **Sym-Cit-6**.

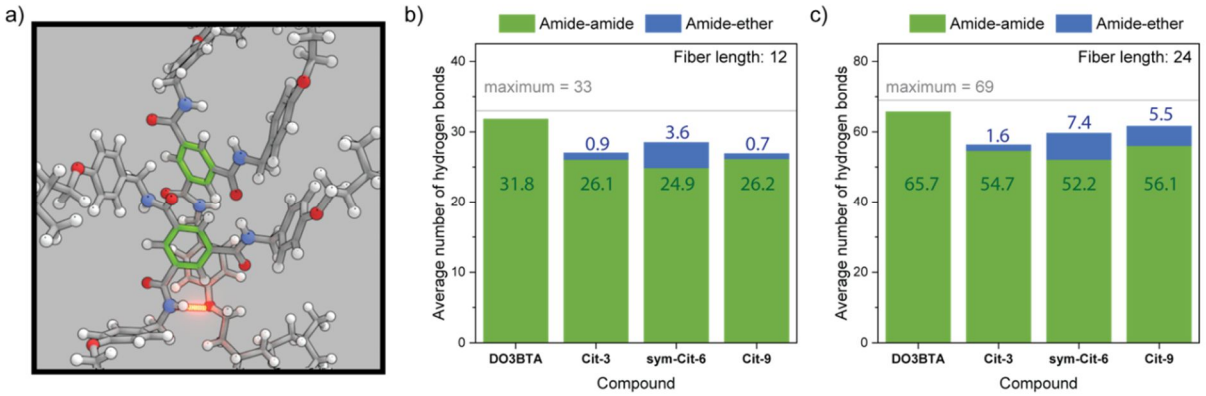

Figure 3. a) Cartoon representation of the **Cit-3** simulation with 24 units at 40 ns, showing the highlighted amide-ether hydrogen bond. The aromatic cores of the two benzyl-BTAs are highlighted in green. b, c) The number of amide-amide and amide-ether H-bonds averaged over the entire simulation for fibers of 12 BTAs (b) and 24 BTAs (c).

Analysis of the MD results indicates that an increasing number of alkoxy substituents that are well-positioned on peripheral phenyl rings increases the number of defects in the fibers as a consequence of competitive amide-ether hydrogen bonds becoming more likely. However, for the fibers of **Cit-9,** which possess three alkoxy chains per benzyl group, the formation of amide-ether hydrogen bonds is counterbalanced, possibly due to additional steric effects which reduce the possibility of the fiber to kink. All in all, the number of solubilizing alkoxy chain in the periphery of benzyl-BTAs need to be considered in the design of molecules as they induce competitive hydrogen-bonding interactions into the system. Using these computationally derived design rules, the stability of the supramolecular polymers can be controlled, as our experimental results show in the next section.

Experimental studies confirm computationally observed trends

To test whether MD simulations accurately predict the different degrees of ordering for the different compounds, the eight benzyl-BTA derivatives were extensively studied both in the

bulk and in solution. All benzyl-BTAs were synthesized according to the procedures described in the Schemes S1-S4 in the Supporting Information and obtained in excellent purity (full characterization in the Supplementary Information).

The results obtained for **Cit-3** clearly show that the *para*-alkoxy substituted derivatives form supramolecular polymers both in the solid state as well as in solution. Similar to trisalkyl BTAs, **Cit-3** and **C8-3** are thermotropic liquid crystals.[43] Polarized optical microscopy (POM) results show that **Cit-3** and **C8-3** exhibit a pseudo-focal conic texture upon slow cooling from the isotropic liquid, indicating the presence of a columnar liquid crystal phase (Figure S6). X-ray diffraction (XRD) measurements allow us to confirm the ordered columnar phases, with an interdisc distance of 3.5 Å as was previously reported for trisalkyl BTAs (Table S1).[44]

Table 1. NH-stretch and CO-stretch frequencies [cm^{-1}] obtained from bulk IR measurements and transition temperatures [°C] and corresponding enthalpies [kJ mol^{-1}] of BTAs obtained by DSC measurements.[a]

Compound[a]	$\nu_{NH\text{-}stretch}$ (cm^{-1})	$\nu_{CO\text{-}stretch}$ (cm^{-1})	Thermal behavior
Cit-3	3231	1637	C 62 (1.7) Col_{ho} 182 (8.8) I
C8-3	3244	1638	C 123 (13.3) Col_{ro} 185 (15.6) I
Cit-6	3237	1636	Col_{ho} 133 (17.3) I
C8-6	3262	1647	C 55 (9.2) Col_{ho} 151 (16.0) I
Sym-Cit-6	3331	1667	I
Sym-C8-6	3329	1664	g 23 I
Cit-9	3317	1662	I
C8-9	3230	1649	Col_{ho} 88 (10.0) I

[a] All DSC data derived from the second heating run. g = isotropic glass. C = crystalline phase; Col_{ro} = rectangularly ordered columnar phase; Col_{ho} = hexagonally ordered columnar phase; I=isotropic phase.

Table 2. IR frequencies [cm^{-1}] of the NH-stretch and CO-stretch vibrations of the BTAs obtained in 250 μM MCH and $CHCl_3$ solutions. Full spectra are given in Figures S8-11.

Compound	$\nu_{NH\text{-}stretch}$ (cm^{-1})		$\nu_{CO\text{-}stretch}$ (cm^{-1})	
	MCH	$CHCl_3$	MCH	$CHCl_3$
Cit-3	3229	3448	1640	1666
Cit-9	3315	3447	1665	1666
C8-9	3322	3447	1666	1666
Cit-6	3326	3443	1663	1663
C8-6	3318	3445	1664	1663
Sym-Cit-6	3321	3445	1667	1665
Sym-C8-6	3331	3445	1666	1666

The enthalpies associated to the mesophase to isotropic liquid transitions, 8.8 and 15.6 $kJ \cdot mol^{-1}$, are similar to those observed for trisalkyl BTAs (12-17 $kJ \cdot mol^{-1}$).[43] This similarity indicates that the structure of the mesophases could be equivalent, and consist of a 2D packing of one dimensional fibers, which are each stabilized through helical arrays of threefold hydrogen bonding.[44]

The IR spectra in the bulk provide further support for the presence of a threefold hydrogen-bonded helical array, with NH-stretch and CO-vibrations around 3240 and 1640 cm^{-1} respectively. The vibrations at those wavenumbers are very indicative of the formation of strong, triple helical hydrogen bonds (Table 1). The same absorption bands are observed for **Cit-3** in methylcyclohexane (MCH) solution showing that the one-dimensional fibers are stable in MCH and possess a similar structure as observed in the bulk. The results in chloroform ($CHCl_3$) solutions show a shift of the NH and CO stretch vibrations to higher

wavenumbers (Table 2), indicating that in $CHCl_3$, the hydrogen bonds are disrupted. Interestingly, the high degree of ordering that is enabled by the aliphatic side chain of **C8-3** renders this compound insoluble in MCH. Since the insolubility impairs further detailed analysis of the structures in solution, we decided not to further investigate this compound.

The strong hydrogen bonding and highly ordered columnar packing in the supramolecular polymers of **Cit-3**, as observed in the IR results, is further illustrated in the variable temperature CD (VT-CD) and variable temperature UV (VT-UV) experiments (Figure 4a, Figure S12). At temperatures above 87 °C, **Cit-3** is molecularly dissolved in 50 µM solutions in MCH. Upon cooling the solutions below this temperature, a sharp onset of the CD signal is observed, indicating that ordered supramolecular polymers are formed via a very cooperative process. By fitting the cooling curves of three different concentrations simultaneously to a thermodynamic mass-balance model of a nucleated supramolecular polymerization (Figure S18), we determined the enthalpy of elongation and nucleation of **Cit-3** at −71 $kJ \cdot mol^{-1}$ and −54 $kJ \cdot mol^{-1}$ and the entropy of elongation at −117 $J \cdot mol^{-1} \cdot K^{-1}$ and the cooperativity parameter, σ, at 293 K of $9.3 \cdot 10^{-4}$. The cooperativity in the supramolecular polymerization of **Cit-3** is in good agreement with the presence of intermolecular hydrogen bonding in solution as shown by IR measurements.[45,46]

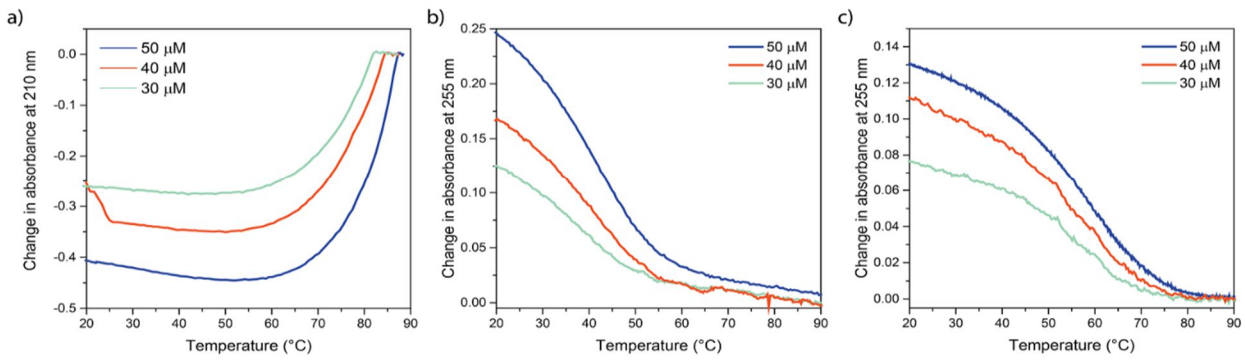

Figure 4 VT-CD results obtained for **Cit-3** (a), **Cit-9** (b) and **C8-9** (c) at various concentrations in MCH.

C8-9 and **Cit-9** exhibit a different behavior from **C8-3** and **Cit-3**. Although **C8-9** is a liquid crystal at room temperature, its clearing point is 94 K lower than the clearing point of **C8-3,** as generally occurs upon increasing the number of flexible alkyl chains in the periphery of discotic molecules. The mesophase can be assigned as ordered columnar hexagonal based on the weakly birefringent pseudo-focal conic texture by POM, and the X-ray diffraction pattern (Table S1). Branching in the alkyl chains further destabilizes the mesophase for **Cit-9**, which is an isotropic liquid. Consistently, IR measurements in the bulk show the formation of supramolecular polymers in bulk for **C8-9**, as indicated by the NH and CO stretch vibrations around 3240 and 1650 cm^{-1}, but not for **Cit-9** (Table 1). If present, the amide-amide intermolecular hydrogen bonds are even weaker in solution as shown by the NH and CO stretch vibrations around 3320 and 1665 cm^{-1} even for **C8-9** in MCH (Table 2).

In line with the observations made in bulk and concentrated solutions, VT-CD and UV experiments of **Cit-9** and VT-UV **C8-9**, where the wavelength of maximum CD intensity of **Cit-9** is followed, indicate that supramolecular polymers are formed only in a weakly cooperative manner (Figure 4b, c, Figures S13, S18). By fitting the data to the model, the enthalpy and entropy of elongation of **Cit-9** are determined at −72 $kJ \cdot mol^{-1}$ and −144 $J \cdot mol^{-1} \cdot K^{-1}$ and at −61 $kJ \cdot mol^{-1}$ and −100 $J \cdot mol^{-1}\ K^{-1}$ for **C8-9**. The cooperativity parameter, σ, of both compounds is determined at 0.04 and 0.03, respectively, at 293 K. The larger entropic penalty of polymerization of **Cit-9** presumably reflects the loss of entropy resulting from the organization of the larger number of alkoxy chains, while the higher value of σ suggests that polymers of **Cit-9** are shorter than the polymers of **Cit-3** under similar conditions.[47] Similar observations on the effect of cooperativity and stability on peripheral substitution patterns in BTA derivatives has also been observed in related compounds.[41]

Sym-Cit-6 and **Sym-C8-6**, which were obtained as viscous liquids, did not show signs of hydrogen bonding either in the solid state or in MCH solutions as shown by the wavenumbers

of the NH and CO stretch vibrations (Tables 1 and 2). Accordingly, the compounds were isotropic under POM and no transitions could be observed by DSC or by VT-UV and CD (Figures S14, 16). Liquid crystallinity has been rarely reported for discotic compounds with a 3,5-substitution pattern compared to 3,4,5- or 3,4-substitution patterns.[48] Therefore, we also synthesized the 3,4-disubstituted analogues **Cit-6** and **C8-6**. For those compounds, POM shows a clear pseudo-focal conic texture at high temperatures, indicating the presence of a columnar liquid crystal phase. The isotropization temperature is lower than for **C8-3** and **Cit-3** but higher than for **C8-9** and **Cit-9** showing that the mesophase is intermediate in stability. However, the transition enthalpy is similar to **C8-3** and to trisalkyl BTAs suggesting the structure of the mesophase could be also the same. Indeed, the mesophase can be assigned as ordered columnar hexagonal based on XRD measurements on shear aligned samples (Figure S7). First, a set of equatorial reflections is observed in the small angle region with spacings in the reciprocal ratio 1:√7:√12, compatible with a 2D hexagonal lattice. Second, a sharp arc is centered on the meridian and corresponds to 3.5 Å, which is the typical stacking distance in ordered columnar mesophases. The diffuse halo that results from the aliphatic tails shows a four-spot pattern as previously reported for trisalkyl BTAs.[44]

Consistently, strong hydrogen bonding can be observed in the solid-state IR spectra, indicated by the NH and CO stretch vibrations for **Cit-6** and **C8-6** at 3237 and 3262 cm^{-1} and 1636 and 1647 cm^{-1}, respectively (Table 1). Interestingly however, in MCH solutions, no triple helical hydrogen bonding can be observed in the IR spectrum, with the NH and CO stretch vibrations for **Cit-6** and **C8-6** at 3326 and 3318 cm^{-1} and 1663 and 1664 cm^{-1}, respectively, indicating a low degree of order in the hydrogen bonds (Table 2). The inability to form supramolecular polymers in solution is also reflected by the absence of a polymerization that is observable by VT-CD and VT-UV experiments (Figure S15, 17).

Comparison of computational and experimental results

The results obtained from the bulk and solution state experiments confirm the trends of the different monomers that are observed in the MD simulations. Most notably, the MD simulations show that the central amides form hydrogen bonds with the ethers at the periphery, inducing kinks between ordered segments within the fibers. Interestingly, the number of defects appears to be regulated by a balance between the number and position of the ether moieties and the steric bulk at the periphery of the fibers.

The trends observed in the computational results rationalize the experimental data. **Cit-3** shows a relatively low number of amide-ether hydrogen bonds as well as a low number of persistent kinks throughout the simulation. This observation of a very ordered fiber is in line with the strong CD signal observed for this compound, as well as the high elongation temperature and cooperative self-assembly behavior. In addition, the IR spectra show that the amides form strong hydrogen bonds organized in a triple helical fashion in both bulk and MCH solutions, which corroborates the computational results.

The behavior of the dialkoxy-substituted benzyl-BTA derivatives is considerably different. The simulations of **Sym-Cit-6** show the highest number of amide-ether hydrogen bonds and the highest number of defects of all compounds simulated. Consequently, the ordered segments in these polymers are the shortest, in accordance with the complete absence of supramolecular polymers in solution or bulk in the conditions measured. The increased number of ether groups and their closer proximity to the central amides explain why the amide-ether hydrogen bonding can occur efficiently. Destabilization of the polymeric aggregates by these hydrogen bonds disrupts the integrity and stability of the polymer. As a result, **Sym-Cit-6** cannot form stable supramolecular polymers.

Surprisingly, the derivative that contains most ether moieties, **Cit-9**, shows only an intermediate amount of amide-ether hydrogen bonds in the simulations. The IR spectra of **Cit-**

9 in turn do not indicate that strong, helically organized hydrogen bonds are formed in either solution or the solid state, as was observed for **Cit-3**. These results suggest that the moderate amounts of competitive hydrogen bonding of the amides with the ether groups may indeed interfere in the ordering of the supramolecular polymer. Despite the absence of helical hydrogen bonds, supramolecular polymers are present in solution, albeit with lower thermal stability and cooperativity than the polymers of **Cit-3**. The low degree of order in the supramolecular polymers is additionally reflected in the low CD intensity that these systems display. Nonetheless, the ability of **Cit-9** and **C8-9** to form polymers indicates that π-stacking also considerably contributes to the stability of the supramolecular polymers and that a balance between various hydrogen-bonding patterns and π-stacking determines the stability of the supramolecular polymers.

Together, the computational and experimental results show that amide-ether intermolecular hydrogen bonds, which compete with the amide-amide intermolecular hydrogen bonds, can significantly alter the stability and order of the supramolecular polymers. We propose that balancing these interactions may provide an avenue to tailor the stability and thermal properties in these non-covalent systems.

Conclusions

Despite the progress achieved in understanding the formation of supramolecular polymers, relationships between the molecular features of the monomers and stabilities of the supramolecular polymers still remain elusive. To arrive at design rules for tunable stability in supramolecular polymerizations, insights gained from molecular simulations are to be combined with experimental studies. Here, we performed MD simulations on a series of tribenzyl-substituted benzene-1,3,5-carboxamide derivatives decorated with alkoxy-substituted benzyl moieties. The MD simulations show that, in comparison to the previously

well studied 1,3,5-trialkyltricarboxamides, the alkoxybenzyl-BTAs organize in dynamic fibers with stacking defects such as kinks. These kinks appear and propagate at an extent and on a timescale that depend on the monomer structure.

Altogether, our results show that the degree of order along the fiber is a result of the competition between hydrogen bonding along the backbone of the supramolecular polymer with groups at the monomer periphery. The competition between these two hydrogen bonding patterns appears to be modulated by the steric demands of the peripheral alkyl substituents. The disordering effect due to amide-ether hydrogen bonds shown by the MD simulations was experimentally observed through differences of supramolecular polymerizations for the various compounds, both in the bulk and methylcyclohexane solutions. This combined approach is key to arrive at design principles and a complete understanding of supramolecular polymerizations. We hope our results will pave the way for such systematic studies of supramolecular polymers and other non-covalent systems both in water and organic media.

Supporting Information

Supporting Information is available below.

Conflicts of interest

There are no conflicts to declare.

Acknowledgements

MFJM and ARAP thank E.W. (Bert) Meijer for stimulating discussions, Elisabeth Weyandt for providing several aldehyde starting materials, and acknowledge financial support from NWO (TOP-PUNT Grant 10018944) and the Dutch Ministry of Education, Culture and Science (Gravitation program 024.001.035). RMR, HSC, JB and JMF acknowledge the

Ministerio de Ciencia Innovación y Universidades (Spain) for funding through the Ramón y Cajal Program (RYC-2013-12570) and Proyectos I+D+i (CTQ2015-66869-P). HSC is grateful for a FPU fellowship from Ministerio de Educación Cultura y Deporte (Spain). The collaboration between Eindhoven and Mons is supported by the Fonds de la Recherche Scientifique - FNRS and the Fonds Wetenschappelijk Onderzoek under EOS Project No.30650939. Computational resources have been provided by the Consortium des Équipements de Calcul Intensif (CÉCI), funded by the Fonds de la Recherche Scientifique de Belgique (F.R.S.-FNRS) under Grant No. 2.5020.11 and by the Wallonia Region. S.K., M.F. and M.S. thank Dr. Patrick Brocorens for helpful comments on the manuscript.

References

1 T. Aida, E. W. Meijer and S. I. Stupp, *Science*, 2012, **335**, 813–817.

2 L. Zang, Y. Che and J. S. Moore, *Acc. Chem. Res.*, 2008, **41**, 1596–1608.

3 S. S. Babu, V. K. Praveen and A. Ajayaghosh, *Chem. Rev.*, 2014, **114**, 1973–2129.

4 P. A. Korevaar, S. J. George, A. J. Markvoort, M. M. J. Smulders, P. A. J. Hilbers, A. P. H. J. Schenning, T. F. A. De Greef and E. W. Meijer, *Nature*, 2012, **481**, 492–496.

5 F. Fennel, S. Wolter, Z. Xie, P. A. Plötz, O. Kühn, F. Würthner and S. Lochbrunner, *J. Am. Chem. Soc.*, 2013, **135**, 18722–18725.

6 S. Ogi, C. Grzeszkiewicz and F. Würthner, *Chem. Sci.*, 2018, **9**, 2768–2773.

7 K. Cai, J. Xie, D. Zhang, W. Shi, Q. Yan and D. Zhao, *J. Am. Chem. Soc.*, 2018, **140**, 5764–5773.

8 A. Sorrenti, J. Leira-Iglesias, A. J. Markvoort, T. F. A. De Greef and T. M. Hermans, *Chem. Soc. Rev.*, 2017, **46**, 5476–5490.

9 S. Ogi, K. Sugiyasu, S. Manna, S. Samitsu and M. Takeuchi, *Nat. Chem.*, 2014, **6**, 188–195.

10 S. Ogi, T. Fukui, M. L. Jue, M. Takeuchi and K. Sugiyasu, *Angew. Chemie - Int. Ed.*, 2014, **53**,

14363–14367.

11 J. Kang, D. Miyajima, T. Mori, Y. Inoue, Y. Itoh and T. Aida, *Science*, 2015, **347**, 646–651.

12 K. V. Rao, D. Miyajima, A. Nihonyanagi and T. Aida, *Nat. Chem.*, 2017, **9**, 1133–1139.

13 K. V. Rao, M. F. J. Mabesoone, D. Miyajima, A. Nihonyanagi, E. W. Meijer and T. Aida, *J. Am. Chem. Soc.*, 2020, **142**, 598–605.

14 M. Wehner, M. I. S. Röhr, M. Bühler, V. Stepanenko, W. Wagner and F. Würthner, *J. Am. Chem. Soc.*, 2019, **141**, 6092–6107.

15 J. S. Valera, R. Gómez and L. Sánchez, *Angew. Chemie - Int. Ed.*, 2019, **58**, 510–514.

16 P. van der Schoot, in *Supramolecular Polymers, Second Edition*, CRC Press, 2005.

17 R. Van Buel, D. Spitzer, C. M. Berac, P. Van Der Schoot, P. Besenius and S. Jabbari-Farouji, *J. Chem. Phys.*, 2019, **151**, 014902.

18 A. J. Markvoort, H. M. M. Ten Eikelder, P. A. J. Hilbers, T. F. A. De Greef and E. W. Meijer, *Nat. Commun.*, 2011, **2**, 509.

19 H. M. M. ten Eikelder, A. J. Markvoort, T. F. A. de Greef and P. A. J. Hilbers, *J. Phys. Chem. B*, 2012, **116**, 5291–5301.

20 H. M. M. ten Eikelder, B. Adelizzi, A. R. A. Palmans and A. J. Markvoort, *J. Phys. Chem. B*, 2019, **123**, 6627–6642.

21 J. Gershberg, F. Fennel, T. H. Rehm, S. Lochbrunner and F. Würthner, *Chem. Sci.*, 2016, **7**, 1729–1737.

22 Y. Liu, Y. Zhang, F. Fennel, W. Wagner, F. Würthner, Y. Chen and Z. Chen, *Chem. - A Eur. J.*, 2018, **24**, 16388–16394.

23 M. Roman, C. Cannizzo, T. Pinault, B. Isare, B. Andrioletti, P. Van Der Schoot and L. Bouteiller, *J. Am. Chem. Soc.*, 2010, **132**, 16818–16824.

24 M. F. J. Mabesoone, A. J. Markvoort, M. Banno, T. Yamaguchi, F. Helmich, Y. Naito, E. Yashima, A. R. A. Palmans and E. W. Meijer, *J. Am. Chem. Soc.*, 2018, **140**, 7810–7819.

25 K. K. Bejagam, G. Fiorin, M. L. Klein and S. Balasubramanian, *J. Phys. Chem. B*, 2014, **118**, 5218–5228.

26 K. K. Bejagam and S. Balasubramanian, *J. Phys. Chem. B*, 2015, **119**, 5738–5746.

27 A. Desmarchelier, M. Raynal, P. Brocorens, N. Vanthuyne and L. Bouteiller, *Chem. Commun.*, 2015, **51**, 7397–7400.

28 J. A. Berrocal, F. Di Meo, M. García-Iglesias, R. P. J. Gosens, E. W. Meijer, M. Linares and A. R. A. Palmans, *Chem. Commun.*, 2016, **52**, 10870–10873.

29 A. Desmarchelier, B. G. Alvarenga, X. Caumes, L. Dubreucq, C. Troufflard, M. Tessier, N. Vanthuyne, J. Idé, T. Maistriaux, D. Beljonne, P. Brocorens, R. Lazzaroni, M. Raynal and L. Bouteiller, *Soft Matter*, 2016, **12**, 7824–7838.

30 M. Garzoni, M. B. Baker, C. M. A. Leenders, I. K. Voets, L. Albertazzi, A. R. A. Palmans, E. W. Meijer and G. M. Pavan, *J. Am. Chem. Soc.*, 2016, **138**, 13985–13995.

31 P. W. J. M. Frederix, J. Idé, Y. Altay, G. Schaeffer, M. Surin, D. Beljonne, A. S. Bondarenko, T. L. C. Jansen, S. Otto and S. J. Marrink, *ACS Nano*, 2017, **11**, 7858–7868.

32 D. Bochicchio and G. M. Pavan, *ACS Nano*, 2017, **11**, 1000–1011.

33 P. Gasparotto, D. Bochicchio, M. Ceriotti and G. M. Pavan, *J. Phys. Chem. B*, 2020, **124**, 589–599.

34 C. Kulkarni, S. K. Reddy, S. J. George and S. Balasubramanian, *Chem. Phys. Lett.*, 2011, **515**, 226–230.

35 D. B. Korlepara, W. R. Henderson, R. K. Castellano and S. Balasubramanian, *Chem. Commun.*, 2019, **55**, 3773–3776.

36 Y. Nakano, T. Hirose, P. J. M. Stals, E. W. Meijer and A. R. A. Palmans, *Chem. Sci.*, 2012, **3**, 148–155.

37 J. J. Van Gorp, J. A. J. M. Vekemans and E. W. Meijer, *Mol. Cryst. Liq. Cryst.*, 2003, **397**, 191–205.

38 S. Ghosh, X.-Q. Li, V. Stepanenko and F. Würthner, *Chem. - A Eur. J.*, 2008, **14**, 11343–11357.

39 R. van der Weegen, A. J. P. Teunissen, E. W. W. Meijer, R. Weegen and A. J. P. Teunissen, *Chem. - A Eur. J.*, 2017, **23**, 1–12.

40 T. E. Kaiser, V. Stepanenko and F. Würthner, *J. Am. Chem. Soc.*, 2009, **131**, 6719–6732.

41 A. Sandeep, V. K. Praveen, D. S. Shankar Rao, S. Krishna Prasad and A. Ajayaghosh, *ACS Omega*, 2018, **3**, 4392–4399.

42 P. Kumar and M. Bansal, *J. Biomol. Struct. Dyn.*, 2012, **30**, 773–783.

43 Y. Matsunaga, N. Miyajima, Y. Nakayasu, S. Sakai and M. Yonenaga, *Bull. Chem. Soc. Jpn.*, 1988, **61**, 207–210.

44 P. J. M. Stals, M. M. J. Smulders, R. Martín-Rapún, A. R. A. Palmans and E. W. Meijer, *Chem. - A Eur. J.*, 2009, **15**, 2071–2080.

45 C. Kulkarni, S. Balasubramanian and S. J. George, *ChemPhysChem*, 2013, **14**, 661–673.

46 C. Kulkarni, E. W. Meijer and A. R. A. Palmans, *Acc. Chem. Res.*, 2017, **50**, 1928–1936.

47 D. Zhao and J. S. Moore, *Org. Biomol. Chem.*, 2003, **1**, 3471–3491.

48 S. Kumar, *Handbook of liquid crystals*, Wiley-VCH Verlag, Weinheim, 2014.

Entry for the Table of Contents

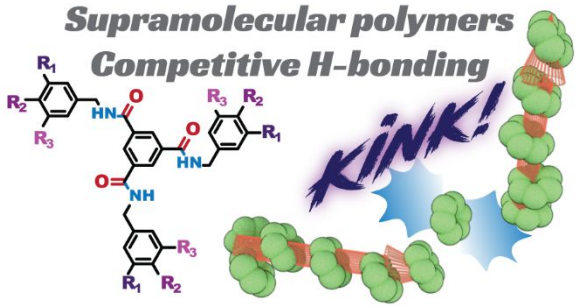

By combining experiments and modelization we elucidate the role of competitive hydrogen bonding on the supramolecular behavior of tris(alkoxybenzyl)benzene-1,3,5-tricarboxamides

Design, System, Application

Despite the numerous reports on supramolecular polymers, structure-property relationships are still lacking. Here, we designed several new types of substituted tribenzylbenzene-1,3,5-tricarboxamides, as monomers for supramolecular polymerization. To arrive at a rational translation of molecular properties to material properties, we first study the supramolecular polymers with molecular dynamics (MD) simulations. These simulations show that introduction of ether moieties at the monomer periphery induces defects in the polymers, as a result of hydrogen bonding between these ethers and the central amides. The structural defects of the polymers are experimentally confirmed both in bulk and in solution. We anticipate that the rational design rules obtained through our combined computational and experimental insights may facilitate the design of complex and adaptive supramolecular polymers.

On the molecular origins of cooperativity in supramolecular polymerization of 1,3,5-benzene tricarboxamides

Mathijs F.J. Mabesoone,[a]† Sinan Kardas,[a,b]† Héctor Soria-Carrera,[c] Joaquín Barberá,[c] Jesús M. de la Fuente,[c] Anja R.A. Palmans,*[a] Mathieu Fosséprè,[b] Mathieu Surin*[b] and Rafael Martín-Rapún*[c,d]

Supporting Information

Table of Contents

Molecular Dynamics (MD) simulations 2
Full POM and solid state IR results 8
Instruments and measurements 10
Synthesis details 11
IR spectra of BTA derivatives 37
VT-UV and VT-CD spectra of BTA derivatives 39
Additional VT-UV and VT-CD cooling curves 41
Fits of cooling curves Cit-3, Cit-9 and C8-9 42
MALDI-TOF mass spectra of the BTA derivatives 43
NMR spectra of the BTA derivatives 46
DSC thermograms of the BTA derivatives 62

[a] *M.F.J. Mabesoone, S. Kardas, Prof. Dr. A.R.A. Palmans*
Laboratory of Macromolecular and Organic Chemistry and Institute for Complex Molecular Systems
Eindhoven University of Technology
Eindhoven (The Netherlands)
E-mail: A.R.A.Palmans@tue.nl

[b] *S. Kardas, Dr. M. Fosséprè, Dr. M. Surin*
Laboratory for Chemistry of Novel Materials
Center of Innovation and Research in Materials and Polymers
University of Mons–UMONS
Mons (Belgium)
E-mail: Mathieu.Surin@umons.ac.be

[c] *H. Soria-Carrera, Prof. Dr. J. Barberá, Prof. Dr. J. M. de la Fuente, Dr. R. Martín-Rapún*
Department of Organic Chemistry - Instituto de Ciencia de Materiales de Aragón
University of Zaragoza-CSIC
Zaragoza (Spain)

[d] *Dr. R. Martín-Rapún*
Instituto de Nanociencia de Aragón
University of Zaragoza,
Zaragoza (Spain)
E-mail: rmartin@unizar.es

† These authors contributed equally

Molecular Dynamics (MD) simulations

Computational details

All-atom molecular dynamics (MD) simulations, an effective technique to get more insight into molecular order and dynamics of supramolecular systems,[1,2] were performed using AMBER 16 software.[3] We started from prearranged BTA fibers. For this, BTA monomers were built within Discovery Studio 4.0[4] and parametrized with the '*general AMBER force field (GAFF)*'[5]. The partial atomic charges of monomers were calculated using the semiempirical AM1-BCC model[6,7] with the *antechamber* module.[8] Then, these monomers were replicated along the z-axis to build fibers of 12 and 24 BTA units, characterized by a stacking distance (between adjacent BTAs) of 5 *Å*, chosen higher than the characteristic BTA stacking distance of ~3.4 *Å*[9] to avoid biasing the system. Once BTA fibers were built, we performed a 10,000 steps energy minimization consisting in 1,000 steps of steepest descent algorithm, followed by 9,000 cycles of conjugate gradient. After initial energy minimization, BTA fibers underwent 500 ns of MD simulations. Particle velocities in each direction were randomly assigned according to the Maxwell-Boltzmann velocity distribution function at the specified temperature. MD simulations were performed at a temperature of 300 K using a Langevin thermostat with a coupling constant of 1 ps. Non-bonded interactions were calculated with a virtual infinite cutoff. All MD simulations used a time step of 1 fs and were performed in the gas phase (*i.e.* no solvent) to reproduce the low dielectric constant of MCH in which BTAs self-assemble and to reduce the computational cost. The resulting trajectories were visualized using the *VMD* software package[10] and snapshots of the MD trajectories were captured using *PyMOL.*[11]

Position of defects in the fibers. The distance/angle between center-of-mass of BTA cores were calculated using *cpptraj* module[12] of AMBER 16. Each distance/angle was averaged over the entire simulations and plotted for each pair/triad of BTA units sliding in steps of one BTA unit along the fiber (starting from the first BTA unit).

Hydrogen bonds. Intermolecular H-bonds (amide-amide or amide-ether H-bonds) between BTA units were identified using *cpptraj* module of AMBER 16. A donor (D)-acceptor (A) distance cut-off of 3.5 Å and no A-H-D angle cutoff were used to prevent missing any possible hydrogen bonds. Only persistent H-bonds (*i.e.* those present more than 90% of simulation time) were considered.

Helical kink identification. The bending and the kinking of helices were computed using the HELANAL-Plus[13] software which follows the method of Sugeta and Miyazawa.[14] It calculates the local axis of the helix by fitting least square 3D line and sphere to local helix origin points. A local helix axis is defined for a window of four consecutive BTA centers-of-mass. This window then slides along the length of the helix one BTA unit at a time. Local bending angles (one for each window of four consecutive BTA centers-of-mass, except at the ends of the helix) are calculated from the angle between local helix axis and the helix axis (Fig. S4). The region of kink is characterized by large

values of local bending angles at several consecutive window and is identified from 2D-plots of the local bending angle at the position *i* (position of the sliding window of four consecutive BTA units) versus the simulation time. To quantify the number of kinks for each helix, we applied an angle cutoff of 90° above which a kink is considered as an authentic kink, while regions of lower bending angles are considered as straight. This value was chosen for consistency with the fact that BTA cores are not uniaxially stacked on top each other.

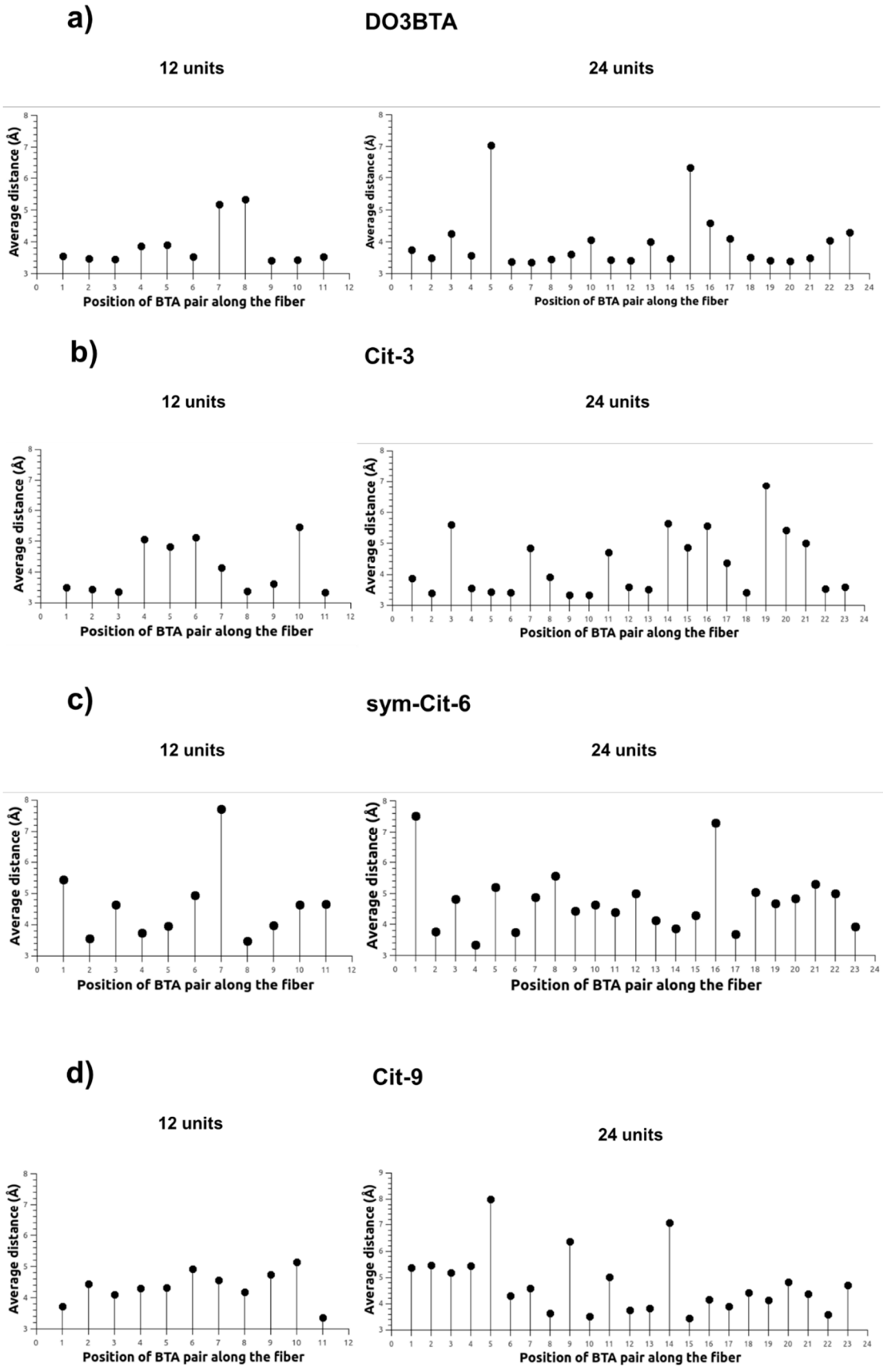

Figure S1. Plots of average distances between pairs of BTA cores for a) **DO3BTA** (reference BTA), b) **Cit-3**, c) **Sym-Cit-6**, d) **Cit-9** fibers of 12 units (left) and 24 units (right).

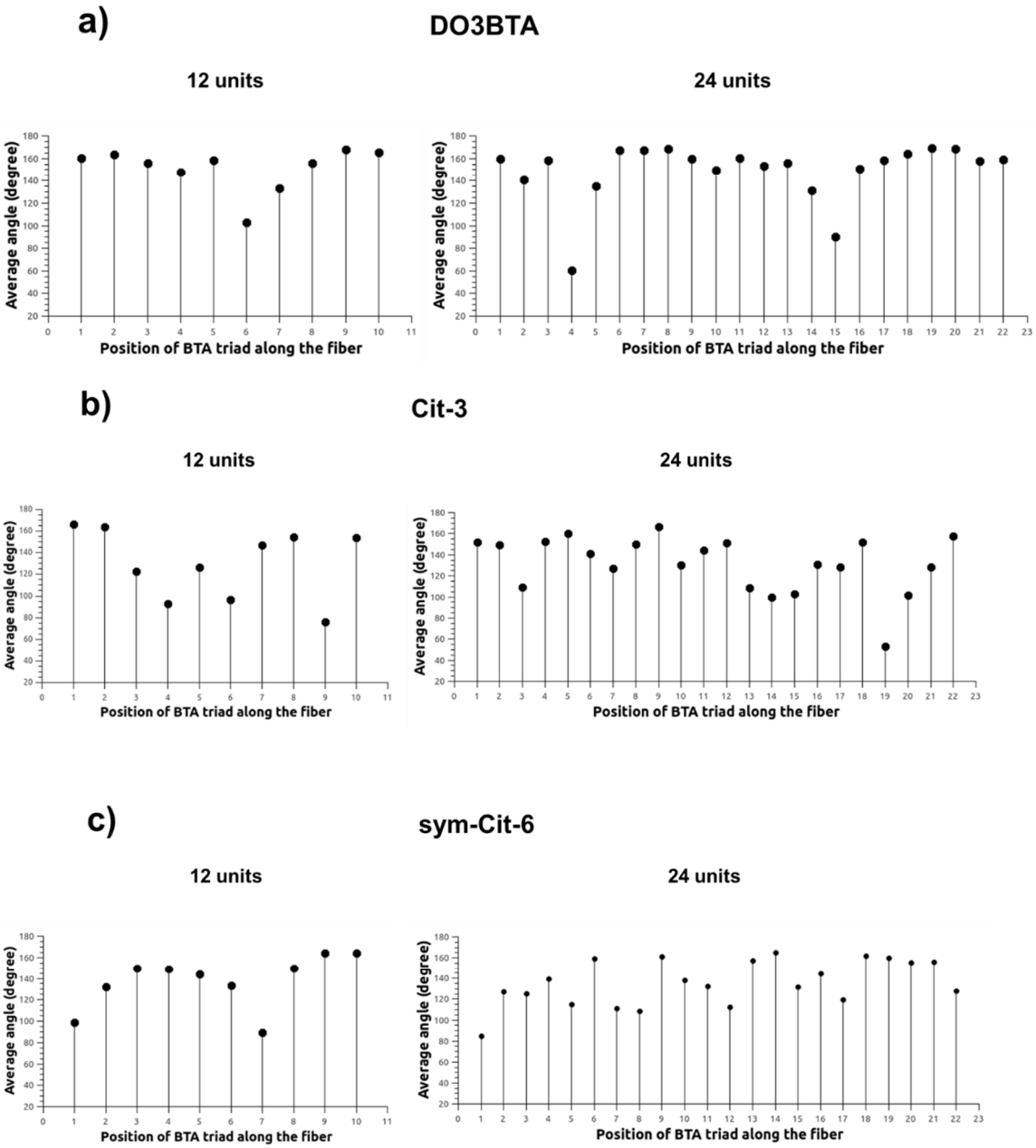

Figure S2. Plots of average angles between triads of BTA cores for a) **DO3BTA** (reference BTA), b) **Cit-3**, c) **Sym-Cit-6**, d) **Cit-9** fibers of 12 units (left) and 24 units (right).

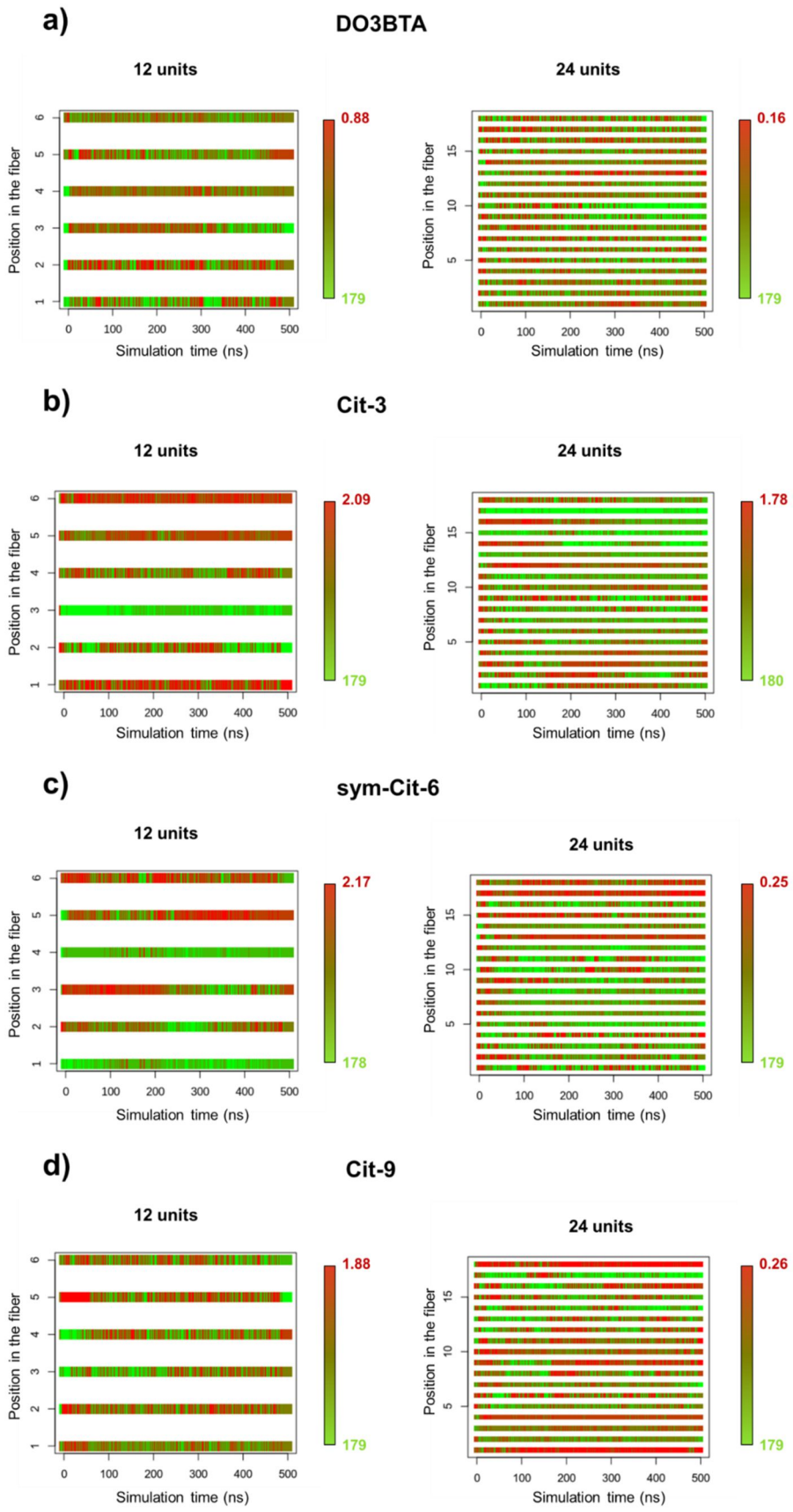

Figure S3. Evolution of the local bending angles at the position *i* (position of the sliding window of four consecutive BTA units) versus the simulation time for a) **DO3BTA** (reference BTA), b) **Cit-3**, c) **Sym-Cit-6**, d) **Cit-9** fibers of 12 units (left) and 24 units (right). Red regions indicate low bending angles values; green regions indicate high bending angles values.

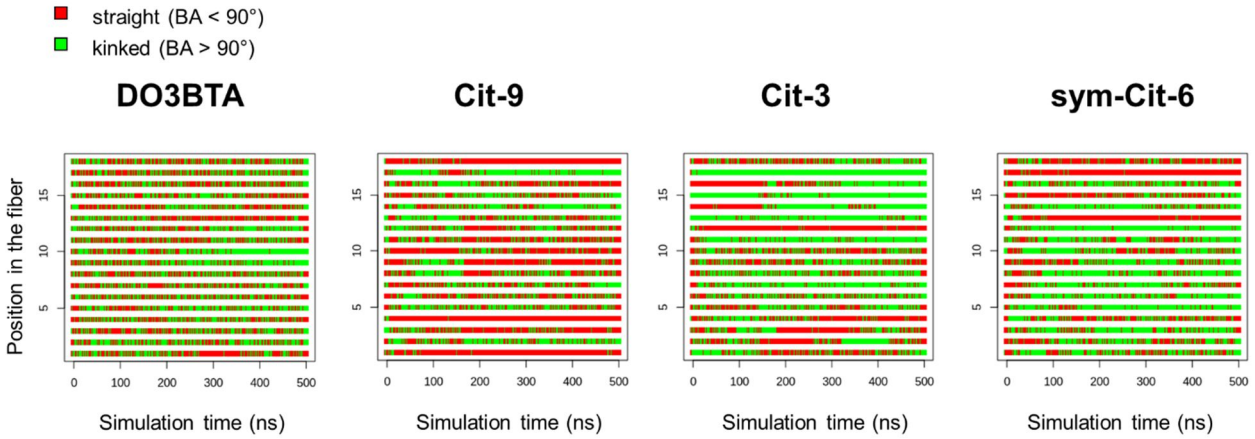

Figure S4. For fibers of 24 BTA units, evolution of the local bending angles at the position along the fiber (position of the sliding window of four consecutive BTA units, see computational details and Fig. S4 for the definition) versus the MD simulation time. Kinked regions appear through a binary color code of bending angles (BA): red regions indicate a straight portion of the fiber (BA < 90°), while green regions indicate kinked portions (BA > 90°). From left to right: **DO3BTA** (reference BTA), **Cit-9**, **Cit-3**, **Sym-Cit-6**.

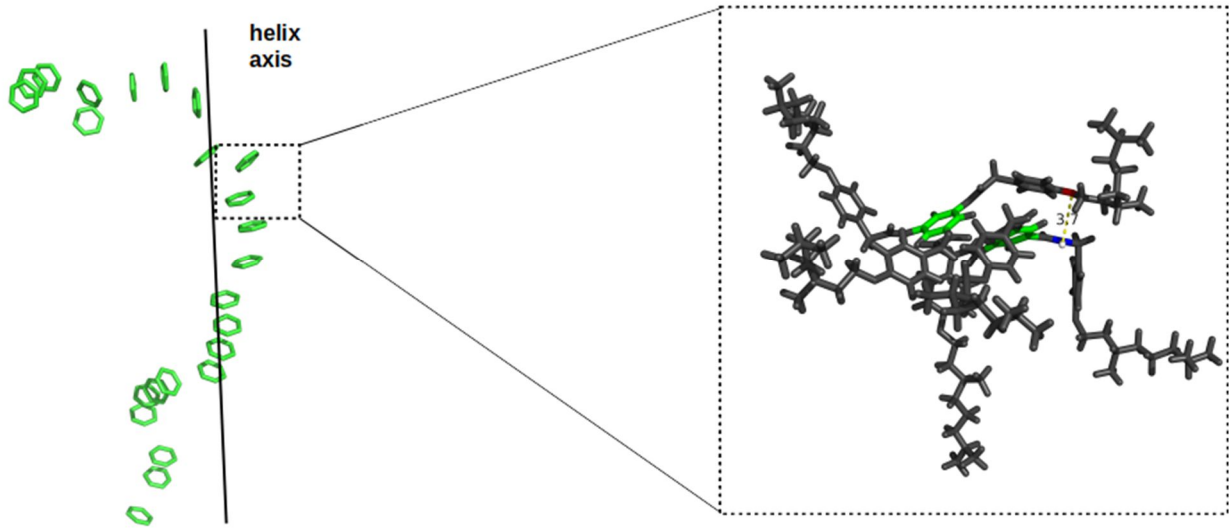

Figure S5. Snapshot of 24 **Cit-3** BTA cores conformation at 40 ns and zoom showing disordering amide-ether hydrogen-bond between the two BTA units where a structural defect is localized.

Full POM and solid state IR results

Table S1. Diffraction spacings in Å for BTA's.

hkl	**DO3BTA**[a]	**C8-3**[b]	**Cit-3**	**Cit-6**	**C8-6**	**C8-9**
T (°C)	140	159	120	124	85	73
1 0 0	17.2	16.0	20.6	24.9	23.0	26.7
1 1 0	9.9	9.1	11.8	–	–	15.5
2 0 0	8.6	8.1	10.3	–	–	13.4
2 1 0	–	–	–	9.4	8.7	–
3 0 0	–	–	–	8.3	7.7	–
3 1 0	–	–	–	6.9	6.5	7.2
halo	5.0	4.8	4.7	4.6	4.6	4.6
interdisc	3.5	3.5	3.5	3.5	3.5	3.5
intercolumn	19.9	18.5	23.8	28.8	26.6	30.8
Density (Z = 1)[c]	0.87	0.89	0.88	0.94	0.97	0.94

[a] P. J. M. Stals, J. F. Haveman, R. Martín-Rapún, C. F. C. Fitié, A. R. A. Palmans, E. W. Meijer, J. Mater. Chem. 2009, 19, 124 – 130.[15] [b] P. J. M. Stals, M. M. J. Smulders, R. Martín-Rapún, A. R. A. Palmans, E.W. Meijer, Chem. Eur. J. 2009, 15, 2071 – 2080.[16] [c] g cm^{-3}

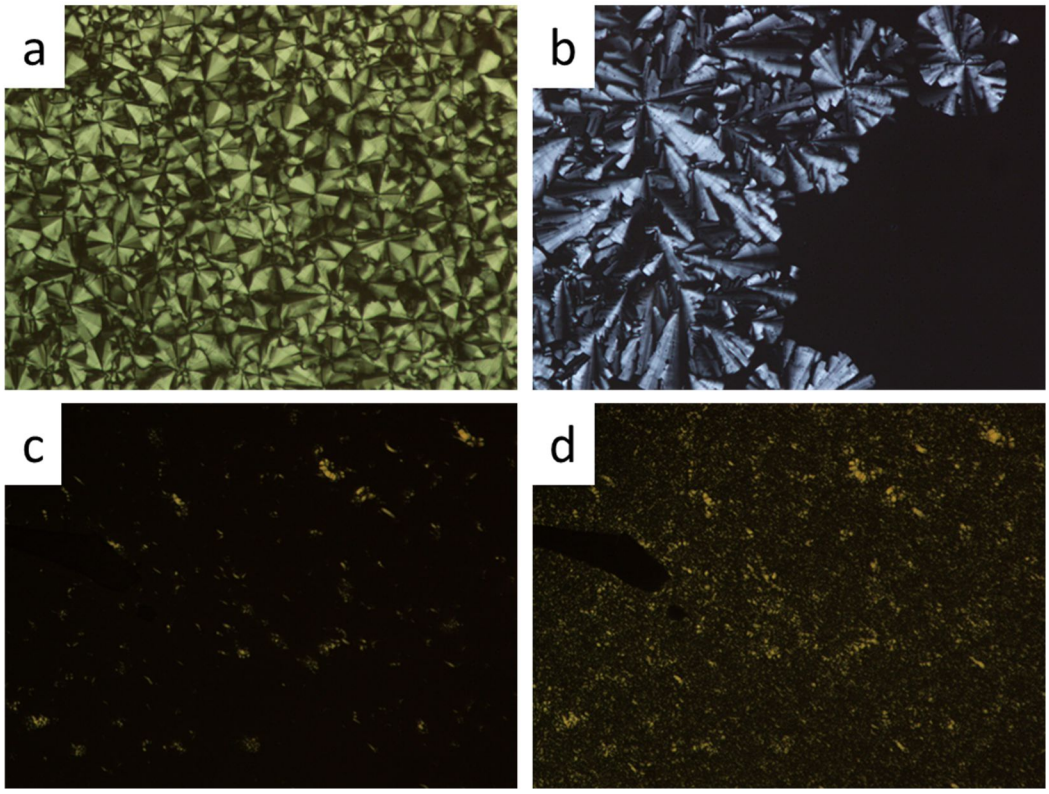

Figure S6. Optical textures (crossed polarizers) obtained after slow cooling from the isotropic state for (a) **C8-3** at 119 °C, (b) **C8-6** at 151 °C, (c) **C8-9** at 66 °C, and (d) **C8-9** at 57 °C.

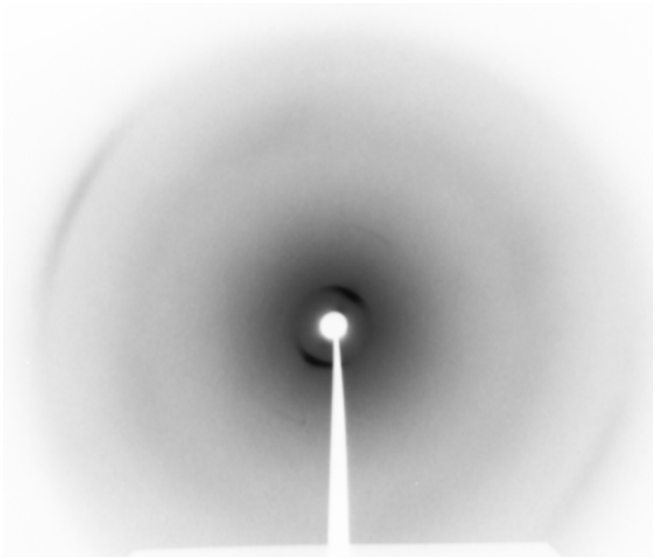

Figure S7. Diffraction pattern observed for aligned **Cit-6** measured at 124 °C./

Instruments and measurements

^{1}H and ^{13}C NMR (400 and 101 MHz respectively) spectra were recorded on a Bruker AV-400 spectrometer and a Bruker Avance 3 HD NanoBay spectrometer. Chemical shifts are given in ppm relative to the solvent residual peak, which was used as internal reference. Coupling constants are given in Hertz. Spectra were processed with *MestReNova 10.0.2* from Mestrelab Research.

MALDI-ToF mass spectrometry was performed on a Bruker Autoflex Speed spectrometer. ESI-MS was performed on a Thermo Finnigan LCQ Fleet ion trap mass spectrometer. FTIR spectroscopy was performed in a *Jasco* FT-IR 4100 instrument with an ATR accessory, in which samples were measured without any preparation, or a PerkinElmer Spectrum Two spectrometer. Solution state IR measurements were performed using NaCl cells. All frequencies of characteristic bands are reported in cm^{-1}.

Mesogenic behavior was investigated by polarized light optical microscopy (POM) using an Olympus BS51 Polarizing Optical Microscope fitted with a Linkam THMS600 hot stage.

Differential scanning calorimetry (DSC) experiments were performed on a TA DSC Q-20 and Q-2000 instrument under nitrogen atmosphere in aluminum pans and a scanning rates of 10 °C·min^{-1}. Three consecutive thermal cycles were carried out. The transition temperatures were read at the maximum or the onset of the corresponding peaks in the second or third cycle.

X-Ray diffraction measurements (XRD) were carried out with a Pinhole camera (Anton Paar) operating with a point-focused Ni-filtered Cu-Kα beam. Samples were contained in Lindemann glass capillaries (0.9 or 0.7 mm diameter) and, when necessary, a variable temperature attachment was used to heat the sample. The patterns were collected on flat photographic film perpendicular to the X-ray beam. Bragg's law was used to obtain the spacing ($n \times \lambda = 2 \times d \times \sin\theta$).

CD spectroscopy was measured on a Jasco J-815 spectrometer with a thermostatted PCT-742 or MPTC-490 sample holder. Samples were prepared by dissolving the solid material in MCH in an air-tight vial and heating and sonicating the mixture until no solid material could be observed anymore. Samples were measured in screw-capped cuvettes and cooled at a rate of 1 °C·min^{-1}.

Synthesis details

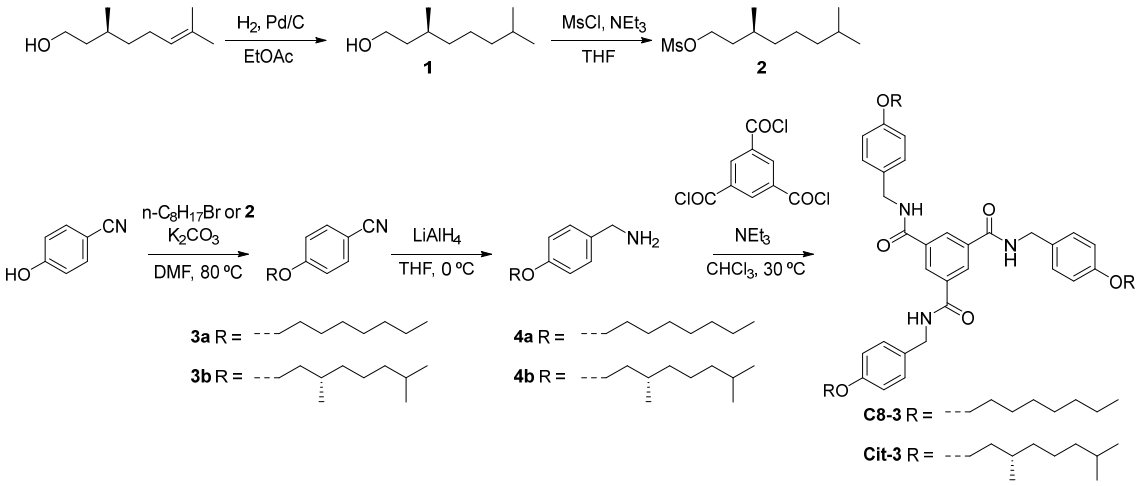

Scheme S1. Synthetic route to **C8-3** and **Cit-3**.

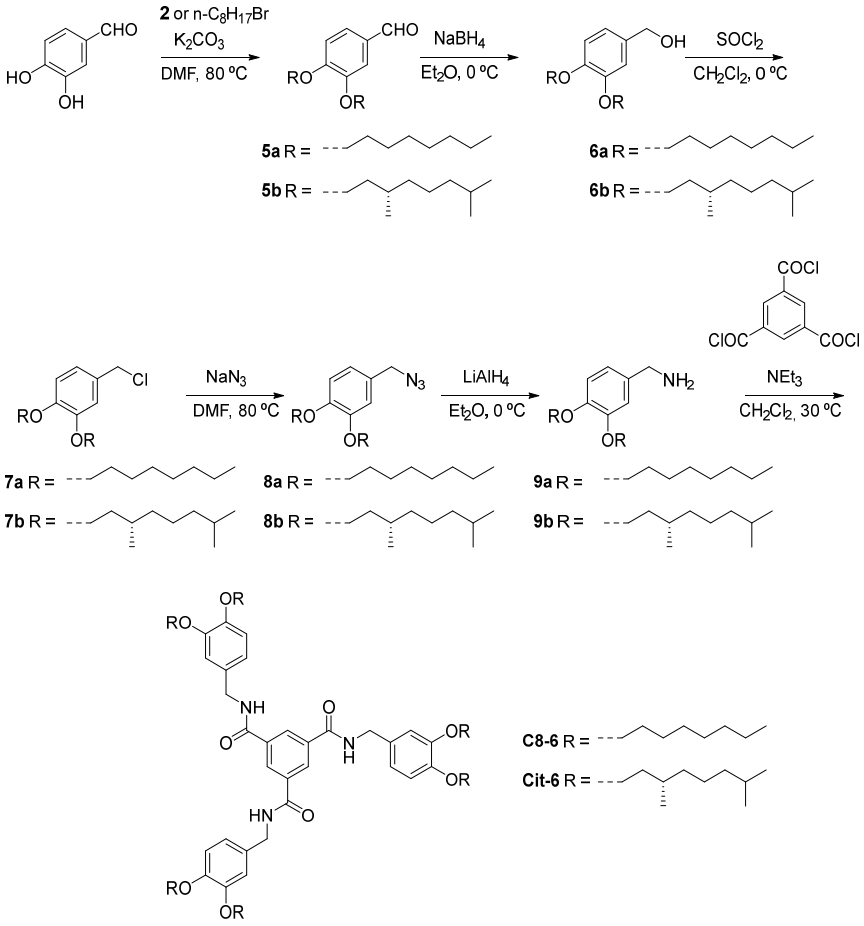

Scheme S2. Synthetic route to **C8-6** and **Cit-6**.

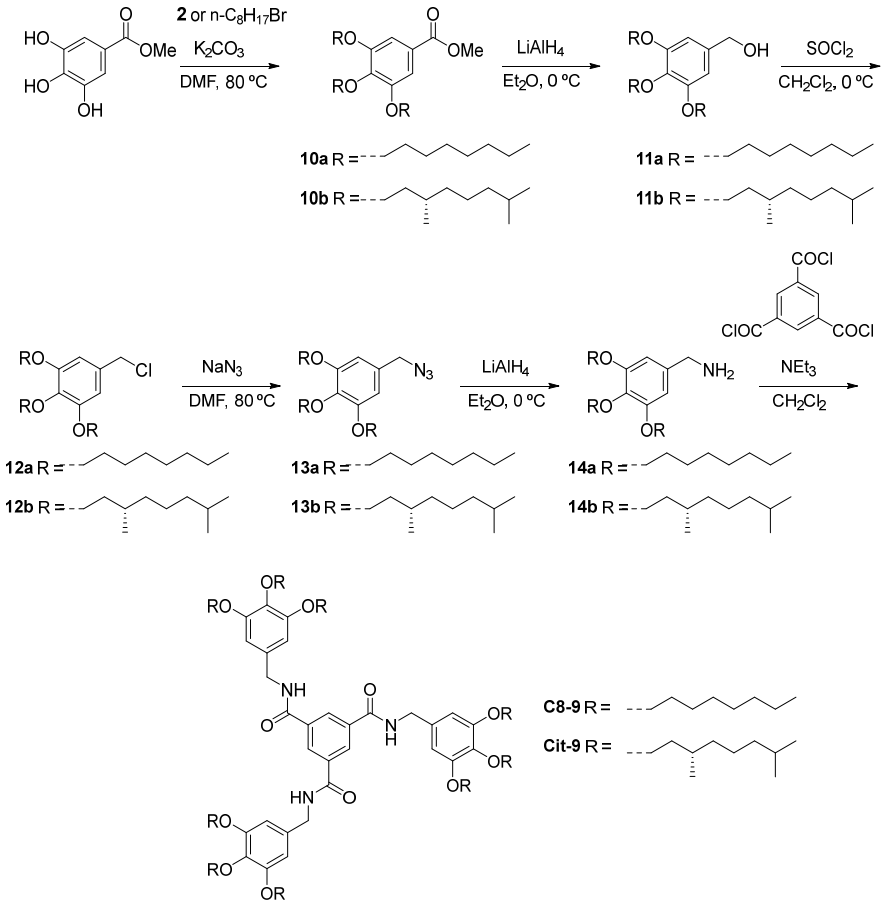

Scheme S3. Synthetic route to **C8-9** and **Cit-9**.

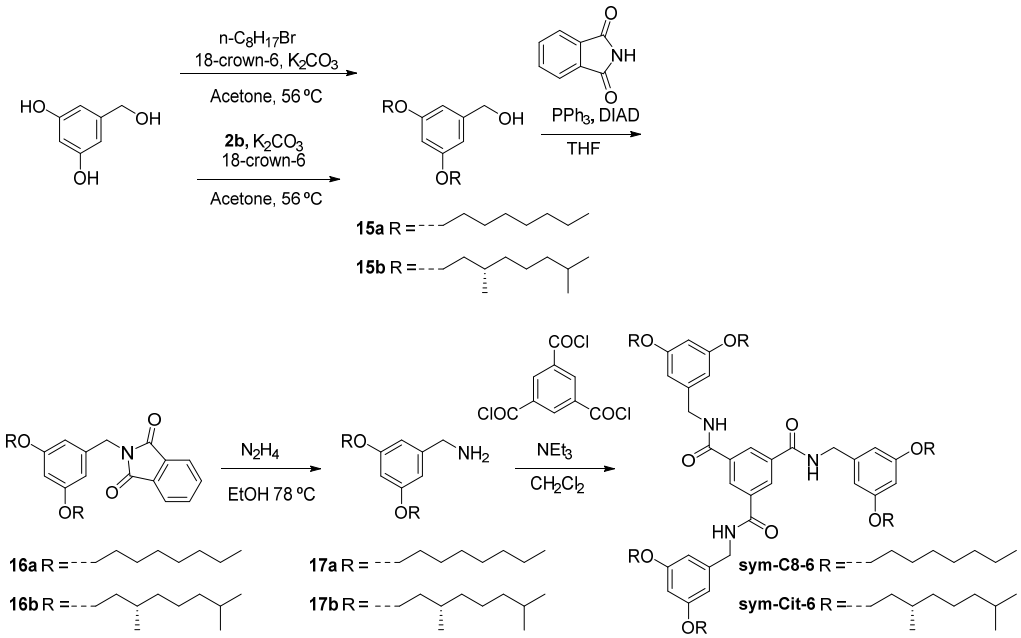

Scheme S4. Synthetic route to **sym-C8-6** and **Sym-Cit-6**.

General procedure for the synthesis of the C3-symmetrical compounds

To a solution of the appropriate benzylamine derivative (0.39 mmol) and trimethylamine (0.42 mmol) in anhydrous dichloromethane or chloroform (10 mL) at 0 °C, 1,3,5-benzenetricarbonyl chloride (0.12 mmol) was added and the reaction mixture was then allowed to reach room temperature (or heated to reflux temperature if the solution was not homogeneous). After 14-18 h the mixture was diluted with dichloromethane (10 mL) and washed with aqueous HCl (1 M, 2 x 10 mL). The organic layer was then dried over anhydrous Na2SO4, filtered and the solvents were removed under reduced pressure. The crude product was purified by column chromatography.

Synthesis of C8-3

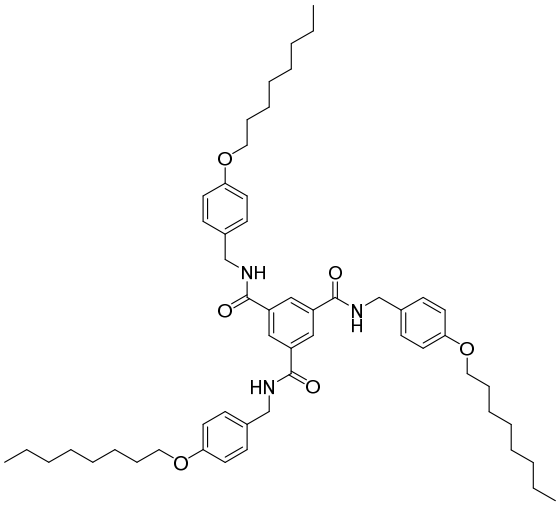

FTIR-ATR (neat): 3244, 3069, 2925, 2854, 1638, 1553, 1511, 1299, 1246, 1232, 1177 cm^{-1}

^{1}H NMR (399 MHz, $CDCl_3$) δ 8.33 (s, 3H), 7.23 (d, *J* = 8.6 Hz, 5H), 6.92 – 6.78 (m, 6H), 6.64 (t, *J* = 5.5 Hz, 3H), 4.54 (d, *J* = 5.5 Hz, 6H), 3.93 (t, *J* = 6.6 Hz, 6H), 1.84 – 1.69 (m, 6H), 1.52 – 1.39 (m, 6H), 1.39 – 1.17 (m, 24H), 1.00 – 0.77 (m, 9H).

^{13}C NMR (101 MHz, $CDCl_3$) δ 165.34, 158.79, 135.05, 129.34, 129.28, 128.22, 114.80, 77.00, 68.09, 43.91, 31.81, 30.92, 29.35, 29.23, 26.03, 22.65, 14.09.

HRMS (ESI): $C_{54}H_{75}N_3O_6$ $[M+Na]^+$, mass calculated: 884.55, mass found: 884.57; $[M+K]^+$, calculated: 900.53, found: 900.54.

Synthesis of Cit-3

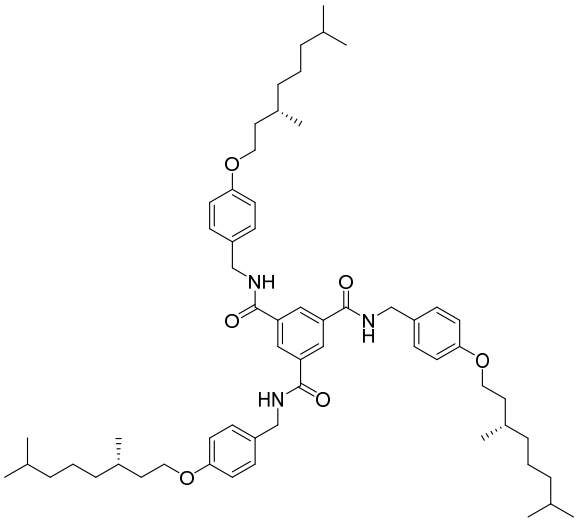

FTIR-ATR (neat): 3231, 3065, 2954, 2925, 2869, 1637, 1556, 1511, 1298, 1246, 1233, 1175 cm^{-1}

^{1}H NMR (400 MHz, $CDCl_3$) δ 8.34 (s, 3H), 7.26 (s, 6H), 6.87 (d, *J* = 8.6 Hz, 6H), 6.57 (t, *J* = 5.6 Hz, 3H), 4.56 (d, *J* = 5.4 Hz, 6H), 3.99 (d, *J* = 7.0 Hz, 6H), 1.90 – 1.75 (m, 3H), 1.75 – 1.43 (m, 15H), 1.42 – 1.21 (m, 14H), 1.21 – 1.06 (m, 6H), 0.94 (d, *J* = 6.5 Hz, 9H), 0.87 (d, *J* = 6.6 Hz, 18H).

^{13}C NMR (101 MHz, $CDCl_3$) δ 165.33, 158.79, 135.05, 129.35, 129.28, 128.23, 114.81, 66.41, 43.92, 39.23, 37.29, 36.16, 29.84, 27.96, 24.64, 22.70, 22.60, 19.62.

HRMS (ESI): $C_{60}H_{87}N_3O_6Na$ $[M+Na]^+$, mass calculated: 968.65, mass found: 968.65.

Synthesis of C8-6

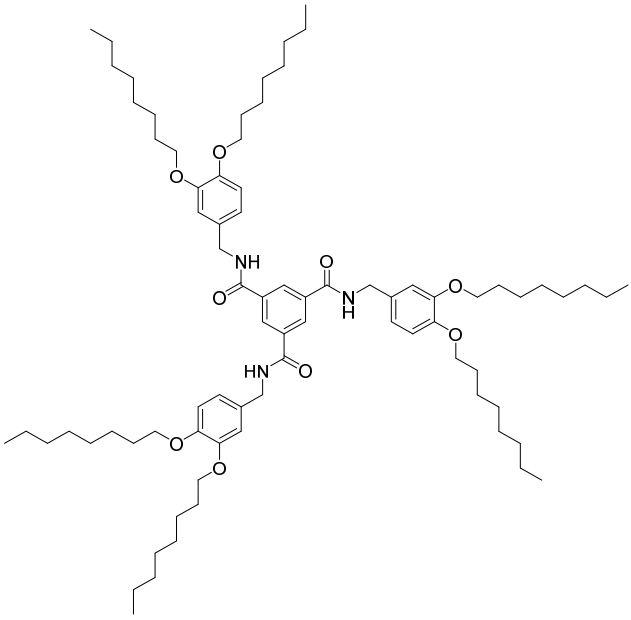

FTIR-ATR (neat): 3237, 3069, 2924, 2855, 1644, 1515, 1264, 1137 cm^{-1}.

^{1}H NMR (400 MHz, $CDCl_3$) δ 8.40 (d, *J* = 2.6 Hz, 3H), 6.87 – 6.64 (m, 11H), 4.50 (d, *J* = 3.2 Hz, 3H), 4.00 – 3.86 (m, 12H), 1.95 – 1.70 (m, 14H), 1.70 – 1.54 (m, 3H), 1.54 – 1.37 (m, 15H), 1.37 – 1.01 (m, 51H), 0.97 – 0.73 (m, 18H).

^{13}C NMR (101 MHz, $CDCl_3$) δ 165.18, 149.34, 148.74, 134.97, 129.99, 128.34, 120.65, 114.04, 113.98, 69.42, 69.34, 44.36, 31.81, 29.37, 29.37, 29.30, 29.26, 26.02, 26.00, 22.65, 14.08.
HRMS (ESI): $C_{78}H_{123}N_3O_9$ $[M+Na]^+$, mass calculated: 1268.92, mass found: 1268.93. $C_{78}H_{123}N_3O_9K$ $[M+K]^+$, calculated: 1284.89, found: 1284.90.

Synthesis of Cit-6

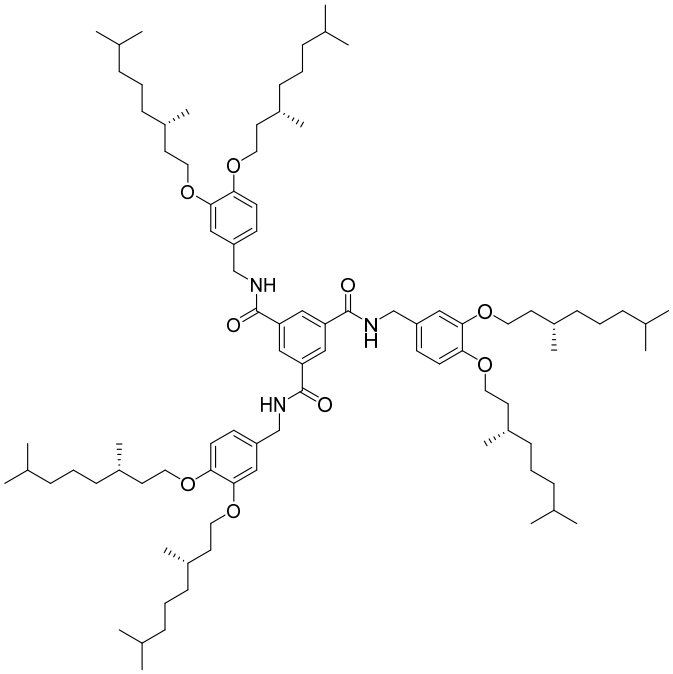

FTIR-ATR (neat): 3237, 3066, 2954, 2926, 2869, 1636, 1514, 1558, 1512, 1468, 1427, 1295, 1263, 1232, 1137 cm^{-1}.
^{1}H NMR (400 MHz, $CDCl_3$) δ 8.37 (s, 3H), 6.83 (s, 9H), 6.65 (t, *J* = 5.4 Hz, 3H), 4.53 (d, *J* = 5.4 Hz, 6H), 4.17 – 3.80 (m, 12H), 1.92 – 1.75 (m, 6H), 1.74 – 1.42 (m, 13H), 1.42 – 1.01 (m, 40H), 0.93 (dd, *J* = 6.5, 2.7 Hz, 18H), 0.86 (dd, *J* = 6.6, 2.4 Hz, 36H).
^{13}C NMR (101 MHz, $CDCl_3$) δ 165.13, 149.45, 148.88, 135.04, 129.91, 128.24, 120.65, 114.01, 113.95, 67.76, 67.68, 44.40, 39.26, 37.38, 37.35, 36.30, 36.24, 29.91, 27.98, 24.71, 22.70, 22.60, 19.67, 19.66.
HRMS (ESI): $C_{90}H_{147}N_3O_9$ $[M+Na]^+$, mass calculated: 1438.10, mass found: 1437.11.

Synthesis of C8-9

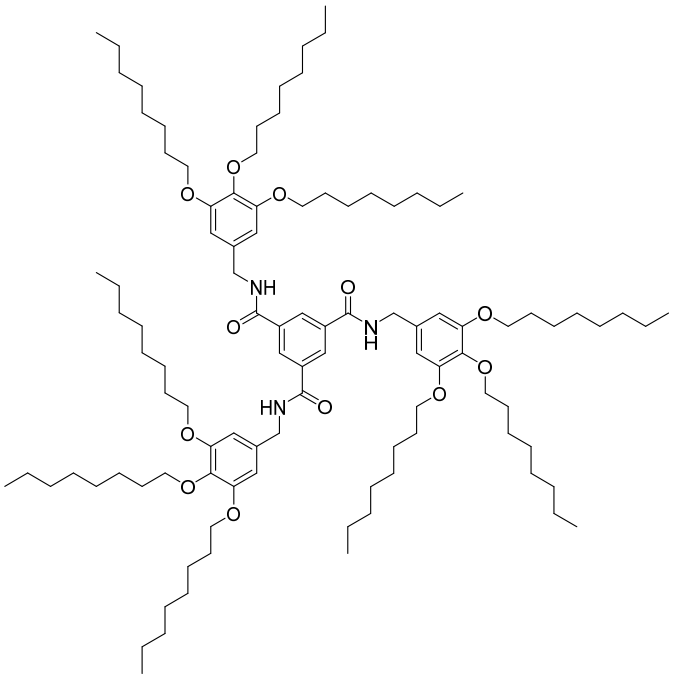

FTIR-ATR (neat): 3230, 3067, 2955, 2922, 2854, 1646, 1628, 1554, 1505, 1440, 1329, 1252, 1231, 1112 cm^{-1}.

^{1}H NMR (400 MHz, $CDCl_3$) δ 8.39 (s, 3H), 6.82 (s, 3H), 6.50 (s, 6H), 4.50 (d, *J* = 4.9 Hz, 6H), 4.13 – 3.79 (m, 19H), 1.87 – 1.63 (m, 19H), 1.55 – 1.39 (m, 19H), 1.39 – 1.12 (m, 78H), 0.99 – 0.70 (m, 29H).

^{13}C NMR (101 MHz, $CDCl_3$) δ 165.20, 153.42, 137.88, 134.85, 132.23, 128.38, 106.81, 77.00, 73.46, 69.20, 31.90, 31.82, 30.32, 29.55, 29.42, 29.37, 29.28, 26.10, 22.68, 22.66, 14.08.

HRMS (ESI): $C_{102}H_{171}N_3O_{12}Na$ $[M+Na]^+$, mass calculated: 1654.28, mass found: 1654.28. $C_{102}H_{171}N_3O_{12}K$ $[M+K]^+$, calculated: 1670.25, found: 1670.25.

Synthesis of Cit-9

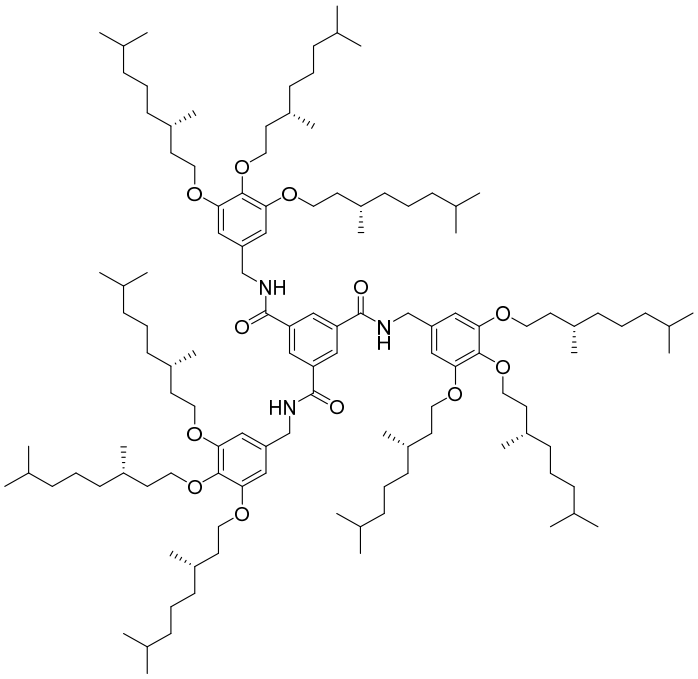

FTIR-ATR (neat): 3317, 2953, 2925, 2869, 1662, 1591, 1535, 1504, 1463, 1438, 1230, 1113 cm^{-1}.

^{1}H NMR (400 MHz, $CDCl_3$) δ 8.37 (s, 3H), 6.57 (t, *J* = 5.5 Hz, 3H), 6.53 (s, 6H), 4.53 (d, *J* = 5.4 Hz, 6H), 4.13 – 3.80 (m, 18H), 1.94 – 1.77 (m, 9H), 1.77 – 1.63 (m, 8H), 1.63 – 1.45 (m, 23H), 1.45 – 1.21 (m, 25H), 1.21 – 1.04 (m, 23H), 0.92 (d, *J* = 6.6 Hz, 18H), 0.92 (d, *J* = 6.6 Hz, 9H), 0.86 (d, *J* = 6.7 Hz, 48H).

^{13}C NMR (101 MHz, $CDCl_3$) δ 165.00, 153.50, 137.99, 134.97, 132.18, 128.25, 77.00, 71.70, 67.49, 39.37, 39.27, 37.54, 37.40, 37.35, 36.44, 29.80, 29.71, 27.98, 24.73, 24.71, 22.71, 22.62, 22.60, 19.58, 19.55.

HRMS (ESI): $C_{120}H_{207}N_3O_{12}Na$ $[M+Na]^+$, mass calculated: 1906.56, mass found: 1906.57.

Synthesis of Sym-C8-6

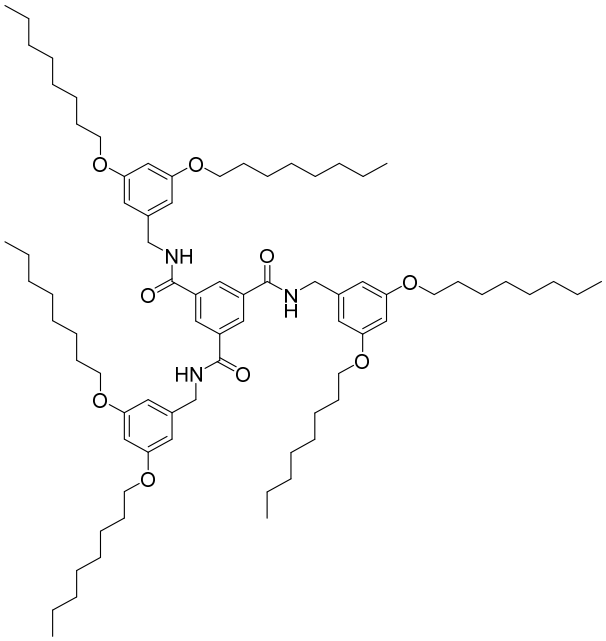

FTIR-ATR (neat): 3330, 2925, 2855, 1664, 1596, 1531, 1460, 1291, 1166, 1060 cm^{-1}.

^{1}H NMR (400 MHz, $CDCl_3$) δ 8.35 (s, 3H), 6.73 (t, J = 5.6 Hz, 3H), 6.44 (d, J = 2.2 Hz, 6H), 6.35 (t, J = 2.2 Hz, 3H), 4.53 (d, J = 5.5 Hz, 6H), 3.90 (t, J = 6.6 Hz, 12H), 1.85 – 1.65 (m, 12H), 1.52 – 1.38 (m, 12H), 1.38 – 1.15 (m, 48H), 0.96 – 0.78 (m, 18H).

^{13}C NMR (101 MHz, $CDCl_3$) δ 165.31, 160.65, 139.47, 134.99, 128.29, 106.45, 100.46, 68.09, 44.62, 31.81, 29.36, 29.25, 29.23, 26.04, 22.65, 14.09.

HRMS (ESI): $C_{78}H_{123}N_3O_9$ $[M+H]^+$, calculated: 1246.93, found: 1246.95; $[M+Na]^+$, mass calculated: 1268.92, mass found: 1268.92.

Synthesis of Sym-Cit-6

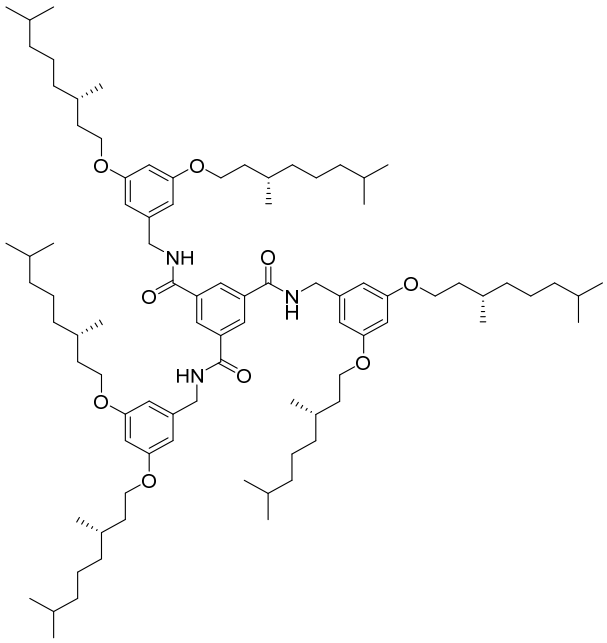

FTIR-ATR (neat): 3332, 3037, 2954, 2927, 2870, 1596, 1532, 1463, 1167 cm^{-1}.

^{1}H NMR (400 MHz, $CDCl_3$) δ 8.36 (s, 3H), 6.65 (t, J = 5.5 Hz, 3H), 6.45 (d, J = 2.2 Hz, 6H), 6.38 (t, J = 2.2 Hz, 3H), 4.54 (d, J = 5.5 Hz, 6H), 4.05 – 3.85 (m, 12H), 1.87 – 1.72 (m, 6H), 1.72 – 1.60 (m, 6H), 1.57 – 1.45 (m, 6H), 1.39 – 1.23 (m, 18H), 1.15 (s, 18H), 0.92 (d, J = 6.5 Hz, 18H), 0.86 (d, J = 6.6 Hz, 36H).

^{13}C NMR (101 MHz, $CDCl_3$) δ 165.20, 160.69, 139.38, 134.99, 128.27, 106.50, 100.52, 66.40, 44.69, 39.24, 37.31, 36.20, 29.82, 27.97, 24.65, 22.71, 22.60, 19.63.

HRMS (ESI): $C_{90}H_{147}N_3O_9$ $[M+H]^+$, calculated: 1416.12, found: 1415.13; $[M+Na]^+$, mass calculated: 1438.11, mass found: 1438.11.

Synthesis of 1

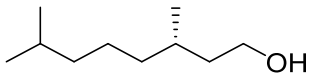

(*S*)-(−)-β-Citronellol (5 g, 31 mmol) was dissolved in ethyl acetate (20 mL) and palladium catalyst (Pd/C 10 % w/w, 250 mg) was added. The suspension and the headspace were deaerated by bubbling nitrogen gas through the suspension. The same operation was then performed with hydrogen. The reaction took place under H2 atmosphere (1 atm) using a balloon which was refilled with hydrogen when needed. When the reaction was complete nitrogen gas was used to replace hydrogen gas in the system. The mixture was subsequently filtered through celite and the solvent was removed under reduced pressure. The product was obtained as colourless liquid (4.14 g, 82 % yield).

FTIR-ATR (neat): 3340, 2954, 2926, 2870, 1457, 1052 cm^{-1}.

^{1}H NMR (400 MHz, $CDCl_3$) δ 3.73 – 3.60 (m, 2H), 1.67 – 1.44 (m, 3H), 1.43 – 1.18 (m, 5H), 1.18 – 1.01 (m, 3H), 0.89 (d, *J* = 6.6 Hz, 3H), 0.86 (d, *J* = 6.6 Hz, 6H).

^{13}C NMR (101 MHz, $CDCl_3$) δ 61.23, 39.93, 39.24, 37.35, 29.49, 27.95, 24.66, 22.67, 22.57, 19.61.

Synthesis of 2

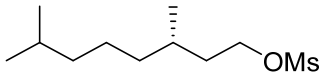

^{1}H NMR (400 MHz, $CDCl_3$) δ 4.32 – 4.20 (m, 2H), 3.00 (s, 3H), 1.85 (bs, 1H), 1.83 – 1.72 (m, 1H), 1.65 – 1.45 (m, 1H), 1.38 – 1.21 (m, 3H), 1.21 – 1.05 (m, 4H), 0.92 (d, J = 6.5 Hz, 4H), 0.86 (d, J = 6.6 Hz, 6H).

FTIR-ATR (neat): 2954, 2928, 2870, 1353, 1173, 940 cm^{-1}.

ESI-MS analysis: $C_{11}H_{24}O_3SNa$ $[M+Na]^+$, mass calculated: 259.13, mass found: 259.13.

Synthesis of 2b

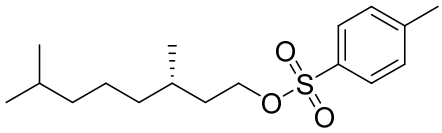

1 (10.0 g, 63.2 mmol) was dissolved in DCM (50 mL) and Et_3N was added (24.3 mL, 174 mmol). Then, the reaction mixture was cooled to 0 °C under an Ar atmosphere. Subsequently, tosyl chloride (13.5 g, 70.9 mmol) in DCM (40 mL) was slowly added dropwise. The mixture was left to heat up to room temperature and stirred for 23 hours, after which the mixture was evaporated to dryness. The product was obtained as a clear oil after purification through silica gel chromatography using 40% heptane in $CHCl_3$ as eluents with a 87% yield.

^{1}H NMR (400 MHz, $CDCl_3$) δ 7.79 (d, J = 8.4 Hz, 2H), 7.34 (d, J = 8.3 Hz, 2H), 4.06 (m, 2H), 2.45 (s, 3H), 1.70-1.63 (m, 1H), 1.52-1.37 (m, 3H), 1.30-1.00 (m, 6H), 0.85 (d, J = 6.7 Hz, 6H, 0.80 (d, J = 6.5 Hz, 3H).

Synthesis of 3a

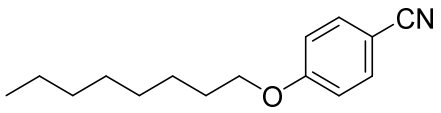

4-cyanophenol (0.63 g, 95 %, 5.00 mmol) and potassium carbonate (1.38 g, 10.00 mmol) were suspended in butanone (15 mL) and heated to reflux temperature under magnetic stirring. After 15 minutes at reflux temperature the 1-bromoctane (0.920 mL, 5.25 mmol) was added dropwise with a syringe. After 16 h a white suspension had been obtained. Water (50 mL) was added and the layers were separated in a separation funnel. The aqueous layer was extracted with ethyl acetate (3x10 mL) and the 4 organic layers were combined and washed with 1 M aqueous NaOH (2x10 mL) and brine (10 mL). After drying over anhydrous sodium sulfate the solvents were removed under reduced pressure. A yellow oil was obtained and used in the next step without further purification.

FTIR-ATR (neat): 2926, 2856, 2224, 1605, 1508, 1257, 1170 cm^{-1}.

^{1}H NMR (400 MHz, $CDCl_3$) δ 7.55 (d, *J* = 8.8 Hz, 2H), 6.92 (d, *J* = 8.8 Hz, 2H), 3.98 (t, *J* = 6.6 Hz, 2H), 1.95 – 1.56 (m, 2H), 1.55 – 1.09 (m, 10H), 0.96 – 0.73 (m, 3H).

^{13}C NMR (101 MHz, $CDCl_3$) δ 162.41, 133.88, 119.27, 115.12, 103.55, 77.00, 68.37, 31.72, 29.22, 29.13, 28.92, 25.87, 22.58, 14.03.

Synthesis of 3b

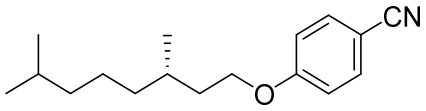

S-(+)-Citronellol (1.00 g, 6.32 mmol), 4-cyanophenol (0.75 g, 6.32 mmol) and diisopropyl azodicarboxylate (1.27 g, 6.32 mmol) were dissolved in dry THF (30 mL) under N_2 atmosphere. Next, the organic solution was cooled in an ice bath and triphenylphosphine (1.66 g, 6.32 mmol) was added. The reaction was allowed to reach room temperature and further stirred 24 hours. Once the reaction was completed, water was added (5 drops) and further stirred 1 hour more. Finally, THF was removed under reduced pressure and the solid obtained was redissolved in an ethyl acetate:hexane (3:7) (60 mL) in an ice bath over 1 hour. The white precipitate obtained was filtered through silica gel and rinsed several times with the same solvent. Finally, the solvent was removed under reduced pressure giving rise to a yellow liquid, which was purified through silica gel column using hexane:ethyl acetate 98:2. **3b** was obtained as a colourless liquid with 61 % yield (1. 06 g, 4.08 mmol).

FTIR-ATR (neat): 2953, 2927, 2870, 2224, 1605, 1508, 1257, 1171 cm^{-1}.

^{1}H NMR (400 MHz, CDCl3) δ 7.73 – 7.42 (m, 2H), 7.07 – 6.75 (m, 2H), 4.26 – 3.82 (m, 2H), 1.90 – 1.77 (m, 1H), 1.73 – 1.44 (m, 3H), 1.41 – 1.05 (m, 5H), 0.94 (d, *J* = 6.5 Hz, 3H), 0.87 (d, *J* = 6.6 Hz, 6H).

^{13}C NMR (101 MHz, $CDCl_3$) δ 162.40, 133.91, 119.28, 115.16, 103.61, 66.74, 39.17, 37.18, 35.85, 29.75, 27.93, 24.60, 22.66, 22.56, 19.57.

Synthesis of 4a

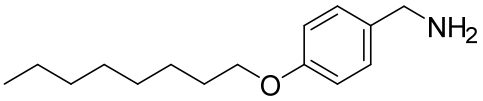

A dry round-bottom flask was flushed with dry nitrogen gas for 20 min and $LiAlH_4$ (1 M in THF, 4.33 mL) was added via syringe. The reagent was diluted with dry diethyl ether (10 mL) and the mixture was stirred at 0-4 ºC under nitrogen for 10 min. Then a solution of **3a** (1.00 g, 4.33 mmol) in dry diethyl ether (5 mL) was dropwise added. The mixture turned yellow. After overnight reaction the mixture was diluted with Et_2O (10 mL) and NaOH (3.60 mL) was added in an ice bath to precipitate inorganic salts. After 1 hour stirring the suspension was vacuum filtered and the solid rinsed several times with Et_2O. The solvent was removed under reduced pressure giving rise a yellow oil, which was purified through silica gel column using $CHCl_3$:MeOH:NH_3 90:9:1 as eluent. **4a** was obtained as a white waxy solid with a 64 % yield (653 mg, 2.77 mmol).

FTIR-ATR (neat): 3271, 2918, 2852, 1511, 1242 cm^{-1}.

^{1}H NMR (400 MHz, $CDCl_3$) δ 7.22 (d, *J* = 8.6 Hz, 2H), 6.85 (d, *J* = 8.6 Hz, 2H), 3.93 (t, *J* = 6.6 Hz, 2H), 3.79 (s, 2H), 2.54 (s, 2H), 1.76 (dq, *J* = 8.1, 6.6 Hz, 2H), 1.50 – 1.39 (m, 2H), 1.39 – 1.12 (m, 13H), 0.95 – 0.78 (m, 3H).

^{13}C NMR (101 MHz, $CDCl_3$) δ 158.21, 134.06, 128.46, 114.54, 68.03, 45.53, 31.79, 29.34, 29.26, 29.22, 26.03, 22.63, 14.07.

ESI-MS analysis: $C_{15}H_{23}O$ $[M\text{-}NH_2]^+$, mass calculated: 219.17, mass found: 219.17.

Synthesis of 4b

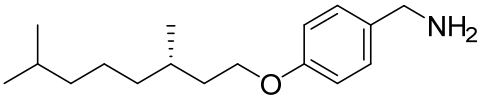

3b (900 mg, 3.46 mmol) was dissolved in dry Et_2O (10 mL) under N_2 and cooled down in an ice bath. Then, $LiAlH_4$ (4.15 mL, 1 M THF) was dropwise added turning the colourless solution to a pale-yellow suspension together with gas release. The reaction was gradually warmed to room temperature and further stirred overnight. The crude was diluted with Et_2O and NaOH (3.60 mL) was added in an ice bath to precipitate inorganic salts. After 1 hour stirring, the suspension was vacuum filtered and the solid rinsed several times with Et_2O. The solvent was removed under reduced pressure giving rise a yellow oil, which was purified through silica gel column using $CHCl_3$:MeOH:NH_3 90:9:1 as eluent. **4b** was obtained as a yellowish liquid with 86 % yield (770 mg, 2.94 mmol).

FTIR-ATR (neat): 3277, 2924, 2869, 1513, 1245 cm^{-1}.

^{1}H NMR (400 MHz, $CDCl_3$) δ 7.25 – 7.19 (m, 2H), 6.90 – 6.83 (m, 2H), 4.02 – 3.88 (m, 2H), 3.80 (s, 2H), 3.65 (bs, 2H), 1.87 – 1.74 (m, 1H), 1.74 – 1.43 (m, 3H), 1.39 – 1.21 (m, 3H), 1.21 – 1.06 (m, 3H), 0.93 (d, *J* = 6.5 Hz, 3H), 0.87 (d, *J* = 6.6 Hz, 6H).

^{13}C NMR (101 MHz, $CDCl_3$) δ 158.45, 132.46, 128.83, 114.62, 66.34, 45.11, 39.23, 37.29, 36.20, 29.84, 27.95, 24.64, 22.69, 22.59, 19.63.

ESI-MS analysis: $C_{17}H_{27}O$ $[M\text{-}NH_2]^+$, mass calculated: 247.21, mass found: 247.20.

Synthesis of 5a

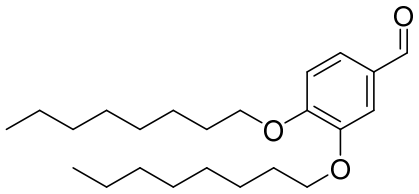

3,4-dihydroxybenzaldehyde (540 mg, 3.90 mmol) was dissolved in 30 mL of DMF in a Schlenk flask under argon atmosphere. To the solution were added (*S*)-3,7-dimethyloctyl 4-methylbenzenesulfonate (2.05 eq., 2.5 g, 8.0 mmol) and potassium carbonate (3.5 eq., 1.89 g, 13.7 mmol) and the reaction mixture refluxed for 16 hours. The solvent was removed under reduced pressure, the mixture dissolved in chloroform and extracted with water (3 x 20 mL). The organic phase was dried over magnesium sulfate, filtered and the solvent removed. The material was purified by column chromatography with a Biotage Isolera One and a solvent gradient of DCM in Heptane (30 to 50%) to yield **5a** as a yellow oil (3.19 mmol, yield: 82%)

FTIR-ATR (neat): 2921, 2851, 1685, 1589, 1510, 1271, 1236, 1133 cm^{-1}.

^{1}H NMR (400 MHz, $CDCl_3$) δ 9.83 (s, 1H), 7.64 – 7.32 (m, 2H), 6.95 (d, *J* = 8.1 Hz, 1H), 4.08 (t, *J* = 6.6 Hz, 2H), 4.04 (t, *J* = 6.6 Hz, 2H), 1.93 – 1.76 (m, 4H), 1.56 – 1.42 (m, 4H), 1.42 – 1.19 (m, 16H), 0.97 – 0.81 (m, 6H).

^{13}C NMR (101 MHz, $CDCl_3$) δ 191.00, 154.65, 149.40, 129.82, 126.59, 111.70, 110.89, 69.11, 69.09, 31.80, 31.78, 29.32, 29.30, 29.25, 29.23, 29.05, 28.96, 25.97, 25.93, 22.65, 14.09.

ESI-MS analysis: $C_{23}H_{38}O_3Na$ $[M+Na]^+$, mass calculated: 385.27, mass found: 385.27.

Synthesis of 5b

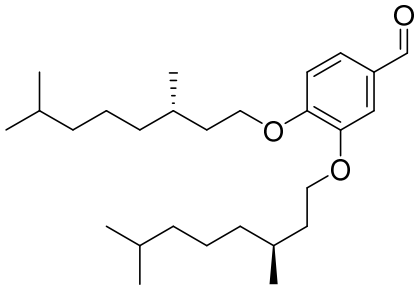

3,4-dihydroxybenzaldehyde (1 g, 7.24 mmol) was dissolved in 40 mL of DMF in a Schlenk flask under argon atmosphere. To the solution 1-bromooctane (2.05 eq., 2.87 g, 14.9 mmol) and potassium carbonate (3.5 eq., 3.5 g, 25.3 mmol) were added and the reaction mixture refluxed for 16 hours. The solvent was removed under reduced pressure, the mixture dissolved in chloroform and extracted with water (3x 20 mL). The organic phase was dried over magnesium sulfate, filtered and the solvent removed. The material was purified by column chromatography with a Biotage Isolera One and a solvent gradient of DCM in Heptane (30 to 50%) to yield 2.45 g of **5b** as a crystalline solid (6.76 mmol, yield: 93%).

FTIR-ATR (neat): 2926, 2869, 1689, 1595, 1508, 1265, 1132 cm^{-1}.

^{1}H NMR (400 MHz, $CDCl_3$) δ 9.83 (s, 1H), 7.47 – 7.32 (m, 2H), 6.96 (d, *J* = 8.1 Hz, 1H), 4.21 – 3.96 (m, 4H), 1.98 – 1.79 (m, 2H), 1.77 – 1.59 (m, 4H), 1.59 – 1.43 (m, 2H), 1.42 – 1.05 (m, 12H), 0.96 (d, *J* = 6.4 Hz, 3H), 0.95 (d, *J* = 6.4 Hz, 3H), 0.86 (d, *J* = 6.6 Hz, 12H).
^{13}C NMR (101 MHz, $CDCl_3$) δ 191.03, 154.62, 149.42, 129.82, 126.64, 111.60, 110.68, 67.50, 67.47, 39.22, 39.20, 37.28, 35.99, 35.86, 29.96, 29.92, 27.97, 24.71, 24.70, 22.69, 22.59, 19.70, 19.68.
ESI-MS analysis: $C_{27}H_{46}O_3Na$ $[M+Na]^+$, mass calculated: 441.33, mass found: 441.33.

Synthesis of 6a

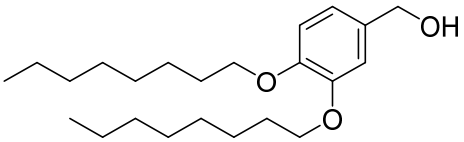

Aldehyde **5a** (1.42 g, 3.91 mmol) was dissolved in dry THF (30 mL), and the mixture was stirred at 0-4 ºC. After 10 min, $NaBH_4$ (0.30 g, 37.83 mmol) was added. After 2 h the reaction was completed by TLC and the mixture was quenched with the addition of aqueous $NaHCO_3$ (5 % w/w, 10 mL). After addition of water (20 mL) the mixture was extracted with CH_2Cl_2 (3 x 10 mL). The organic layers were combined, treated with brine (10 mL) and dried over anhydrous Na_2SO_4. After filtration and removal of the solvents under reduced pressure, the crude was obtained as a thick oil that slowly solidified to yield a waxy solid. The product was purified by flash column chromatography using an eluent gradient from hexanes (100 %) to hexanes/ethyl acetate (5/1). **6a** was obtained as a yellowish liquid with 85 % yield (1.21 g, 3.32 mmol).
FTIR-ATR (neat): 3282, 2921, 2845, 1593, 1518, 1467, 1429, 1263, 1139 cm^{-1}.
^{1}H NMR (400 MHz, $CDCl_3$) δ 7.03 – 6.89 (m, 1H), 6.89 – 6.71 (m, 2H), 4.57 (d, *J* = 19.6 Hz, 2H), 3.99 (t, *J* = 6.6 Hz, 2H), 3.98 (t, *J* = 6.7 Hz, 2H), 2.02 – 1.72 (m, 4H), 1.65 (s, 1H), 1.55 – 1.40 (m, 4H), 1.40 – 1.05 (m, 18H), 1.00 – 0.69 (m, 6H).
^{13}C NMR (101 MHz, $CDCl_3$) δ 149.33, 148.71, 133.69, 119.56, 113.85, 112.97, 69.42, 69.21, 65.36, 31.81, 29.37, 29.29, 29.27, 26.02, 26.01, 22.65, 14.08.
ESI-MS analysis: $C_{23}H_{40}O_3Na$ $[M+Na]^+$, mass calculated: 387.29, mass found: 387.28.

Synthesis of 6b

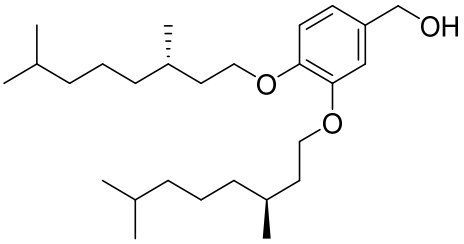

6b was synthesized according to the procedure described for **6a**, using **5b** as starting material (1.15 g, 2.75 mmol), and $NaBH_4$ as reductant (0.21 g, 5.50 mmol). **6b** was obtained as a colourless liquid with 84 % yield (965 mg, 2.31 mmol).

FTIR-ATR (neat): 3372, 2925, 2869, 1512, 1463, 2621, 1135 cm^{-1}.

^{1}H NMR (400 MHz, $CDCl_3$) δ 6.96 – 6.79 (m, 6H), 4.61 (s, 2H), 4.16 – 3.80 (m, 8H), 1.96 – 1.77 (m, 3H), 1.76 – 1.42 (m, 13H), 1.42 – 1.21 (m, 12H), 1.21 – 1.03 (m, 11H), 0.98 – 0.90 (m, 8H), 0.90 – 0.82 (m, 12H).

^{13}C NMR (101 MHz, $CDCl_3$) δ 149.35, 148.72, 133.63, 119.55, 113.70, 112.83, 67.73, 67.53, 65.42, 39.26, 37.35, 36.26, 36.24, 36.20, 36.16, 29.93, 29.91, 27.98, 24.72, 24.71, 22.70, 22.60, 19.69.

Synthesis of 7a

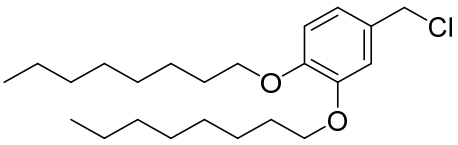

Alcohol **6a** (1.15 g, 3.16 mmol) was dissolved in dry CH_2Cl_2 (10 mL), and the solution was stirred at 0-4 ºC. After 10 min, thionyl chloride (0.32 mL, 4.42 mmol) was added dropwise. After 2 h stirring in a water-ice bath the reaction was still incomplete by TLC and the mixture was allowed to react for 1 h at room temperature before adding another portion of $SOCl_2$ (0.32 mL) at 0-4 ºC. After 2 h the solvents were removed under reduced pressure and the crude was dried under vacuum. The yellow crude finally solidified to a waxy yellowish solid, which was used in the next reaction without any purification.

FTIR-ATR (neat): 2922, 2850, 1603, 1467, 1392, 1270, 1234, 1132 cm^{-1}.

^{1}H NMR (400 MHz, CDCl3) δ 6.94 – 6.86 (m, 2H), 6.86 – 6.79 (m, 1H), 4.55 (s, 2H), 4.01 (d, *J* = 6.6 Hz, 2H), 3.98 (d, *J* = 6.7 Hz, 2H), 1.90 – 1.74 (m, 5H), 1.53 – 1.41 (m, 4H), 1.41 – 1.13 (m, 19H), 0.99 – 0.79 (m, 7H).

^{13}C NMR (101 MHz, $CDCl_3$) δ 149.37, 149.23, 129.96, 121.23, 114.20, 113.45, 69.26, 46.75, 31.81, 29.36, 29.26, 29.22, 26.01, 22.66, 14.09.

Synthesis of 7b

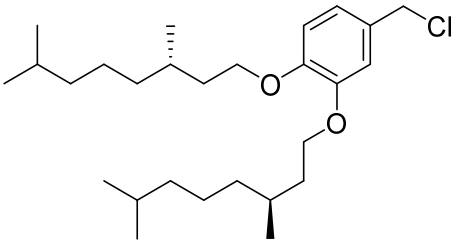

7b was synthesized according to the procedure described for **7a**, using **6b** as starting material (1.00 g, 2.38 mmol), and $SOCl_2$ (0.48 mL, 6.66 mmol) in two portions.

FTIR-ATR (neat): 2952, 2925, 2868, 1511, 1467, 1262 cm^{-1}.

^{1}H NMR (400 MHz, $CDCl_3$) δ 6.95 – 6.86 (m, 2H), 6.86 – 6.77 (m, 1H), 4.55 (s, 2H), 4.10 – 3.91 (m, 4H), 1.95 – 1.80 (m, 2H), 1.79 – 1.45 (m, 10H), 1.41 – 1.21 (m, 6H), 1.21 – 1.05 (m, 7H), 0.95 (d, *J* = 6.5 Hz, 3H), 0.94 (d, *J* = 6.5 Hz, 3H), 0.87 (d, *J* = 6.6 Hz, 6H), 0.87 (d, *J* = 6.6 Hz, 6H).

^{13}C NMR (101 MHz, $CDCl_3$) δ 149.36, 149.22, 129.93, 121.21, 114.06, 113.31, 67.58, 46.78, 39.25, 37.34, 37.33, 36.21, 36.16, 29.92, 29.91, 27.98, 24.73, 24.71, 22.70, 22.60, 19.70, 19.67.
ESI-MS analysis: $C_{27}H_{47}O_2$ $[M\text{-}Cl]^+$, mass calculated: 403.36, mass found: 403.36.

Synthesis of 8a

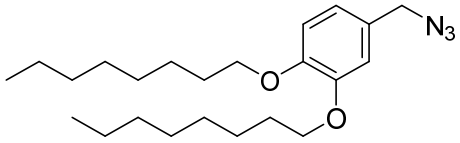

NaN_3 (0.41 g, 6.32 mmol) was added to a solution of **7a** (theor 3.16 mmol) in dry DMF (9 mL). The mixture was heated to 80 ºC and allowed to react overnight (18 h). The mixture was allowed to reach room temperature, water (30 mL) was added and the product was extracted with a 7/3 mixture of hexanes and ethyl acetate (3 x 20 mL). The organic layers were combined, treated with brine (20 mL), dried over anhydrous Na_2SO_4, filtered and submitted to reduced pressure to remove the solvents.
The product was purified by flash column chromatography using an eluent gradient from hexanes to hexanes/ethyl acetate 98/2.
FTIR-ATR (neat): 2955, 2917, 2849, 2107, 1517, 1467, 1430, 1263, 1238, 1137 cm^{-1}.
^{1}H NMR (400 MHz, $CDCl_3$) δ 7.01 – 6.68 (m, 3H), 4.25 (s, 2H), 4.00 (t, *J* = 6.7 Hz, 2H), 3.99 (t, *J* = 6.7 Hz, 2H), 1.89 – 1.73 (m, 4H), 1.54 – 1.41 (m, 4H), 1.41 – 1.17 (m, 14H), 0.99 – 0.79 (m, 6H).
^{13}C NMR (101 MHz, $CDCl_3$) δ 149.32, 149.24, 127.79, 120.93, 113.89, 113.64, 69.29, 69.27, 54.78, 31.81, 29.37, 29.26, 26.01, 22.66, 14.08.
ESI-MS analysis: $C_{23}H_{39}N_3O_2Na$ $[M+Na]^+$, mass calculated: 412.29, mass found: 412.29.

Synthesis of 8b

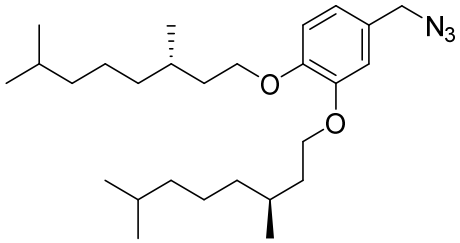

8b was synthesized according to the procedure described for **8a**, using **7b** as starting material (theor 2.38 mmol), and NaN_3 (0.31 g, 4.76 mmol).
FTIR-ATR (neat): 2953, 2925, 2869, 2095, 1512, 1467, 1429, 1262, 1236, 1138 cm^{-1}.
^{1}H NMR (400 MHz, $CDCl_3$) δ 6.93 – 6.72 (m, 3H), 4.25 (s, 2H), 4.14 – 3.75 (m, 3H), 2.01 – 1.76 (m, 2H), 1.75 – 1.44 (m, 5H), 1.39 – 1.05 (m, 11H), 0.95 (d, *J* = 6.5 Hz, 3H), 0.94 (d, *J* = 6.5 Hz, 3H), 0.87 (d, *J* = 6.6 Hz, 12H).
^{13}C NMR (101 MHz, $CDCl_3$) δ 149.32, 149.23, 127.76, 120.89, 113.75, 113.49, 67.61, 67.58, 54.80, 39.24, 37.34, 36.21, 36.19, 29.91, 27.98, 24.71, 22.69, 22.59, 19.70, 19.69.

ESI-MS analysis: $C_{27}H_{47}N_3O_2Na$ $[M+Na]^+$, mass calculated: 468.36, mass found: 468.35.

Synthesis of 9a

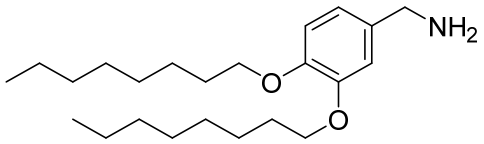

Azide **8a** (0.50 g, 1.29 mmol) was dissolved in dry THF (10 mL) under N_2 atmosphere. After 10 min stirring at 0-4 °C $LiAlH_4$ (1 M in THF, 1.54 mL) was added dropwise via syringe. After 2 h stirring at 0-4 °C no starting material was observed by TLC. The mixture was diluted with diethyl ether (20 mL), and water (0.100 mL) and aqueous 1 M NaOH (0.100 mL) were consecutively added at 0-4 ºC. After 30 min water (0.100 mL) was added and the mixture was stirred at room temperature for 15 min. The mixture was then filtered and the filter cake was washed with diethyl ether (3 x 5 mL). The filtrate was submitted to reduced pressure and the crude was obtained as a waxy yellowish solid after slow solidification. The product was used without further purification.

FTIR-ATR (neat): 3321, 2921, 2850, 1512, 1467, 1268, 1253, 1232, 1135 cm^{-1}.

^1H NMR (400 MHz, $CDCl_3$) δ 6.88 – 6.63 (m, 3H), 4.57 – 4.38 (m, 2H), 4.15 – 3.73 (m, 4H), 2.09 – 1.58 (m, 4H), 1.55 – 1.38 (m, 4H), 1.38 – 1.13 (m, 16H), 0.99 – 0.49 (m, 6H).

Synthesis of 9b

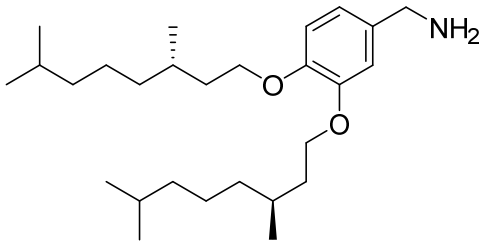

9b was synthesized according to the procedure described for **9a**, using **8b** as starting material (0.50 g, 1.12 mmol), and $LiAlH_4$ as reductant (1 M in THF, 1.35 mL). The product, a yellow oil, was used without further purification.

FTIR-ATR (neat): 2925, 2869, 1510, 1263, 1136 cm^{-1}.

^1H NMR (400 MHz, $CDCl_3$) δ 6.88 – 6.63 (m, 3H), 4.57 – 4.38 (m, 1H), 4.15 – 3.73 (m, 4H), 2.09 – 1.58 (m, 4H), 1.55 – 1.38 (m, 4H), 1.38 – 1.13 (m, 16H), 0.99 – 0.49 (m, 6H).

ESI-MS analysis: $C_{27}H_{49}NO_2$ $[M]^+$, mass calculated: 419.38, mass found: 419.37.

Synthesis of 10a

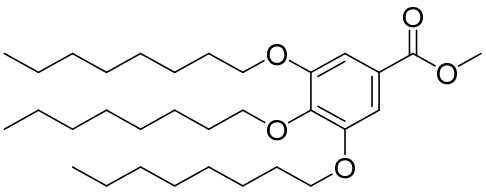

Methyl 3,4,5-trihydroxybenzoate (0.74 g, 4 mmol) and anhydrous potassium carbonate (3.32 g, 24 mmol) were suspended in anhydrous DMF (20 mL). The suspension was heated to 80 °C and after 1 h stirring, 1-bromooctane (2.3 mL 13.2 mmol) was added dropwise via syringe. After 66 h the mixture (dark color) was allowed to reach room temperature and then poured into water (60 mL). The product was extracted with a 70/30 mixture of hexanes and ethyl acetate (3 x 30 mL). The combined organic layers were treated with brine (30 mL), dried over anhydrous Na_2SO_4, filtered and submitted to reduced pressure. The product was then purified by flash column chromatography using an eluent gradient from hexanes (100 %) to a mixture of hexanes and ethyl acetate (95/5). **10a** was obtained as a colourless oil in 71 % yield (1.47 g, 2.82 mmol).

FTIR-ATR (neat): 2924, 2855, 1722, 1587, 1429, 1335, 1217, 1111 cm^{-1}.

^1H NMR (400 MHz, $CDCl_3$) δ 7.27 (d, *J* = 4.6 Hz, 3H), 4.03 (t, *J* = 6.6 Hz, 2H), 4.02 (t, *J* = 6.5 Hz, 4H), 3.90 (s, 3H), 1.90 – 1.69 (m, 6H), 1.55 – 1.42 (m, 6H), 1.42 – 1.16 (m, 24H), 0.99 – 0.78 (m, 9H).

^{13}C NMR (101 MHz, $CDCl_3$) δ 166.92, 152.79, 142.35, 124.63, 107.96, 73.47, 69.15, 52.08, 31.88, 31.82, 30.31, 29.50, 29.35, 29.33, 29.29, 29.28, 26.06, 26.03, 22.68, 22.66, 14.08.

ESI-MS analysis: $C_{32}H_{57}O_5$ $[M+H]^+$, mass calculated: 521.42, mass found: 521.43

Synthesis of 10b

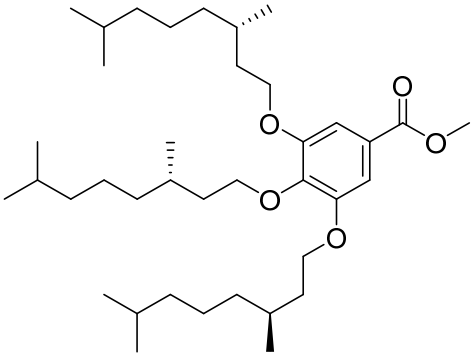

10b was synthesized according to the procedure described for **10a**, using methyl 3,4,5-trihydroxybenzoate (0.74 g, 4 mmol), potassium carbonate (3.32 g, 24 mmol), and (*S*)-3,7-dimethyl-1-octyl methylsulfonate (4.58 g, 19.4 mmol) in dry DMF (20 mL). The product was purified by flash column chromatography using an eluent gradient from hexanes to a 98/2 mixture of hexanes and ethyl acetate, and obtained as a colourless oil (1.24 g, 2.05 mmol, 51 % yield).

FTIR-ATR (neat): 2953, 2869, 1723, 1587, 1435, 1333, 1212, 1112 cm^{-1}.

^{1}H NMR (400 MHz, $CDCl_3$) δ 7.26 (s, 2H), 4.24 – 3.95 (m, 6H), 3.89 (s, 3H), 1.93 – 1.76 (m, 3H), 1.76 – 1.66 (m, 3H), 1.66 – 1.44 (m, 4H), 1.42 – 1.22 (m, 6H), 1.22 – 1.05 (m, 9H), 0.94 (d, *J* = 6.6 Hz, 6H), 0.92 (d, *J* = 6.6 Hz, 3H), 0.89 – 0.78 (m, 18H).
^{13}C NMR (101 MHz, $CDCl_3$) δ 166.91, 152.80, 142.31, 124.64, 107.90, 71.66, 67.42, 52.06, 39.33, 39.24, 37.47, 37.31, 36.29, 29.80, 29.61, 27.96, 24.71, 24.69, 22.68, 22.59, 22.57, 19.56, 19.53.
ESI-MS analysis: $C_{38}H_{68}O_5Na[M+Na]^+$, mass calculated: 627.50, mass found: 627.50.

Synthesis of 11a

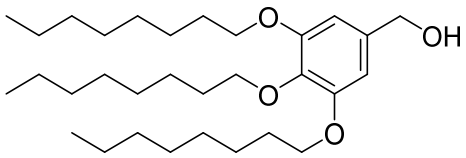

10a (1.43 g, 2.76 mmol) was dissolved in dry diethyl ether (20 mL), and the colourless solution was stirred at 0-4 °C for 10 min. $LiAlH_4$ (1 M in THF, 2.8 mL) was then added dropwise via syringe (gas evolution). The reaction mixture was allowed to react while the water-ice bath was consumed. After 3 h the mixture was diluted with diethyl ether (40 mL), cooled down to 0-4 °C. Deionized water (0.10 mL) and 1 M NaOH (0.10 mL) were consecutively added. The mixture was stirred for 30 min and other 0.10 mL deionized water were added. The mixture was stirred for 30 min at room temperature and then filtered to remove the formed salts. Evaporation of the solvents under reduced pressure afforded **11a** as a white waxy solid (1.20 g, 2.43 mmol, 88 % yield).
FTIR-ATR (neat): 3289, 2921, 2852, 1590, 1437, 1228, 1113 cm^{-1}.
^{1}H NMR (400 MHz, $CDCl_3$) δ 6.56 (s, 2H), 4.59 (s, 2H), 3.97 (t, *J* = 6.5 Hz, 4H), 3.93 (t, *J* = 6.6 Hz, 2H), 1.92 – 1.65 (m, 6H), 1.52 – 1.39 (m, 6H), 1.39 – 1.09 (m, 24H), 1.00 – 0.78 (m, 9H).
^{13}C NMR (101 MHz, $CDCl_3$) δ 153.27, 137.62, 135.98, 109.93, 105.36, 73.43, 69.11, 65.68, 31.91, 31.83, 30.32, 29.55, 29.41, 29.37, 29.36, 29.36, 29.29, 26.12, 26.09, 22.69, 22.67, 14.09.
ESI-MS analysis: $C_{31}H_{57}O_4$ $[M+H]^+$, mass calculated: 493.43, mass found: 493.42.

Synthesis of 11b

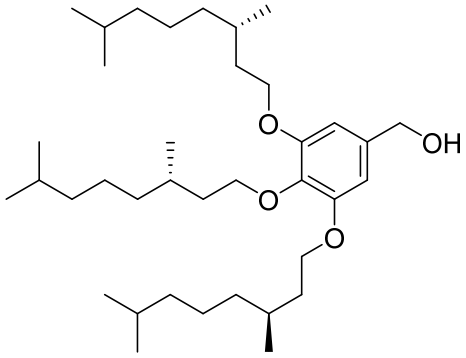

11b was prepared according the same procedure as **11a** using **10b** (1.15 g, 1.90 mmol) as starting material and $LiAlH_4$ (1 M in THF, 1.90 mL). The product was purified by flash column chromatography

using an eluent gradient from hexanes to hexanes/ethyl acetate (95/5). The product was obtained as a colorless oil (0.93 g, 1.61 mmol, 85 % yield).

FTIR-ATR (neat): 3357, 2953, 2925, 2869, 1590, 1457, 1437, 1232, 1114 cm^{-1}.

^{1}H NMR (400 MHz, $CDCl_3$) δ 6.57 (s, 2H), 4.59 (s, 2H), 4.15 – 3.86 (m, 6H), 1.93 – 1.76 (m, 3H), 1.76 – 1.64 (m, 3H), 1.64 – 1.43 (m, 6H), 1.43 – 1.21 (m, 9H), 1.21 – 1.04 (m, 9H), 0.93 (d, *J* = 6.6 Hz, 9H), 0.86 (d, *J* = 6.6 Hz, 18H).

^{13}C NMR (101 MHz, $CDCl_3$) δ 153.27, 137.52, 136.04, 105.24, 71.65, 67.36, 65.65, 39.36, 39.27, 37.52, 37.35, 36.41, 29.82, 29.69, 27.98, 27.96, 24.72, 24.71, 22.70, 22.59, 19.63, 19.57.

ESI-MS analysis: $C37H68O4Na$ $[M+Na]^+$, mass calculated: 599.50, mass found: 599.50.

Synthesis of 12a

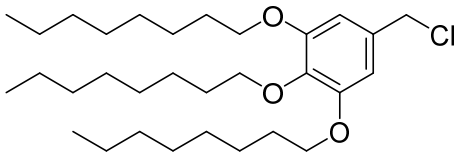

11a (1.14 g, 2.32 mmol) was dissolved in dry dichloromethane (10 mL) and stirred for 10 min at 0-4 °C under nitrogen. Thionyl chloride (0.24 mL, 3.25 mmol) was added dropwise followed by DMF (3 drops). The colourless solution turned yellow. After 1 h stirring 0-4 °C the solvents were removed under reduced pressure. Additional dichloromethane was used to favour distillation of the excess of thionyl chloride. **12a** was obtained as a yellow oil and directly used in the next reaction.

FTIR-ATR (neat): 2924, 2854, 1591, 1506, 1437, 1335, 1235, 1113 cm^{-1}.

^{1}H NMR (400 MHz, $CDCl_3$) δ 6.57 (s, 2H), 4.51 (s, 2H), 3.97 (t, *J* = 6.5 Hz, 4H), 3.94 (t, *J* = 6.6 Hz, 2H), 1.88 – 1.67 (m, 6H), 1.53 – 1.40 (m, 6H), 1.40 – 1.10 (m, 24H), 0.98 – 0.75 (m, 9H).

^{13}C NMR (101 MHz, $CDCl_3$) δ 153.19, 138.24, 132.30, 106.98, 71.66, 67.39, 46.99, 39.35, 39.26, 39.17, 37.50, 37.33, 37.31, 37.06, 36.45, 36.36, 29.80, 29.67, 27.98, 24.73, 24.70, 22.70, 22.59, 19.58.

ESI-MS analysis: $C_{31}H_{55}ClO_3Na$ $[M+Na]^+$, mass calculated: 533.37, mass found: 533.37.

Synthesis of 12b

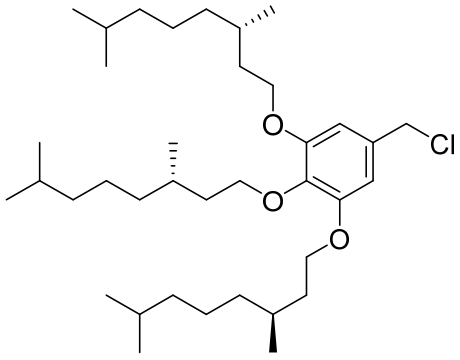

The product was prepared following the same procedure as for **12a** using **11b** (0.88 g, 1.53 mmol), thionyl chloride (0.16 mL, 2.14 mmol), DMF (3 drops) and dry dichloromethane (10 mL).
FTIR-ATR (neat): 2953, 2925, 2869, 1591, 1505, 141464, 1440, 1236, 1114 cm^{-1}.
^{1}H NMR (400 MHz, $CDCl_3$) δ 6.58 (s, 2H), 4.52 (s, 2H), 4.28 – 3.80 (m, 6H), 1.95 – 1.76 (m, 3H), 1.75 – 1.40 (m, 9H), 1.40 – 1.21 (m, 9H), 1.21 – 1.03 (m, 9H), 1.00 – 0.89 (m, 9H), 0.87 (d, *J* = 6.6 Hz, 12H), 0.86 (d, *J* = 6.4 Hz, 6H).
^{13}C NMR (101 MHz, $CDCl_3$) δ 153.19, 138.24, 132.30, 106.98, 71.66, 67.39, 46.99, 39.35, 39.26, 37.50, 37.34, 37.34, 37.31, 36.36, 29.80, 29.67, 27.98, 24.73, 24.70, 22.70, 22.61, 22.59, 19.58.
ESI-MS analysis: C37H67ClO3 $[M+Na]^+$, mass calculated: 617.47, mass found: 617.46.

Synthesis of 13a

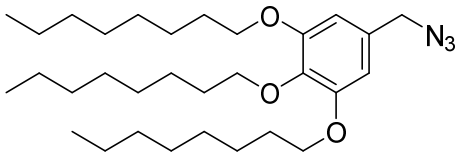

The product was prepared following the same procedure as for **8a** using **12a** (theor 2.32 mmol) and NaN_3 (0.30 g, 4.64 mmol). The product was purified by flash column chromatography using an eluent gradient from hexanes to hexanes/ethyl acetate 99/1. **13a** was obtained as a colourless liquid with 76 % yield (0.93 g, 1.79 mmol).
FTIR-ATR (neat): 2924, 2855, 2097, 1590, 1507, 1436, 1335, 1234, 1113 cm^{-1}.
^{1}H NMR (400 MHz, $CDCl_3$) δ 6.49 (s, 2H), 4.24 (s, 2H), 3.97 (t, *J* = 6.5 Hz, 4H), 3.94 (t, *J* = 6.6 Hz, 2H), 1.91 – 1.67 (m, 6H), 1.53 – 1.40 (m, 6H), 1.40 – 1.13 (m, 24H), 1.01 – 0.76 (m, 9H).
^{13}C NMR (101 MHz, $CDCl_3$) δ 153.32, 138.08, 130.32, 106.57, 73.40, 69.13, 55.17, 31.90, 31.82, 30.31, 29.54, 29.37, 29.35, 29.28, 26.09, 26.08, 22.69, 22.67, 14.09.
ESI-MS analysis: $C_{31}H_{55}N_3O_3Na$ $[M+Na]^+$, mass calculated: 540.41, mass found: 540.41.

Synthesis of 13b

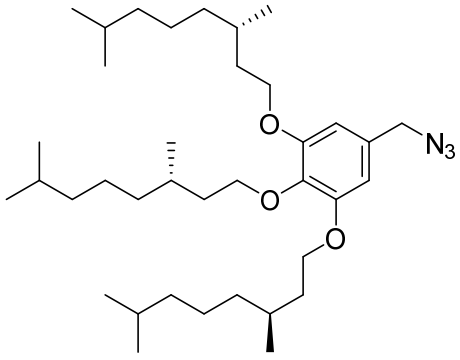

The product was prepared following the same procedure as for **8a** using **12b** (theor 1.39 mmol) and NaN_3 (0.18 g, 2.78 mmol). The product was purified by flash column chromatography using an eluent

gradient from hexanes to hexanes/ethyl acetate 98/2. **13b** was obtained as a colourless liquid with 71 % yield (0.60 g, 0.99 mmol).

FTIR-ATR (neat): 2953, 2925, 2869, 2097, 1590, 1507, 1437, 1236, 1114 cm^{-1}.

^{1}H NMR (400 MHz, $CDCl_3$) δ 6.50 (s, 2H), 4.25 (s, 2H), 4.12 – 3.86 (m, 6H), 1.94 – 1.77 (m, 3H), 1.77 – 1.64 (m, 3H), 1.64 – 1.44 (m, 6H), 1.44 – 1.21 (m, 9H), 1.21 – 1.05 (m, 9H), 0.98 – 0.90 (m, 9H), 0.87 (d, *J* = 6.6 Hz, 18H).

^{13}C NMR (101 MHz, $CDCl_3$) δ 153.34, 138.10, 130.36, 106.54, 71.64, 67.44, 55.19, 39.36, 39.26, 37.52, 37.34, 37.33, 36.37, 29.81, 29.69, 27.98, 24.73, 24.71, 22.70, 22.61, 22.60, 19.58.

ESI-MS analysis: $C_{37}H_{67}N_3O_3Na$ $[M+Na]^+$, mass calculated: 624.51, mass found: 624.51.

Synthesis of 14a

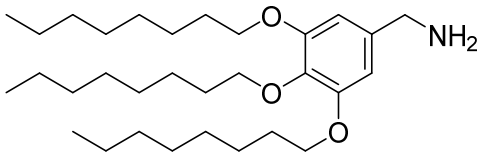

13a (665 mg, 1.28 mmol) was dissolved in anhydrous diethyl ether (10 mL) under N_2 atmosphere. After 10 min stirring at 0-4 °C, $LiAlH_4$ (1 M in THF, 1.54 mL) was added dropwise via syringe. After 2 h stirring at 0-4 °C no starting material was observed by TLC. The mixture was diluted with diethyl ether (20 mL), and water (0.660 mL) and aqueous 1 M NaOH (0.660 mL) were consecutively added at 0-4 ºC. After 1 h water the mixture was filtered and the filter cake was washed with diethyl ether (3 x 5 mL). The filtrate was submitted to reduced pressure and the crude was obtained as a colorless oil. The product was purified by flash column chromatography using an eluent gradient of ethyl acetate/methanol/NH_4OH (aq) from 10/0/0 to 9/1/0 and finally 9/1/0.1. **14a** was obtained as a waxy white solid with a 48 % yield (0.31 g, 0.61 mmol).

FTIR-ATR (neat): 2920, 2850, 1641, 1591, 1502, 1466, 1435, 1330, 1230, 1115 cm^{-1}.

^{1}H NMR (400 MHz, $CDCl_3$) δ 6.54 (s, 2H), 3.96 (t, *J* = 6.5 Hz, 4H), 3.91 (t, *J* = 6.6 Hz, 2H), 3.79 (s, 2H), 3.17 (bs, 2H), 1.85 – 1.65 (m, 6H), 1.54 – 1.39 (m, 6H), 1.39 – 1.13 (m, 24H), 1.04 – 0.53 (m, 9H).

^{13}C NMR (101 MHz, $CDCl_3$) δ 153.25, 137.31, 135.79, 105.84, 73.39, 69.12, 46.04, 31.89, 31.82, 30.32, 29.55, 29.43, 29.37, 29.29, 26.11, 26.11, 22.67, 22.65, 14.07.

ESI-MS analysis: $C_{31}H_{37}NO_3Na$ $[M+Na]^+$, mass calculated: 514.42, mass found: 514.41.

Synthesis of 14b

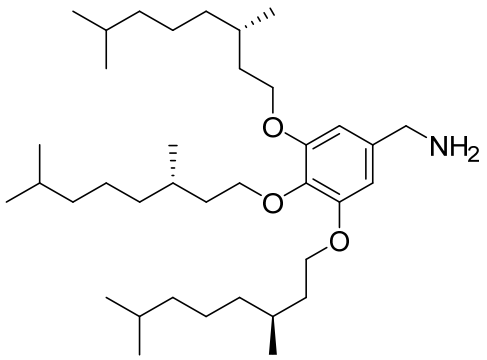

14b was prepared following the same procedure as for **14a** using **13b** (396 mg, 0.66 mmol) and $LiAlH_4$ (1 M in THF, 0.79 mL). **14a** was obtained as a yellow oil with a 61 % yield (229 mg, 0.40 mmol).

FTIR-ATR (neat): 2953, 2925, 2869, 1589, 1463, 1436, 1232, 1114 cm^{-1}.

^1H NMR (400 MHz, $CDCl_3$) δ 6.56 (s, 2H), 4.08 – 3.86 (m, 6H), 3.83 (s, 2H), 3.21 (bs, 3H), 1.94 – 1.76 (m, 3H), 1.76 – 1.62 (m, 3H), 1.62 – 1.43 (m, 6H), 1.43 – 1.20 (m, 10H), 1.20 – 1.03 (m, 8H), 0.93 (d, *J* = 6.4 Hz, 6H), 0.91 (d, *J* = 6.2 Hz, 3H), 0.86 (d, *J* = 6.6 Hz, 18H).

^{13}C NMR (101 MHz, $CDCl_3$) δ 153.32, 137.42, 135.06, 105.89, 71.64, 67.40, 45.92, 39.36, 39.27, 37.54, 37.39, 37.34, 36.45, 29.81, 29.71, 27.97, 24.73, 24.70, 22.70, 22.61, 22.59, 19.56, 19.55.

ESI-MS analysis: $C_{37}H_{67}O_3$ $[M\text{-}NH_2]^+$, mass calculated: 559.51, mass found: 559.50.

Synthesis of 15a

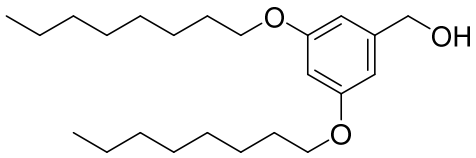

3,5-dihydroxybenzyl alcohol (2.01 g, 14.4 mmol), *n*-octyl bromide (5.33 mL, 30.9 mmol), 18-crown-6 (741 mg, 2.80 mmol) and K_2CO_3 (7.87 g, 56.9 mmol) were suspended in dry acetone (50 mL) under an argon atmosphere. The mixture was refluxed for 16 hours, after which the mixture was cooled to room temperature and subsequently, water (50 mL) was added and the volatile organic solvent was evaporated. Then, DCM (50 mL) was added and the product was extracted into the organic layer. The organic layer was dried over $MgSO_4$, filtered and evaporated. Column chromatography (KP-Sil 100g, heptane to EtOAc) afforded the product (4.65 g, 89%).

^1H NMR (400 MHz, $CDCl_3$) δ 6.50 (d, *J* = 2.2 Hz, 2H), 6.38 (t, *J* = 2.2 Hz, 1H), 4.62 (d, *J* = 5.9 Hz, 2H), 3.93 (t, *J* = 6.6 Hz, 4H), 1.81-1.73 (m, 4H), 1.46-1.40 (m, 4H), 1.37-1.25 (m, 16H), 0.89 (t, *J* = 7.1 Hz, 6H).

^{13}C NMR (101 MHz, $CDCl_3$) δ 160.70, 143.32, 105.21, 100.71, 68.22, 65.65, 31.97, 29.50, 29.41, 29.39, 26.20, 22.81, 14.25.

MALDI-ToF analysis: mass calculated: 364.30, mass found: 365.38 $(M+H^+)$.

Synthesis of 15b

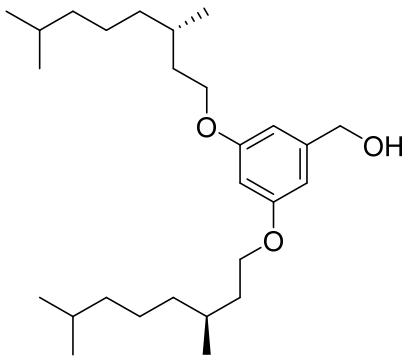

3,5-dihydroxybenzyl alcohol (1.66 g, 11.9 mmol), citronellyl tosylate (7.97 g, 25.5 mmol), 18-crown-6 (632 mg, 2.39 mmol) and K_2CO_3 (6.52 g, 47.2 mmol) were suspended in dry acetone (25 mL) under an argon atmosphere. The mixture was refluxed for 15 hours, after which it was cooled to room temperature and subsequently, the solvent was evaporated. Then, the product was redissolved in DCM (50 mL) and washed with water (50 mL). The aqueous layer was extracted with DCM and the combined organic layers were dried over $MgSO_4$, filtered and evaporated. Column chromatography (KP-Sil 50, 7 vol% EtOAc in heptane) afforded the product (3.43 g, 69%).

^{1}H NMR (400 MHz, $CDCl_3$) δ 6.47 (d, *J* = 2.2 Hz, 2H), 6.35 (t, *J* = 2.2 Hz, 2H), 4.56 (d, *J* = 5.5 Hz, 2H), 3.93 (m, 4H), 1.84-1.73 (m, 2H), 1.72-1.61 (m, 2H), 1.59-1.47 (m, 4H), 1.37-1.23 (m, 6H), 1.19-1.12 (m, 6H), 0.93 (d, *J* = 6.6 Hz, 6H), 0.87 (d, *J* = 6.7 Hz, 12H).

^{13}C NMR (101 MHz, $CDCl_3$) δ 160.50, 143.35, 105.08, 100.56, 66.40, 65.24, 39.33, 37.37, 36.29, 29.93, 28.0, 24.74, 22.79, 22.69, 19.71.

MALDI-ToF analysis: mass calculated: 420.36, mass found: 421.37 ($M+H^+$).

Synthesis of 16a

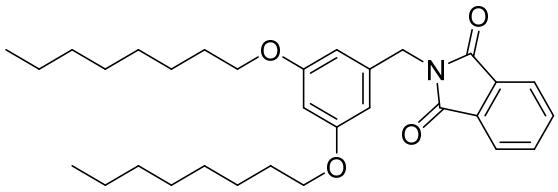

15a (4.44 g, 12.2 mmol), phthalimide (2.24 g, 15.2 mmol) and PPh_3 (2.96 g, 14.6 mmol) were dissolved in dry THF (100 mL) under an argon atmosphere. The solution was cooled to 0 °C using an ice bath and a solution of DIAD (2.87 mL, 14.6 mmol) in dry THF (40 mL) was added using a dropping funnel. Then, the mixture was left to heat up and stir for 3 hours, after which the solvent was evaporated. Pentane (75 mL) was added to the residue to result in the formation of a white precipitate. The supernatant was decanted and evaporated. Column chromatography (KP-Sil 100g, 25% EtOAc in heptane) afforded the product in quantitative yield.

^{1}H NMR (400 MHz, $CDCl_3$) δ 7.82-7.87 (m, 2H), 7.68-7.73 (m, 2H), 6.55 (d, *J* = 2.2 Hz, 2H), 3.90 (t, *J* = 6.6 Hz, 4H), 1.77-1.68 (m, 4H), 1.45-1.37 (m, 4H), 1.34-1.22 (m, 16H), 0.88 (t, *J* = 7.0 Hz, 6H).

^{13}C NMR (101 MHz, $CDCl_3$) δ 168.14, 160.61, 138.46, 134.09, 132.30, 123.48, 106.98, 100.77, 68.18, 41.83, 31.95, 29.49, 29.38, 29.36, 26.18, 22.83, 22.80, 14.25, 14.24.

MALDI-ToF analysis: mass calculated: 493.32, mass found: 494.45 ($M+H^+$).

Synthesis of 16b

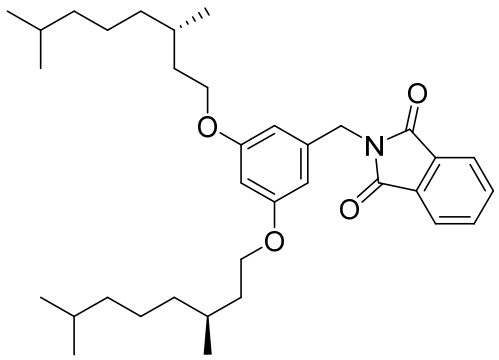

15b (3.43 g, 8.16 mmol) was dissolved in dry THF (100 mL) under an argon atmosphere. Phthalimide (1.51 gram, 10.2 mmol) and PPh_3 (2.78 g, 10.6 mmol) were added and the mixture was cooled to 0 °C using an icebath. Using a dropping funnel, a solution of DIAD (1.93 mL, 9.79 mmol) in dry THF (40 mL) was added, resulting in a yellow solution. The mixture was left to heat up to room temperature and stirred for 4 hours, after which the solvent was evaporated. Then, pentane (100 mL) was added to the yellow oil to precipitate a White solid. The resulting precipitate was filtered off and the filtrate was evaporated. Column chromatography (KP-Sil 100g, 25% $CHCl_3$ in heptane) afforded the product as a viscous oil (3.57 g, 80%).

^1H NMR (400 MHz, $CDCl_3$) δ 7.84 (m, 2H), 7.72 (m, 2H), 6.55 (d, *J* = 2.2 Hz, 2H), 6.34 (t, *J* = 2.2 Hz, 1H), 4.76 (s, 2H), 3.93 (m, 4H), 1.84-1.72 (m, 2H), 1.68-1.58 (m, 2H), 1.54-1.46 (m, 2H), 1.35-1.22 (m, 8H), 1.18-1.10 (m, 6H), 0.91 (d, *J* = 6.6 Hz, 6H), 0.87 (s, 12H).

^{13}C NMR (100 MHz, $CDCl_3$) δ 168.16, 160.61, 138.47, 134.11, 132.32, 123.50, 106.98, 100.77, 66.48, 41.84, 39.39, 37.44, 36.34, 32.04, 29.94, 28.12, 24.79, 22.86, 22.84, 22.75, 19.78, 14.27.

MALDI-ToF analysis: mass calculated: 549.38, mass found: 550.42 ($M+H^+$).

Synthesis of 17a

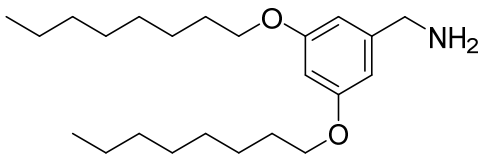

16a (5.61 g, 11.4 mmol) was dissolved in 1:1 EtOH:THF (40 mL). Then, hydrazine monohydrate (5.52 mL, 0.11 mol) was added and the mixture was refluxed overnight. After coooling down to room temperature, DCM (50 mL) was added and the solution was washed with 1M aqueous Na_2CO_3 solution (100 mL). The organic layer was dried over $MgSO_4$, filtered and evaporated to yield the product as a light red oil (3.85 g, 93%).

^{1}H NMR (400 MHz, $CDCl_3$) δ 6.44 (d, J = 2.2 Hz, 2H), 6.34 (t, J = 2.2 Hz, 1H), 3.93 (t, J = 6.6Hz, 4H), 3.79 (s, 2H), 1.80-1.72 (m, 4H), 1.46-1.38 (m, 4H), 1.37-1.22 (m, 16H), 0.89 (t, J = 7.0 Hz, 6H).

^{13}C NMR (100 MHz, $CDCl_3$) δ 160.67, 145.88, 105.48, 99.76, 68.17, 46.86, 31.96, 29.50, 29.43, 29.39, 26.20, 22.80, 14.24.

ESI-MS analysis: mass calculated: 363.31, mass found: 364.17 ($M+H^+$).

Synthesis of 17b

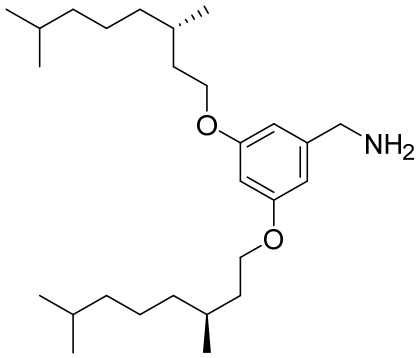

16b (3.5 g, 6.37 mmol) was dissolved in 1:1 EtOH:THF (20 mL). Then, hydrazine monohydrate (4.83 mL, 63.7 mmol) was added. The mixture was then refluxed overnight and left at room temperature for 1 day, after which a white precipitate was formed. The suspension was dispersed between $CHCl_3$ (50 mL) and 0.5 M aqueous Na_2CO_3 solution (100 mL). The aqueous layer was extracted with $CHCl_3$ (3x25 mL) and the combined organic layers were dried over $MgSO_4$, filtered and evaporated to yield the product as a clear oil in quantitative yield.

^{1}H NMR (400 MHz, $CDCl_3$) δ 6.45 (d, J = 2.2 Hz, 2H), 6.34 (t, J = 2.2 Hz, 2H), 3.96 (m, 4H), 3.79 (s, 2H), 1.86-1.77 (m, 2H), 1.71-1.64 (m, 2H), 1.62-1.53 (m, 4H), 1.37-1.23 (m, 6H), 1.18-1.12 (m, 6H), 0.93 (d, J = 6.6 Hz, 6H), 0.87 (d, J = 6.7 Hz, 12H).

^{13}C NMR (100 MHz, $CDCl_3$) δ 160.67, 145.91, 105.48, 99.79, 66.48, 46.89, 39.41, 37.44, 36.40, 30.01, 28.13, 24.8, 22.86, 22.76, 19.81.

IR spectra of BTA derivatives

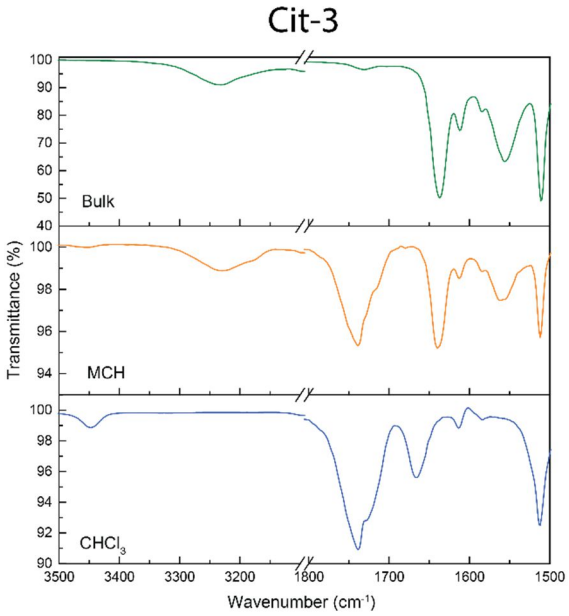

Figure S8. IR spectra of **Cit-3** in the bulk (top panel) and 250 μM solutions in MCH (middle panel) and $CHCl_3$ (bottom panel).

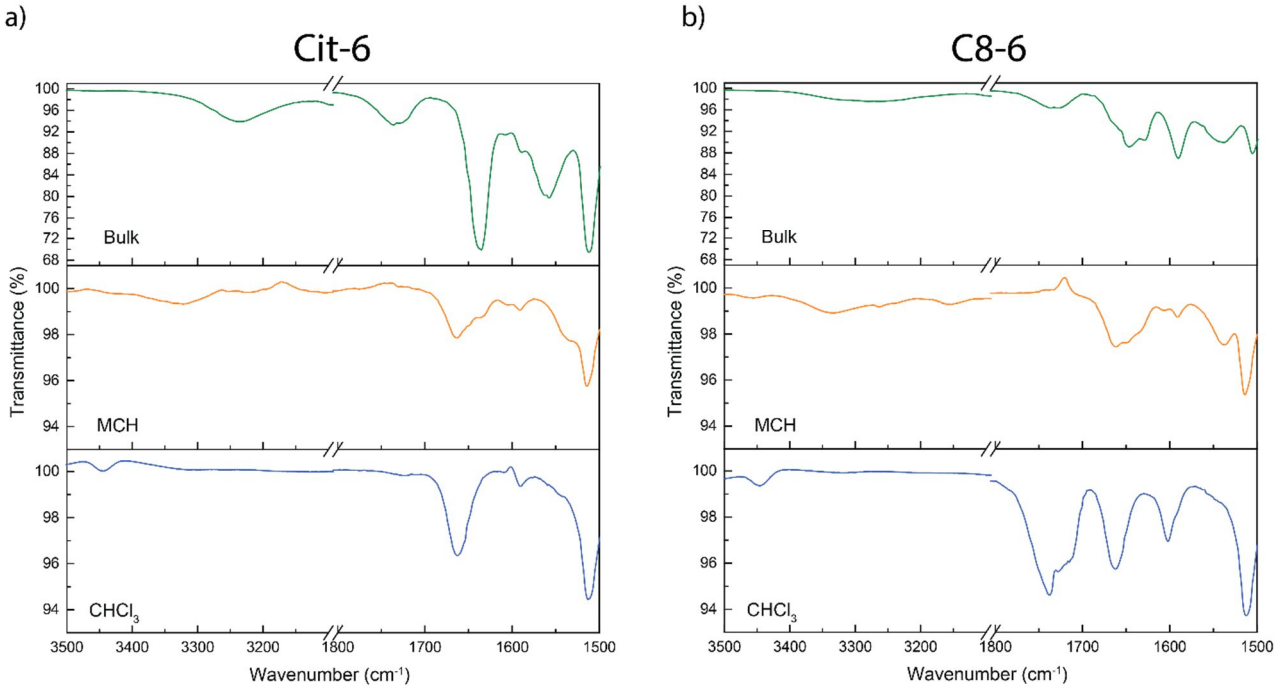

Figure S9. IR spectra of **Cit-6** (a) and **C8-6** (b) in the bulk (top panel) and 250 μM solutions in MCH (middle panel) and $CHCl_3$ (bottom panel).

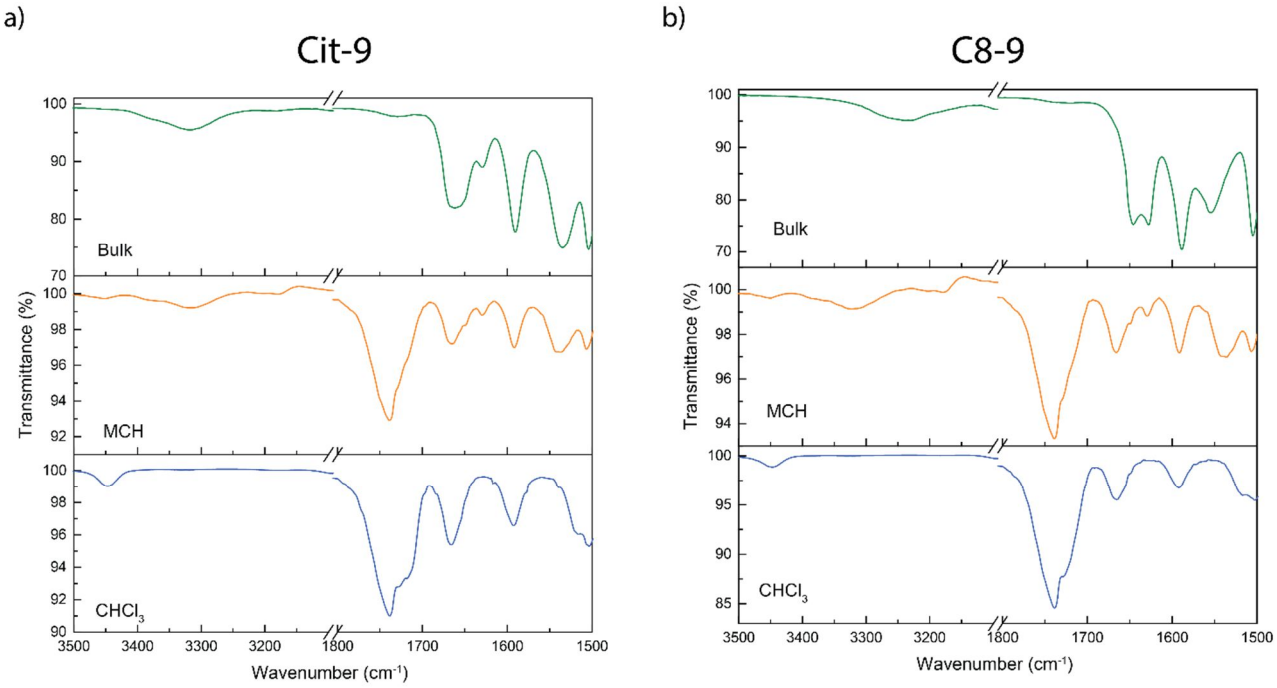

Figure S10. IR spectra of **Cit-9** (a) and **C8-9** (b) in the bulk (top panel) and 250 μM solutions in MCH (middle panel) and $CHCl_3$ (bottom panel).

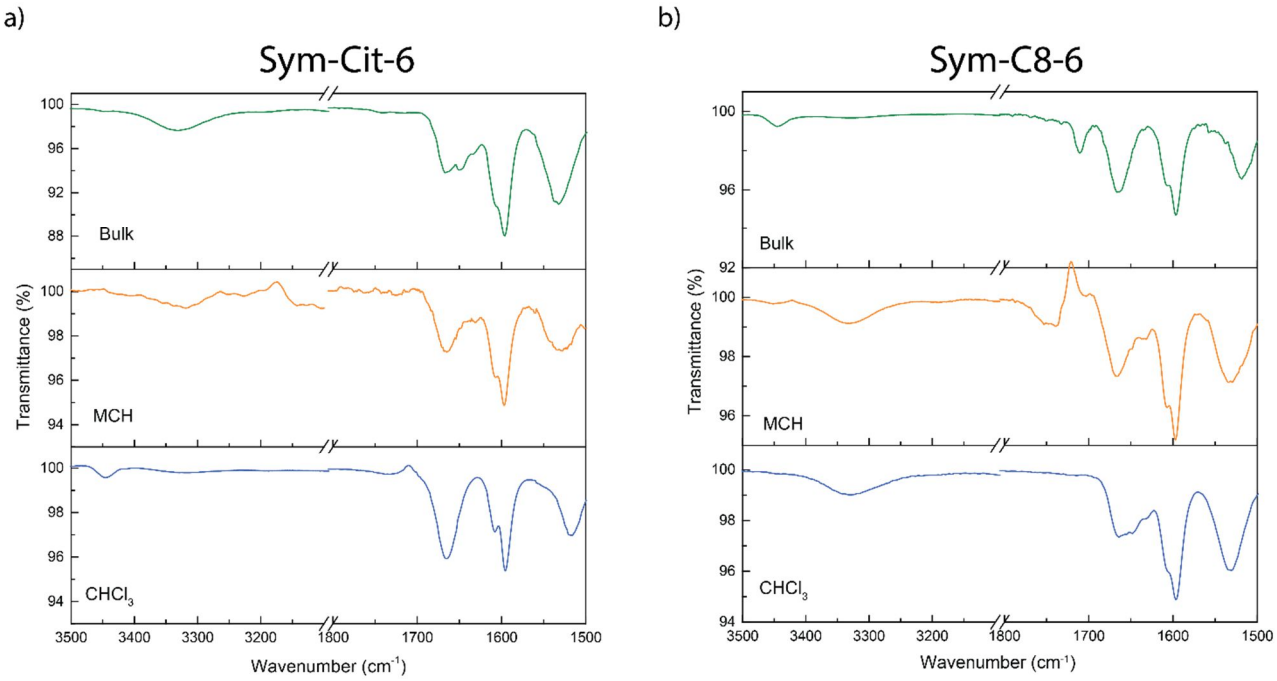

Figure S11. IR spectra of **Sym-Cit-6** (a) and **Sym-C8-6** (b) in the bulk (top panel) and 250 μM solutions in MCH (middle panel) and $CHCl_3$ (bottom panel).

VT-UV and VT-CD spectra of BTA derivatives

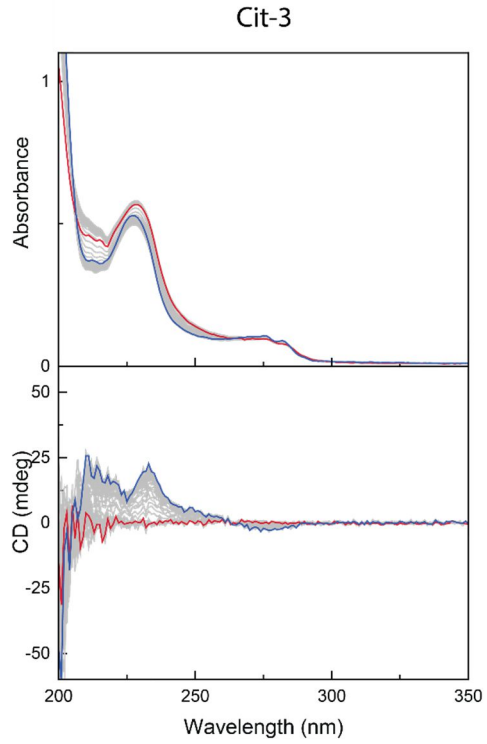

Figure S12. VT-UV (top panel) and VT-CD (bottom panel) spectra of 50 μM solutions of **Cit-3** in MCH. The spectra are measured at regular intervals between 90 °C (red spectrum) and 6 °C (blue spectrum).

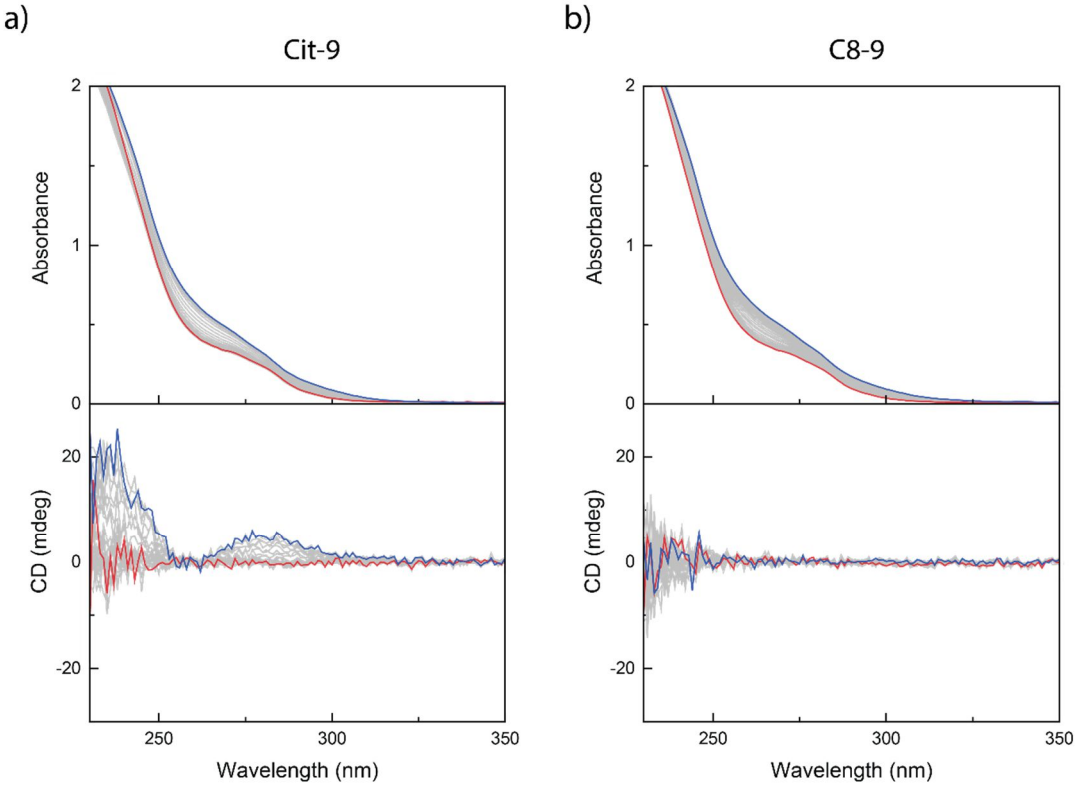

Figure S13. VT-UV (top panel) and VT-CD (bottom panel) spectra of 50 μM solutions of **Cit-9** (a) and **C8-9** (b) in MCH. The spectra are measured at regular intervals between 90 °C (red spectrum) and 6 °C (blue spectrum).

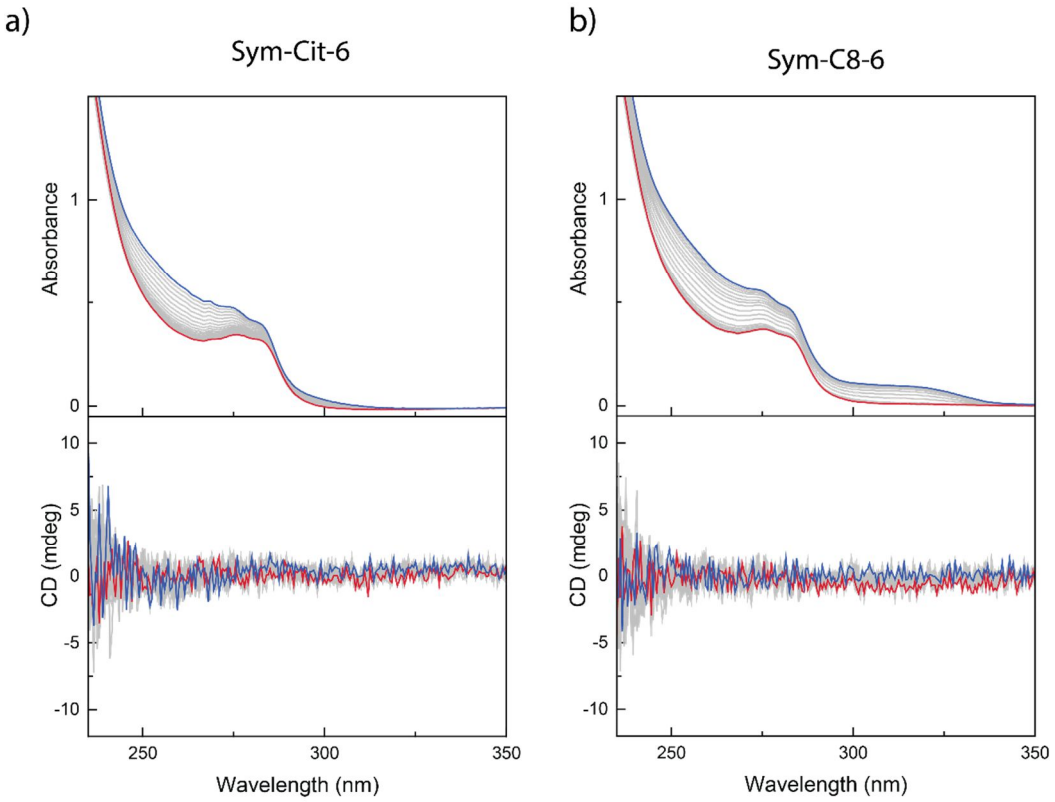

Figure S14. VT-UV (top panel) and VT-CD (bottom panel) spectra of 50 μM solutions of **Sym-Cit-6** (a) and **Sym-C8-6** (b) in MCH. The spectra are measured at regular intervals between 89 °C (red spectrum) and 5 °C (blue spectrum) for **Sym-Cit-6** and 92 °C and 4 °C for **Sym-C8-6** .

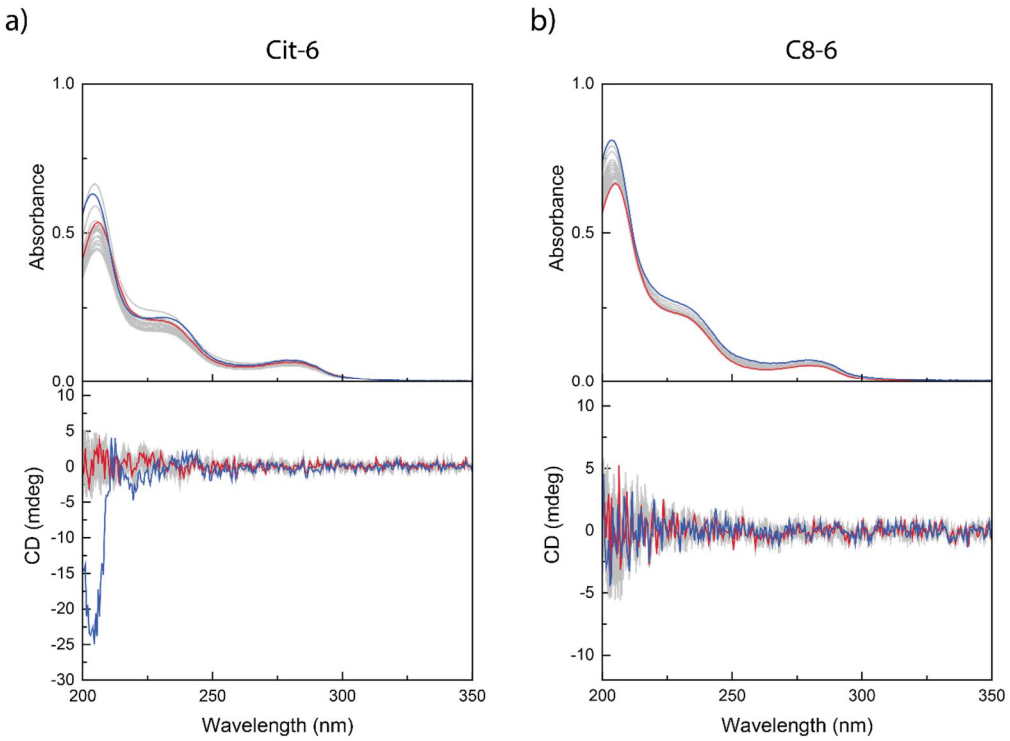

Figure S15. VT-UV (top panel) and VT-CD (bottom panel) spectra of 50 μM solutions of **Cit-6** (a) and **C8-6** (b) in MCH. The spectra are measured at regular intervals between 89 °C (red spectrum) and 5 °C (blue spectrum).

Additional VT-UV and VT-CD cooling curves

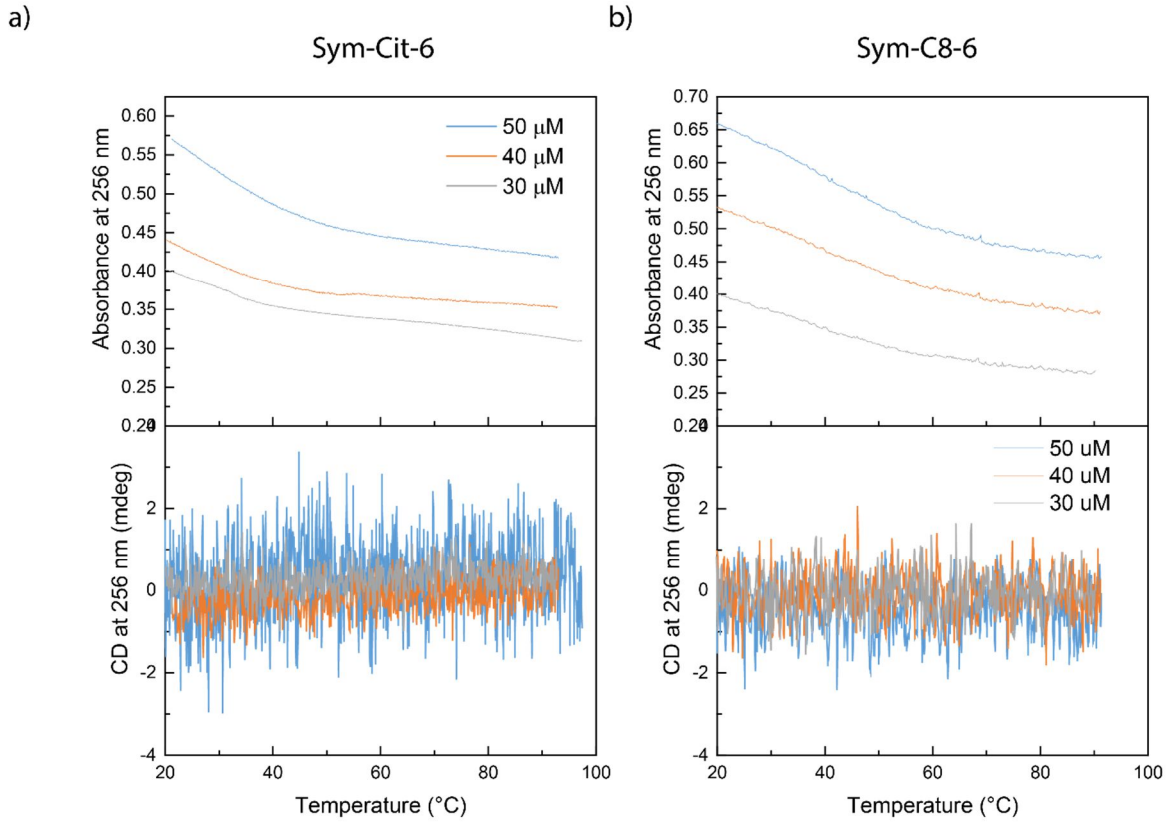

Figure S16. VT-UV (top panels) and VT-CD (bottom panels) cooling curves of **Sym-Cit-6** and **Sym-C8-6** in MCH.

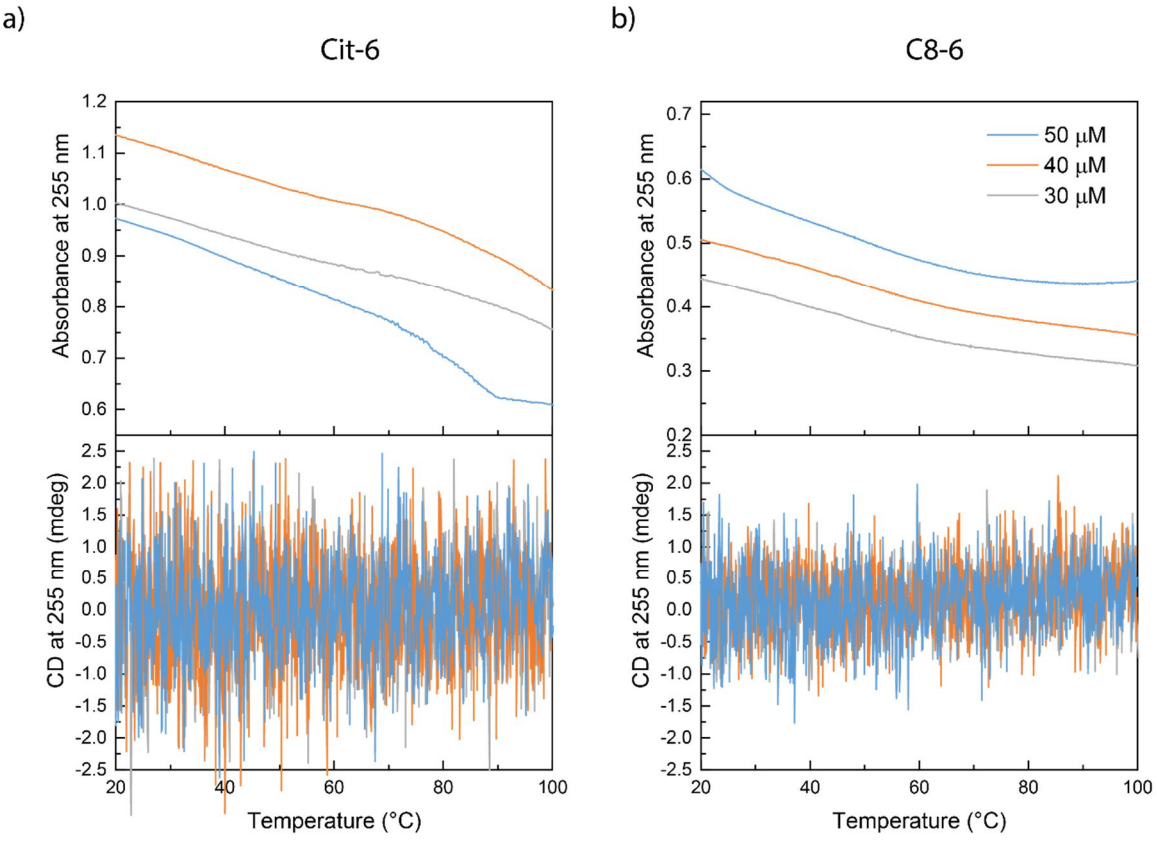

Figure S17. VT-UV (top panels) and VT-CD (bottom panels) cooling curves of **Cit-6** and **C8-6** in MCH.

Fits of cooling curves Cit-3, Cit-9 and C8-9

The fits were obtained by fitting the experimental data with the Matlab software published by ten Eikelder and co-workers.[17]

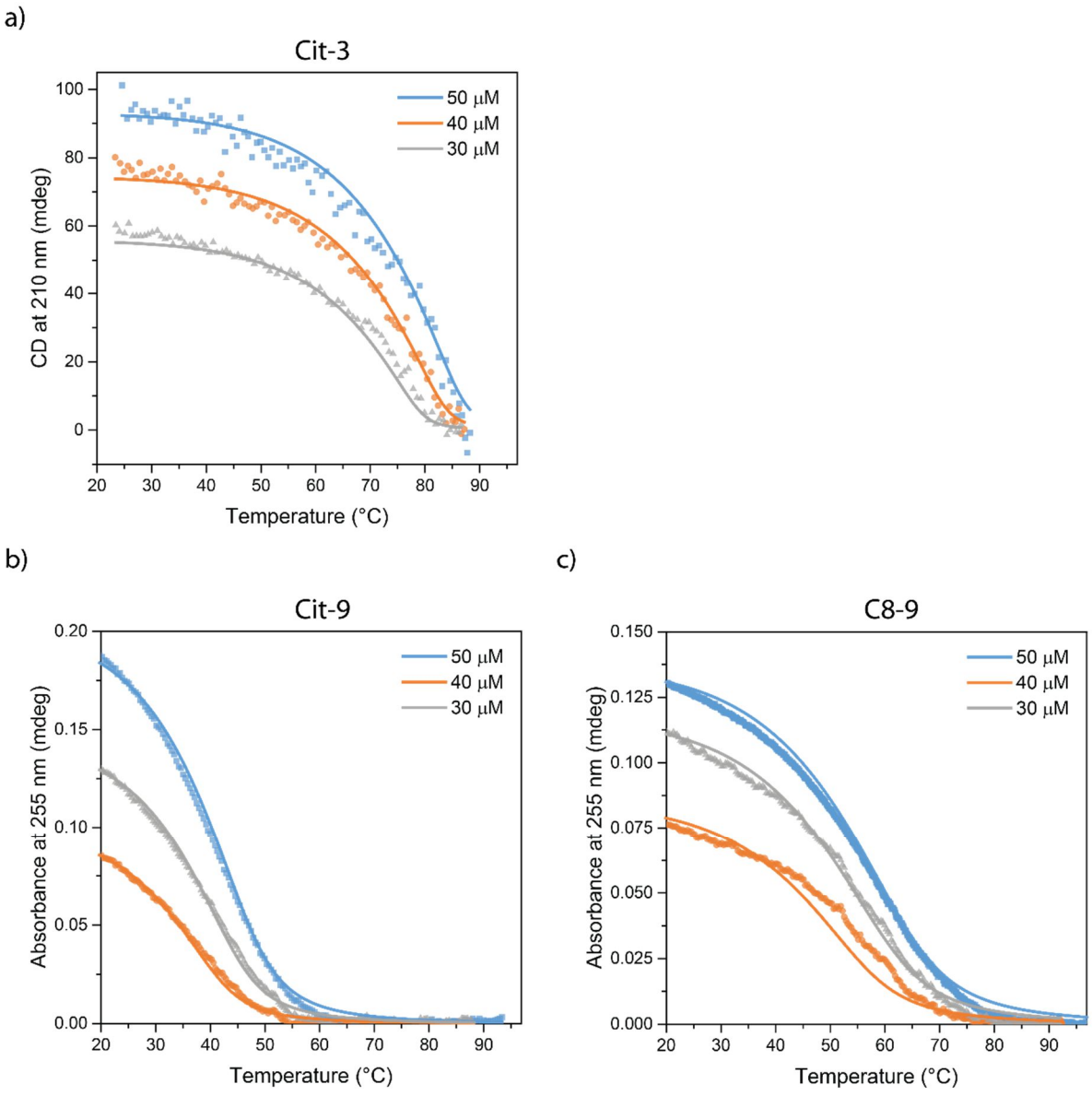

Figure S18. Experimental data (symbols) and fits (solid lines) of the VT-CD experiments of Cit-3 (a), Cit-9 (b) and C8-9 (c). The thermodynamic data obtained is repoted in the main text.

MALDI-TOF mass spectra of the BTA derivatives

C8-3

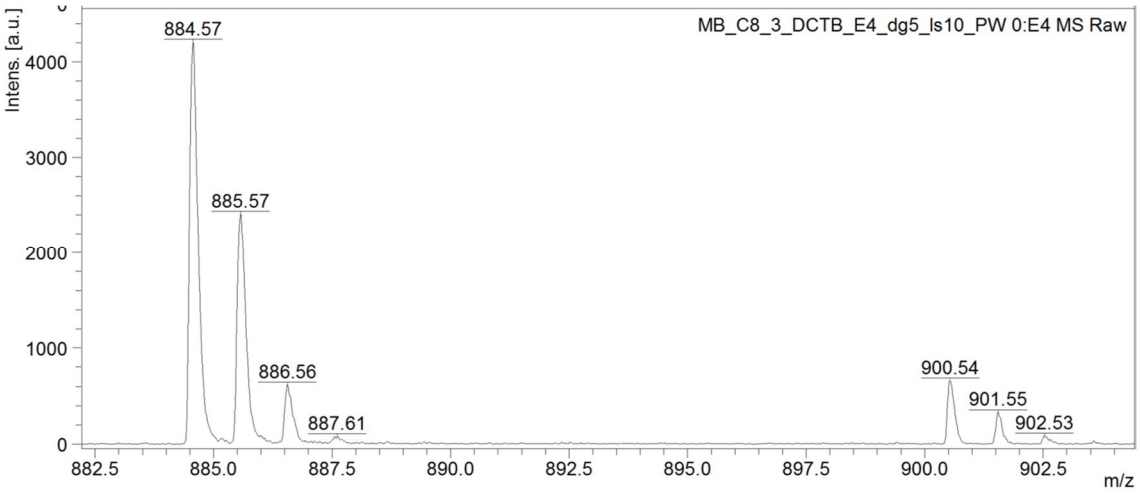

Cit-3

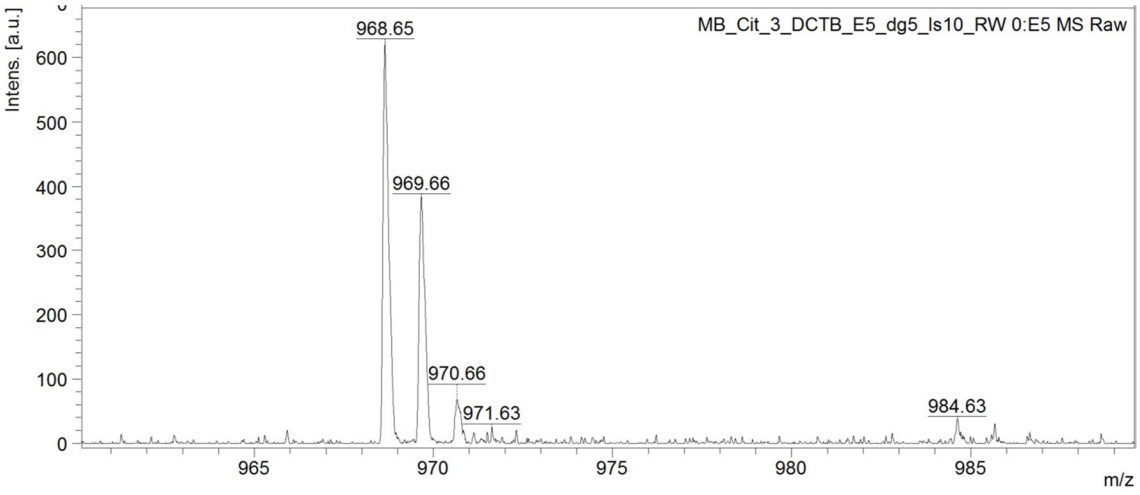

C8-6

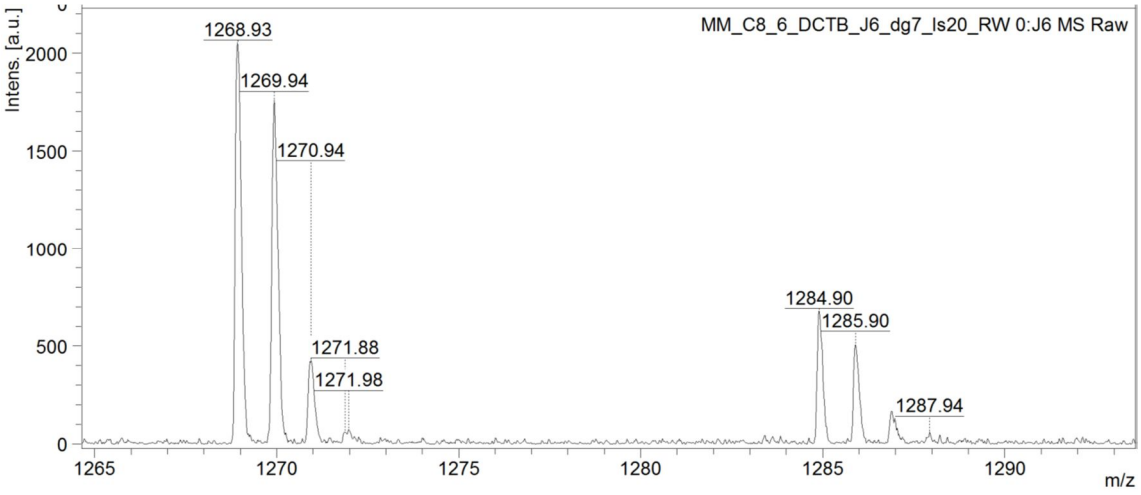

Cit-6

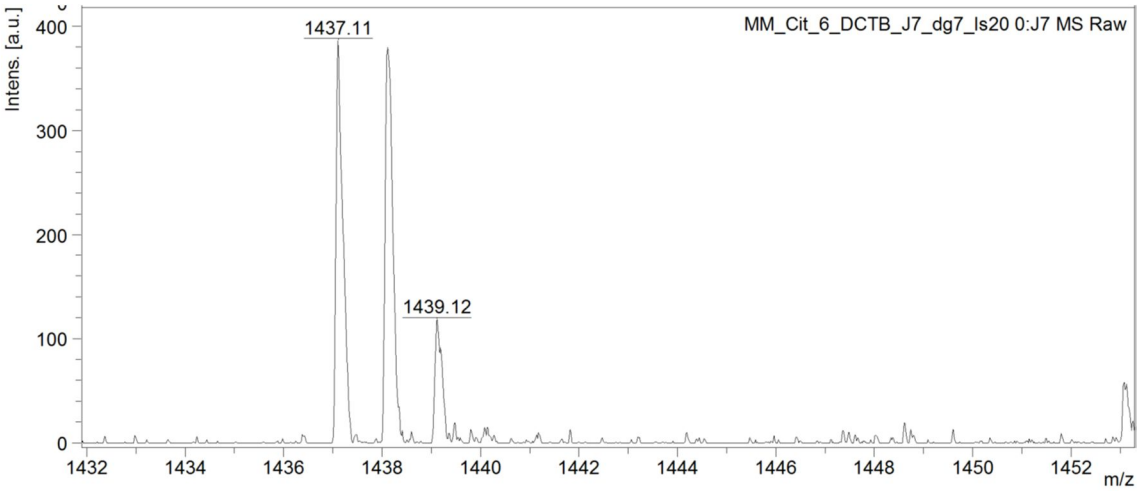

C8-9

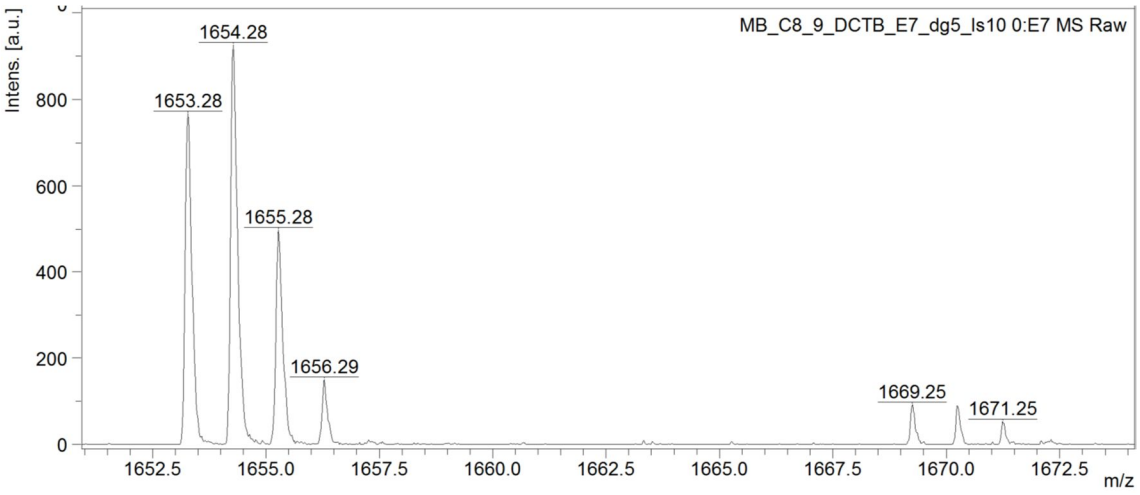

Cit-9

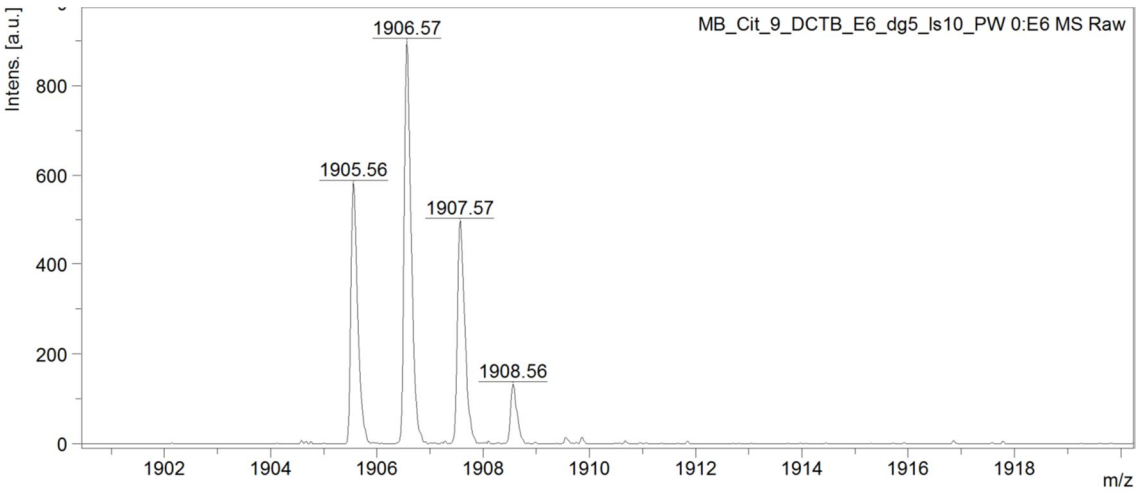

Sym-C8-6

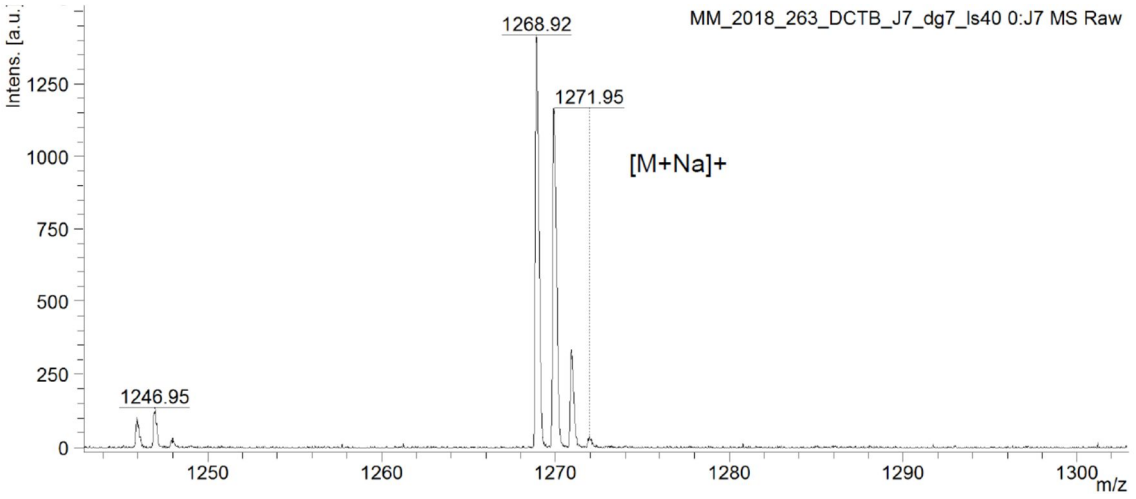

Sym-Cit-6

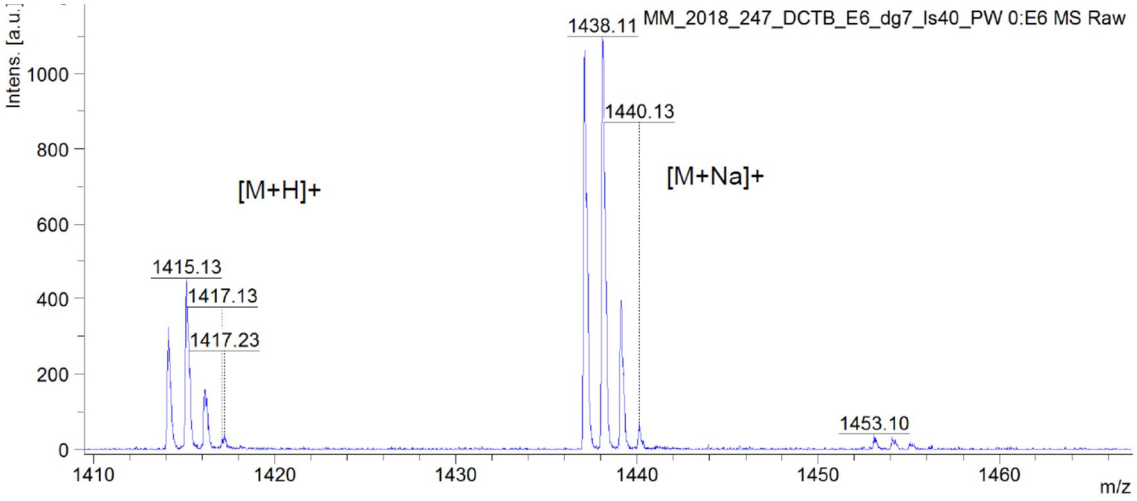

NMR spectra of the BTA derivatives

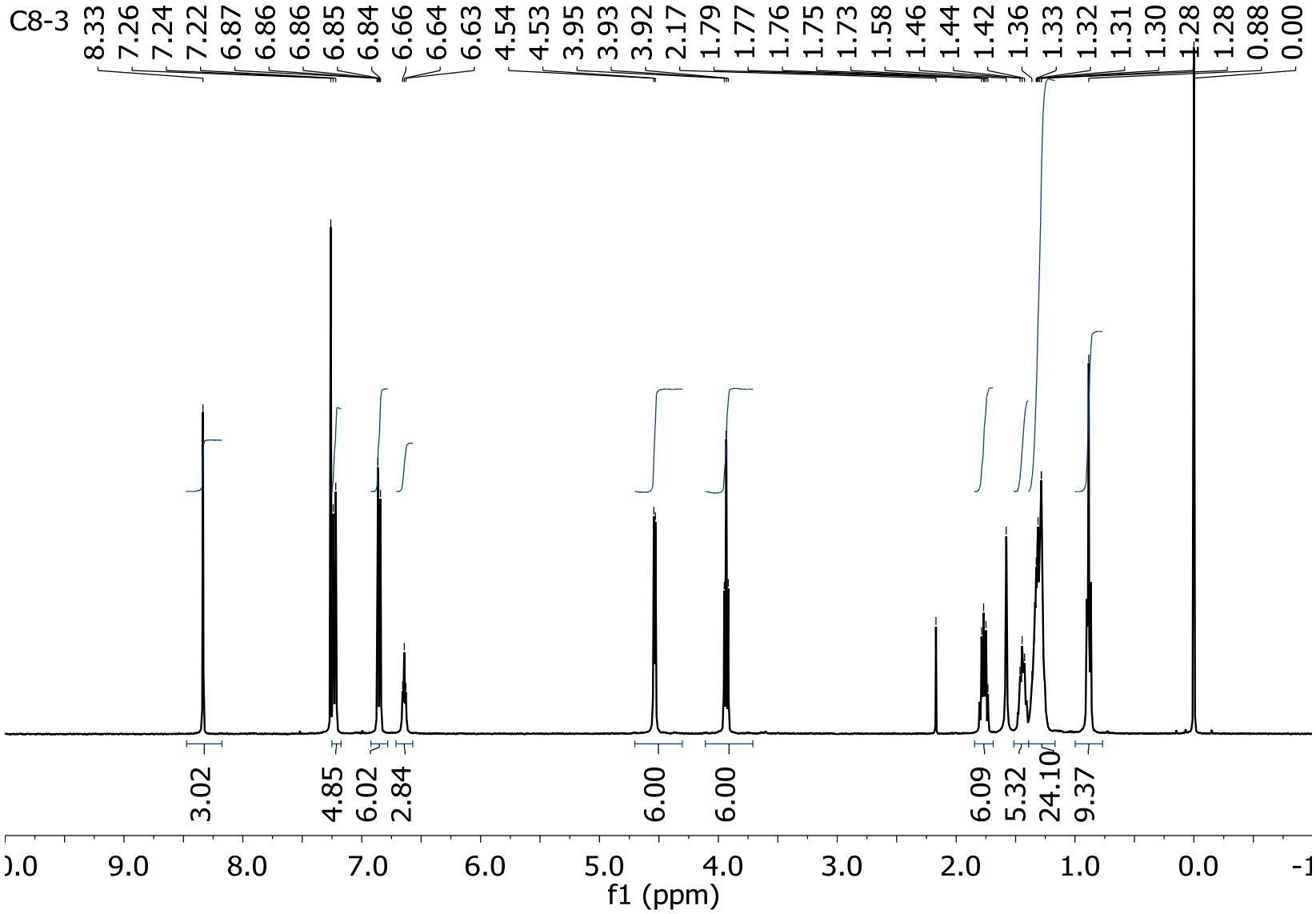

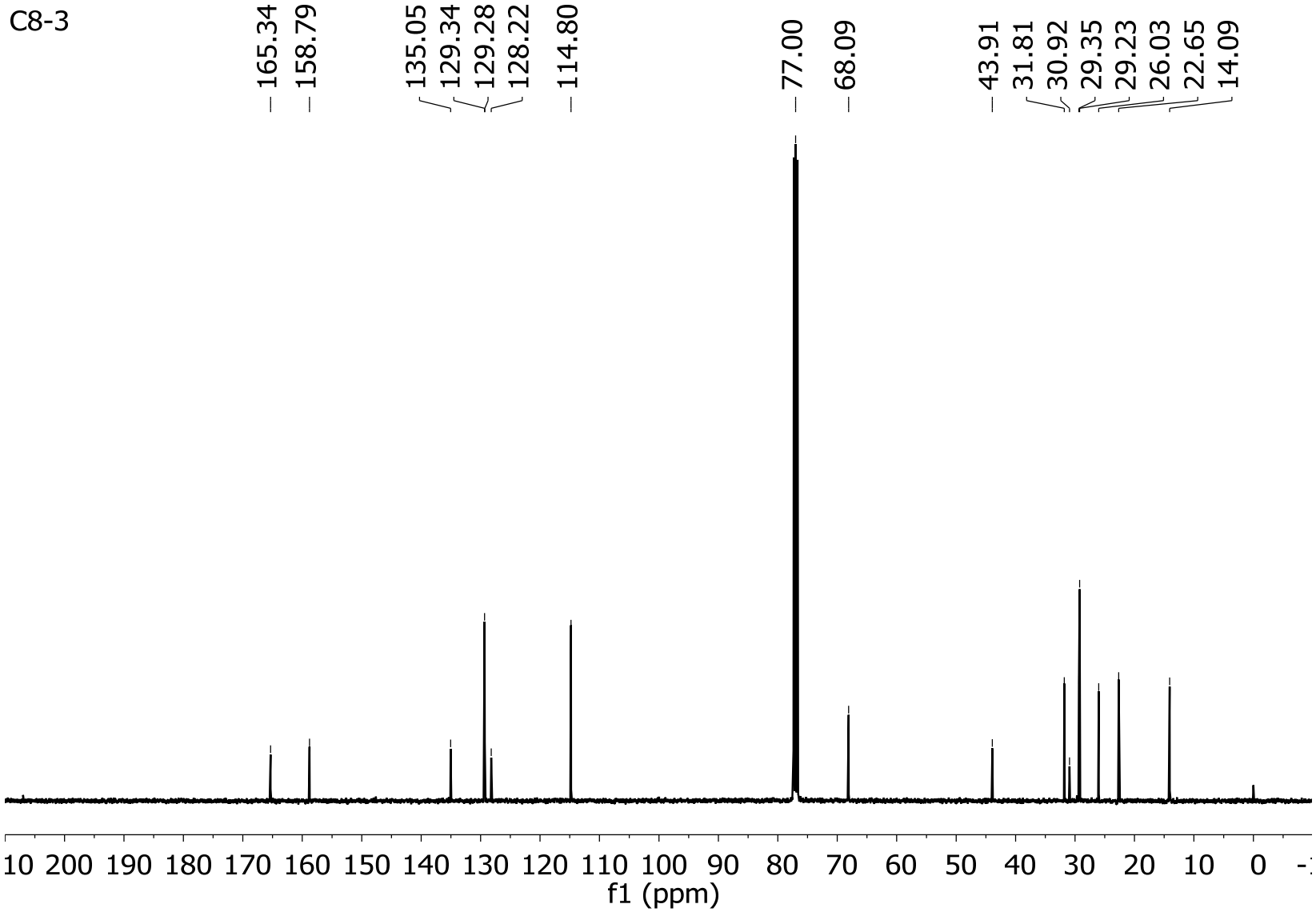
C8-3
165.34
158.79
135.05
129.34
129.28
128.22
114.80
77.00
68.09
43.91
31.81
30.92
29.35
29.23
26.03
22.65
14.09
10 200 190 180 170 160 150 140 130 120 110 100 90 80 70 60 50 40 30 20 10 0
f1 (ppm)

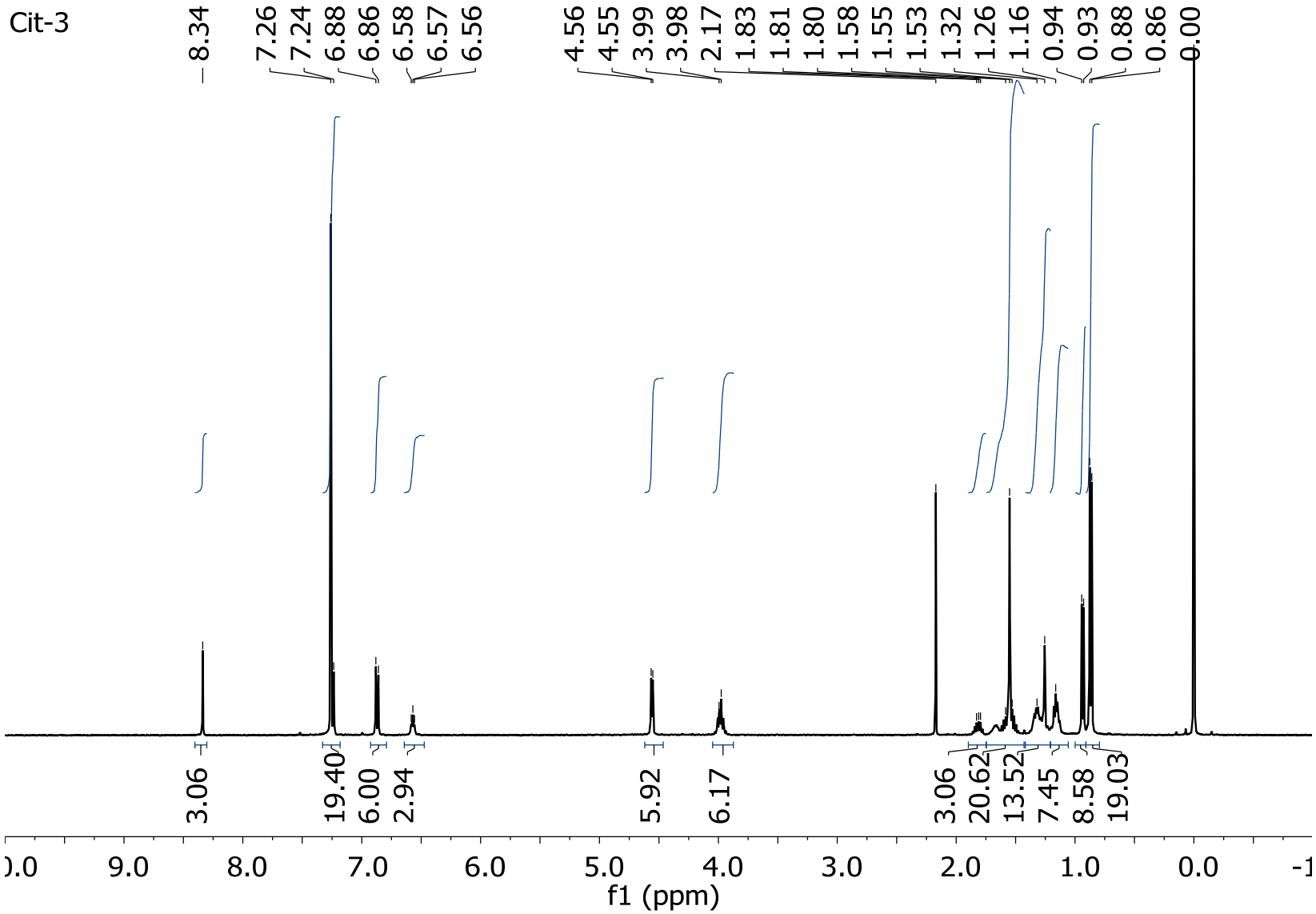
Cit-3
8.34
7.26
7.24
6.88
6.86
6.58
6.57
6.56
4.56
4.55
3.99
3.98
2.17
1.83
1.81
1.80
1.58
1.55
1.53
1.32
1.26
1.16
0.94
0.93
0.88
0.86
0.00
3.06
19.40
6.00
2.94
5.92
6.17
3.06
20.62
13.52
7.45
8.58
19.03
9.0
8.0
7.0
6.0
5.0
4.0
3.0
2.0
1.0
0.0
f1 (ppm)

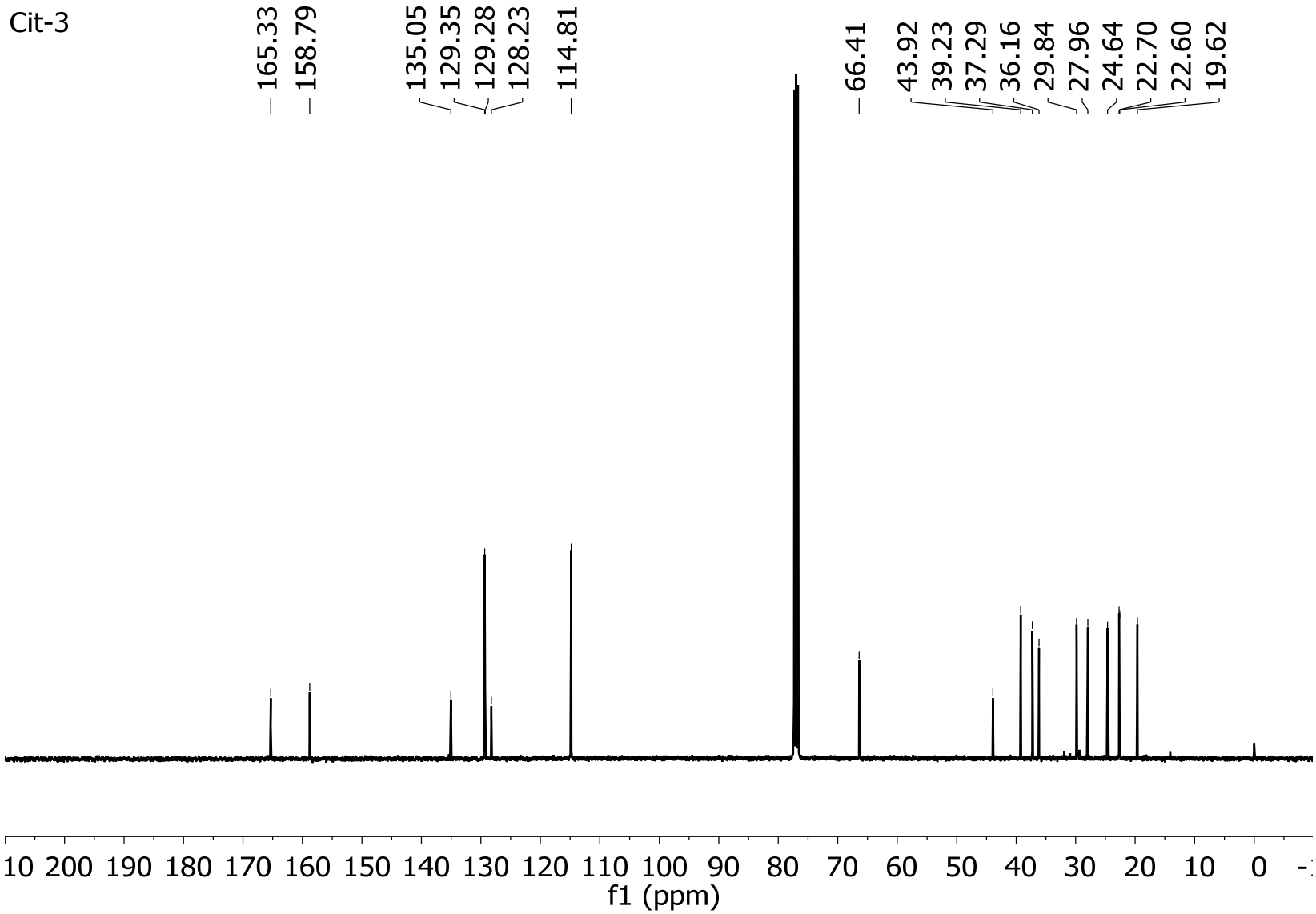
Cit-3
165.33
158.79
135.05
129.35
129.28
128.23
114.81
66.41
43.92
39.23
37.29
36.16
29.84
27.96
24.64
22.70
22.60
19.62
10 200 190 180 170 160 150 140 130 120 110 100 90 80 70 60 50 40 30 20 10 0
f1 (ppm)

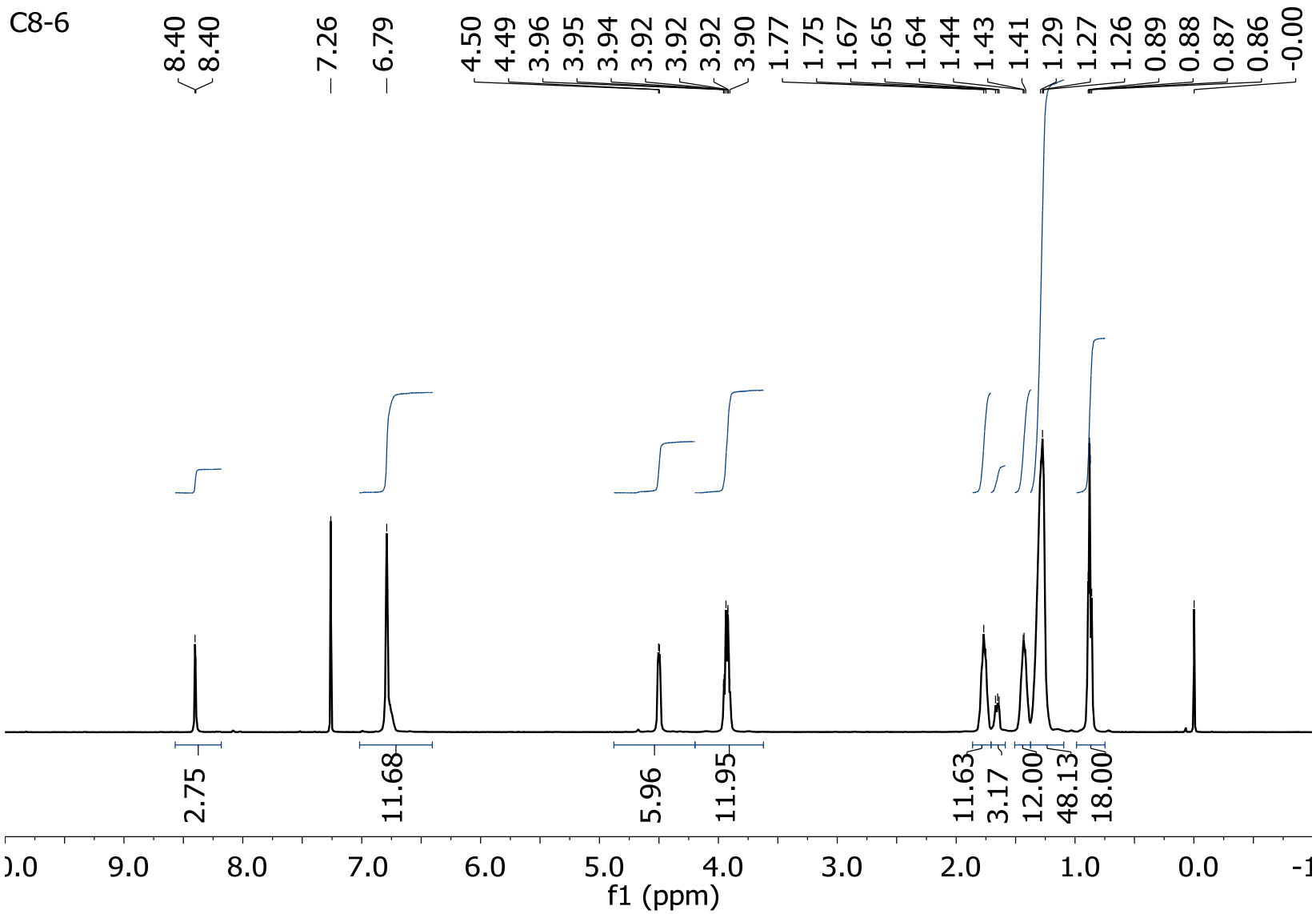
C8-6
8.40
8.40
7.26
6.79
4.50
4.49
3.96
3.95
3.94
3.92
3.92
3.92
3.90
1.77
1.75
1.67
1.65
1.64
1.44
1.43
1.41
1.29
1.27
1.26
0.89
0.88
0.87
0.86
-0.00
2.75
11.68
5.96
11.95
11.63
3.17
12.00
48.13
18.00
9.0
8.0
7.0
6.0
5.0
4.0
3.0
2.0
1.0
0.0
f1 (ppm)

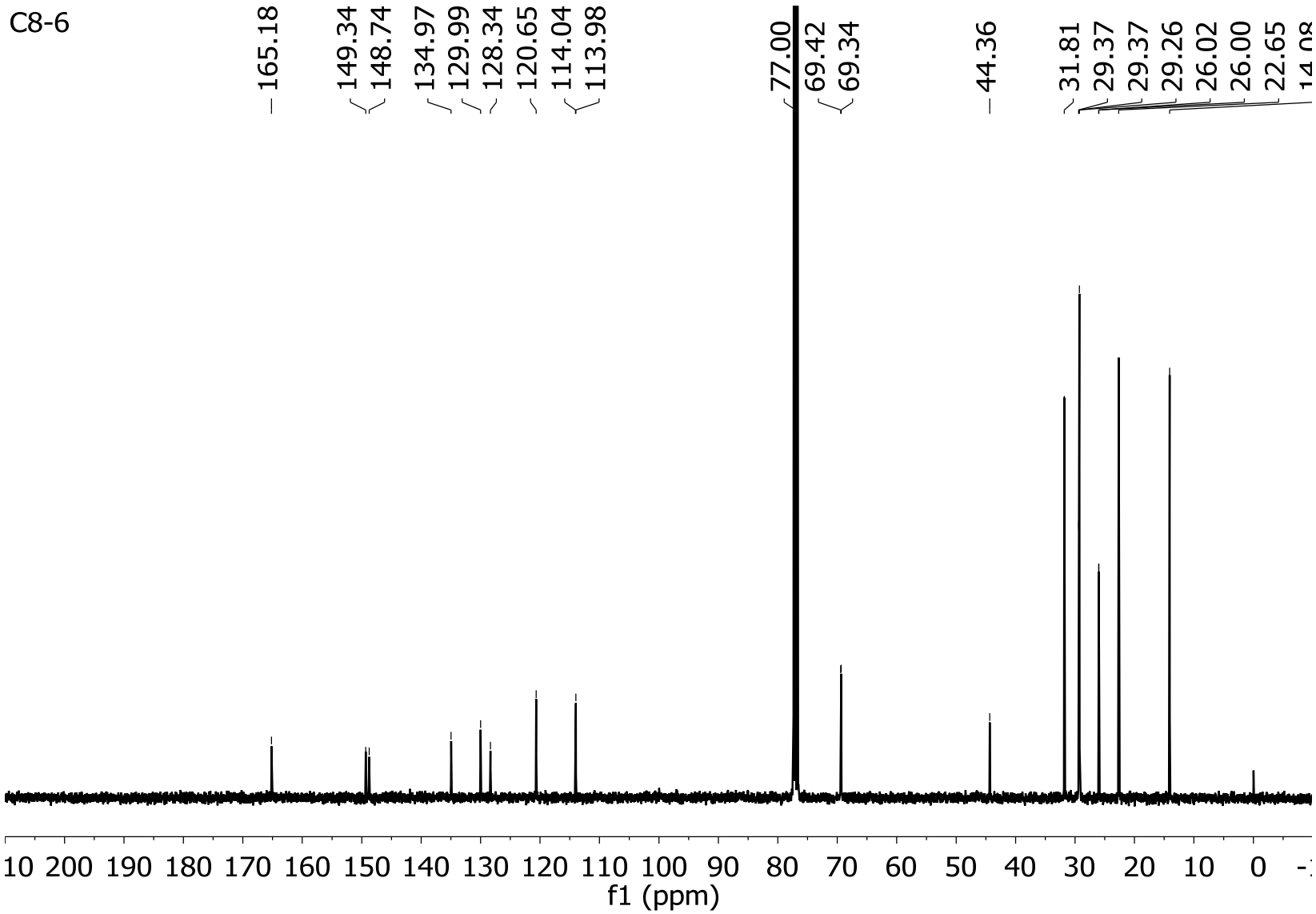
C8-6
165.18
149.34
148.74
134.97
129.99
128.34
120.65
114.04
113.98
77.00
69.42
69.34
44.36
31.81
29.37
29.37
29.26
26.02
26.00
22.65
f1 (ppm)

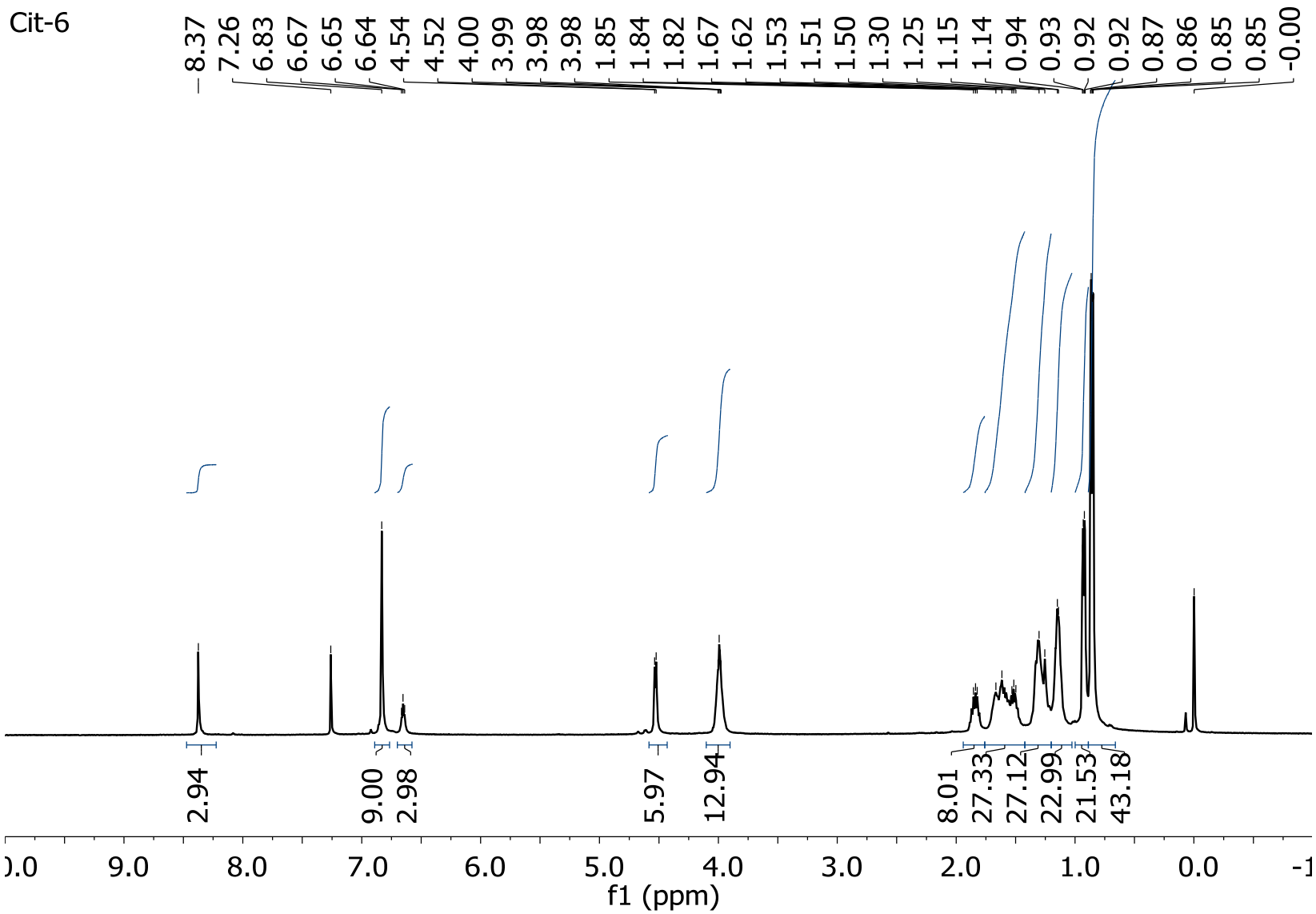
Cit-6
8.37
7.26
6.83
6.67
6.65
6.64
4.54
4.52
4.00
3.99
3.98
3.98
1.85
1.84
1.82
1.67
1.62
1.53
1.51
1.50
1.30
1.25
1.15
1.14
0.94
0.93
0.92
0.92
0.87
0.86
0.85
0.85
-0.00
2.94
9.00
2.98
5.97
12.94
8.01
27.33
27.12
22.99
21.53
43.18
f1 (ppm)

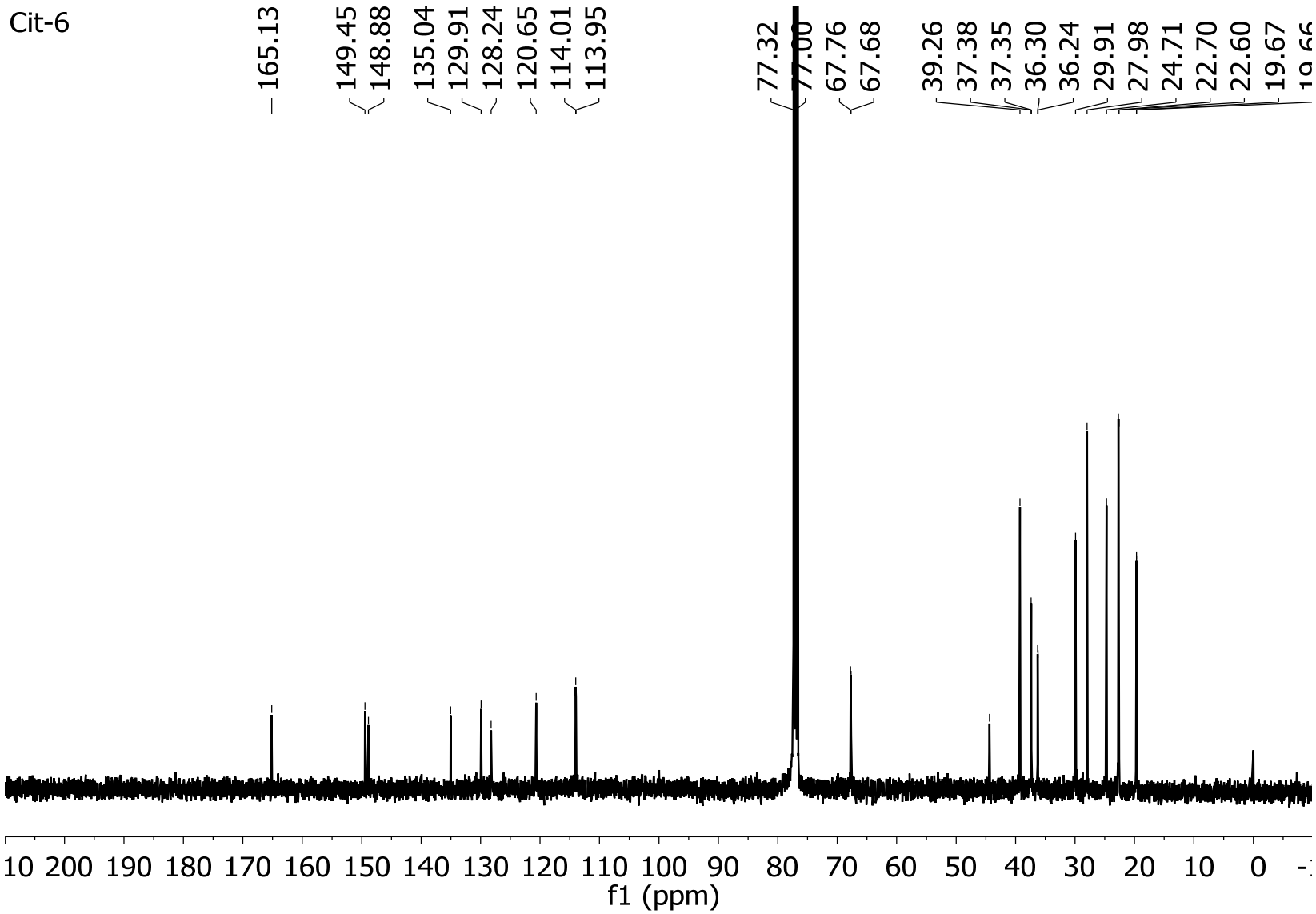
Cit-6
165.13
149.45
148.88
135.04
129.91
128.24
120.65
114.01
113.95
77.32
77.00
67.76
67.68
39.26
37.38
37.35
36.30
36.24
29.91
27.98
24.71
22.70
22.60
19.67
10 200 190 180 170 160 150 140 130 120 110 100 90 80 70 60 50 40 30 20 10 0
f1 (ppm)

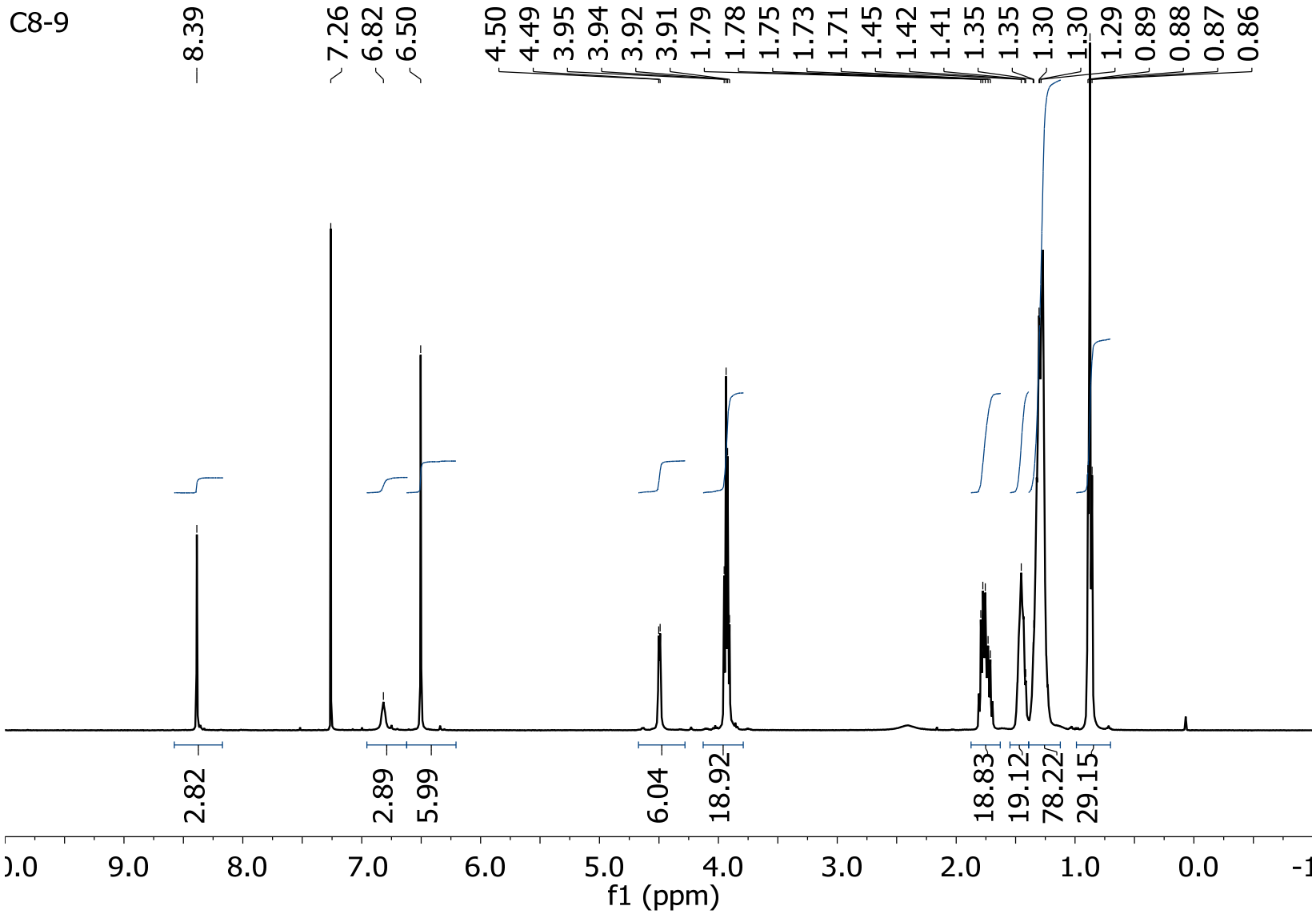
C8-9
8.39
7.26
6.82
6.50
4.50
4.49
3.95
3.94
3.92
3.91
1.79
1.78
1.75
1.73
1.71
1.45
1.42
1.41
1.35
1.35
1.30
1.30
1.29
0.89
0.88
0.87
0.86
2.82
2.89
5.99
6.04
18.92
18.83
19.12
78.22
29.15
9.0
8.0
7.0
6.0
5.0
4.0
3.0
2.0
1.0
0.0
f1 (ppm)

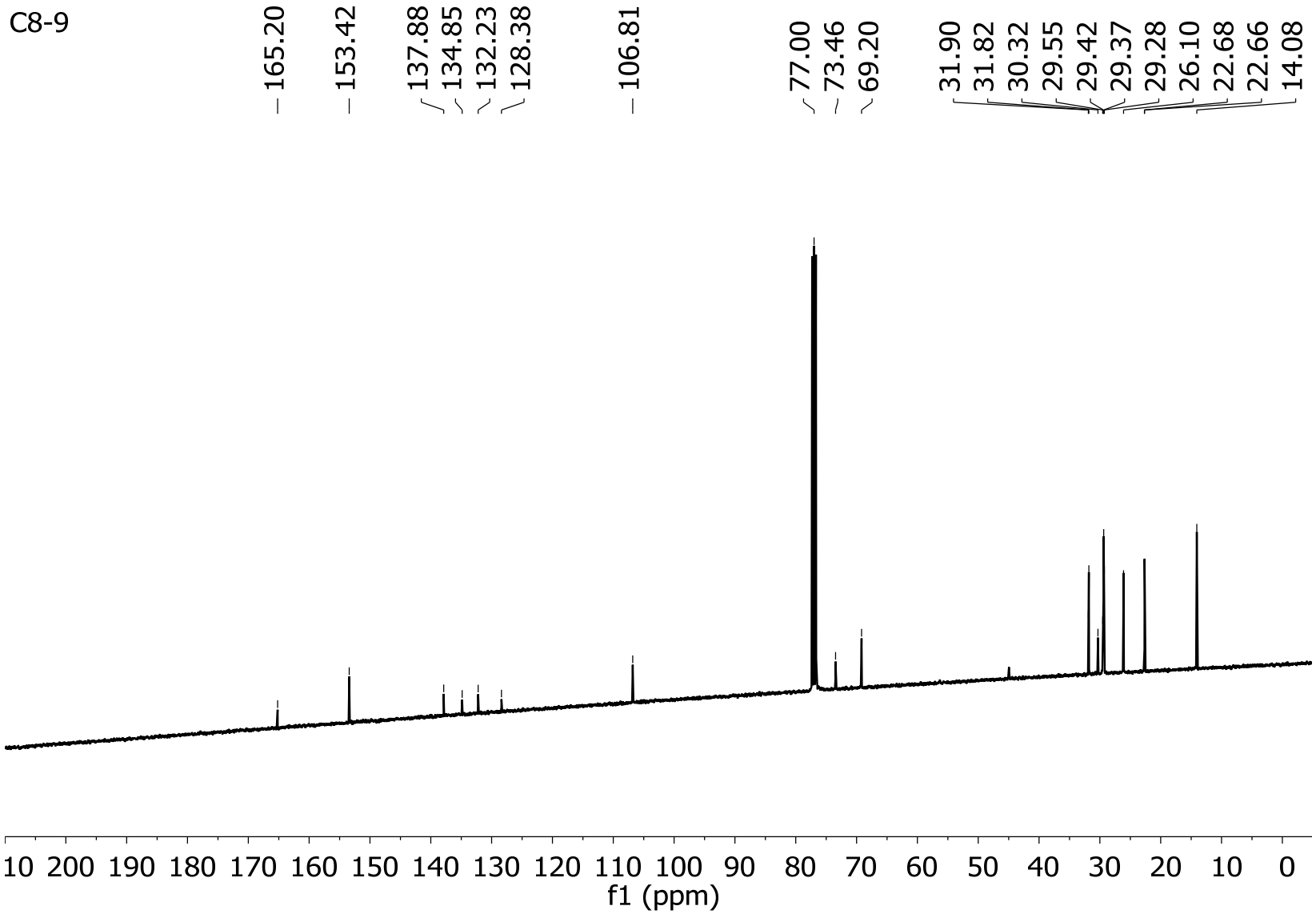
C8-9
165.20
153.42
137.88
134.85
132.23
128.38
106.81
77.00
73.46
69.20
31.90
31.82
30.32
29.55
29.42
29.37
29.28
26.10
22.68
22.66
14.08
10 200 190 180 170 160 150 140 130 120 110 100 90 80 70 60 50 40 30 20 10 0
f1 (ppm)

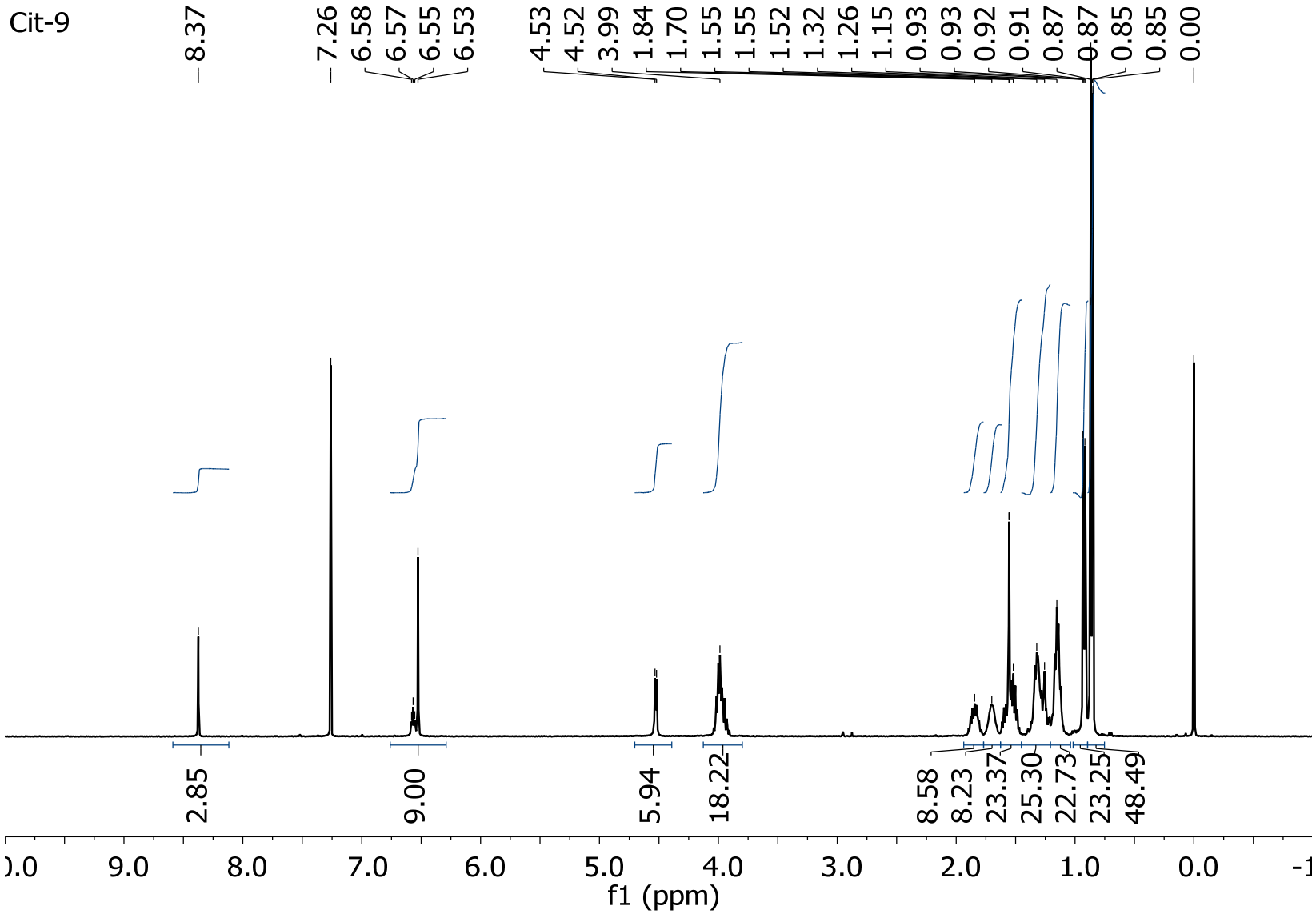
Cit-9
8.37
7.26
6.58
6.57
6.55
6.53
4.53
4.52
3.99
1.84
1.70
1.55
1.55
1.52
1.32
1.26
1.15
0.93
0.93
0.92
0.91
0.87
0.87
0.85
0.85
0.00
2.85
9.00
5.94
18.22
8.58
8.23
23.37
25.30
22.73
23.25
48.49
f1 (ppm)

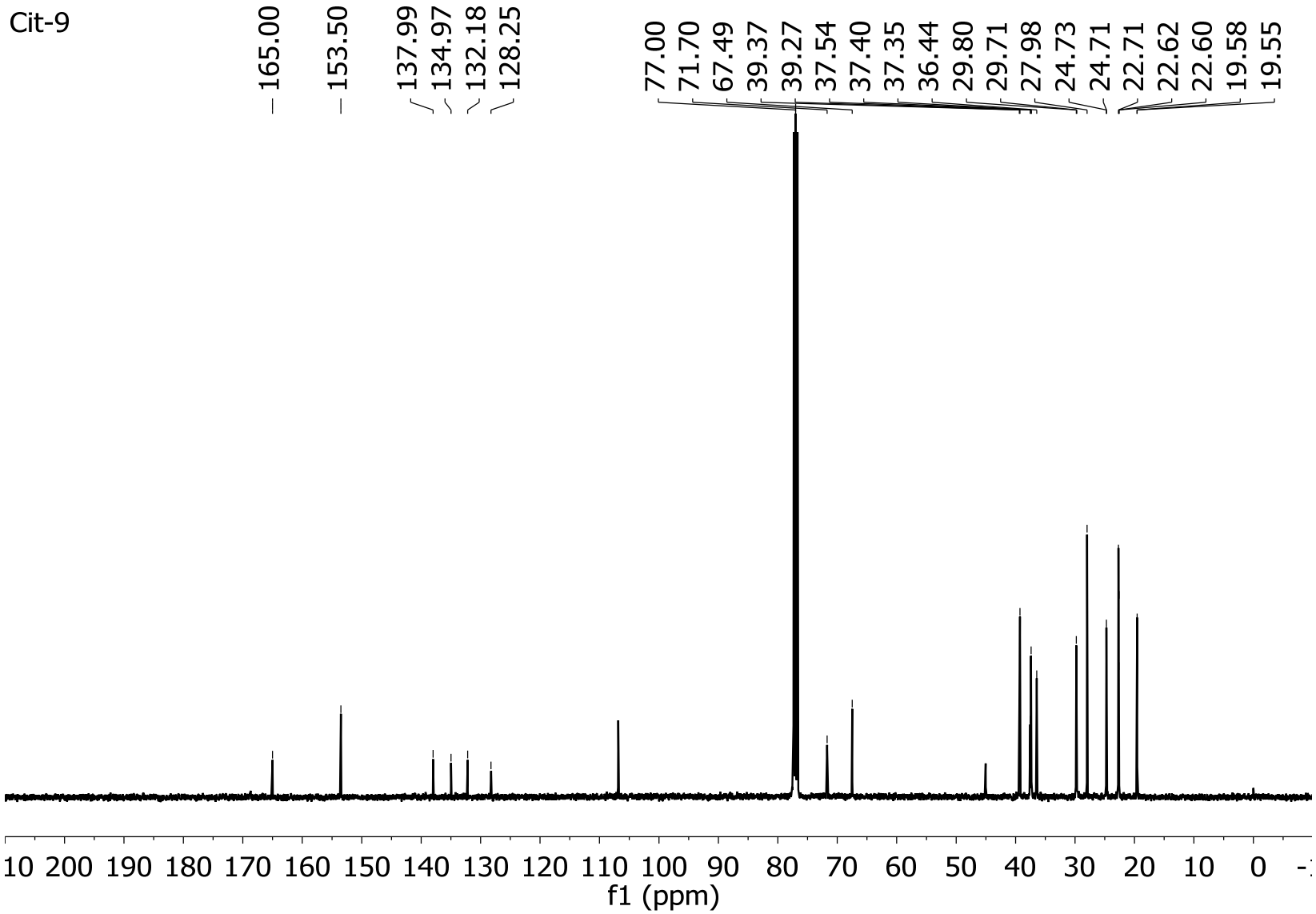
Cit-9
165.00
153.50
137.99
134.97
132.18
128.25
77.00
71.70
67.49
39.37
39.27
37.54
37.40
37.35
36.44
29.80
29.71
27.98
24.73
24.71
22.71
22.62
22.60
19.58
19.55
10 200 190 180 170 160 150 140 130 120 110 100 90 80 70 60 50 40 30 20 10 0
f1 (ppm)

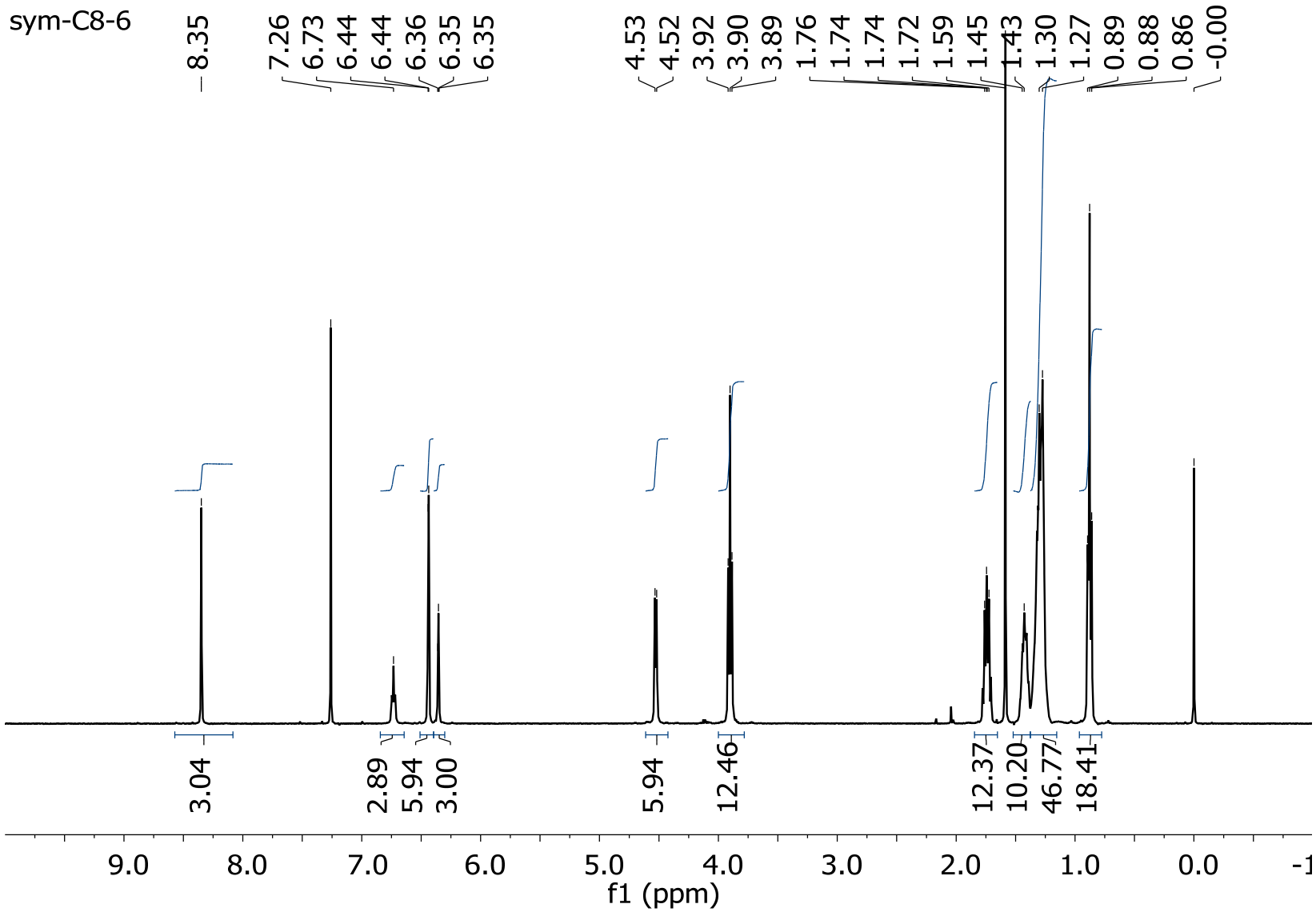
sym-C8-6
8.35
7.26
6.73
6.44
6.44
6.36
6.35
6.35
4.53
4.52
3.92
3.90
3.89
1.76
1.74
1.74
1.72
1.59
1.45
1.43
1.30
1.27
0.89
0.88
0.86
-0.00
3.04
2.89
5.94
3.00
5.94
12.46
12.37
10.20
46.77
18.41
9.0
8.0
7.0
6.0
5.0
4.0
3.0
2.0
1.0
0.0
f1 (ppm)

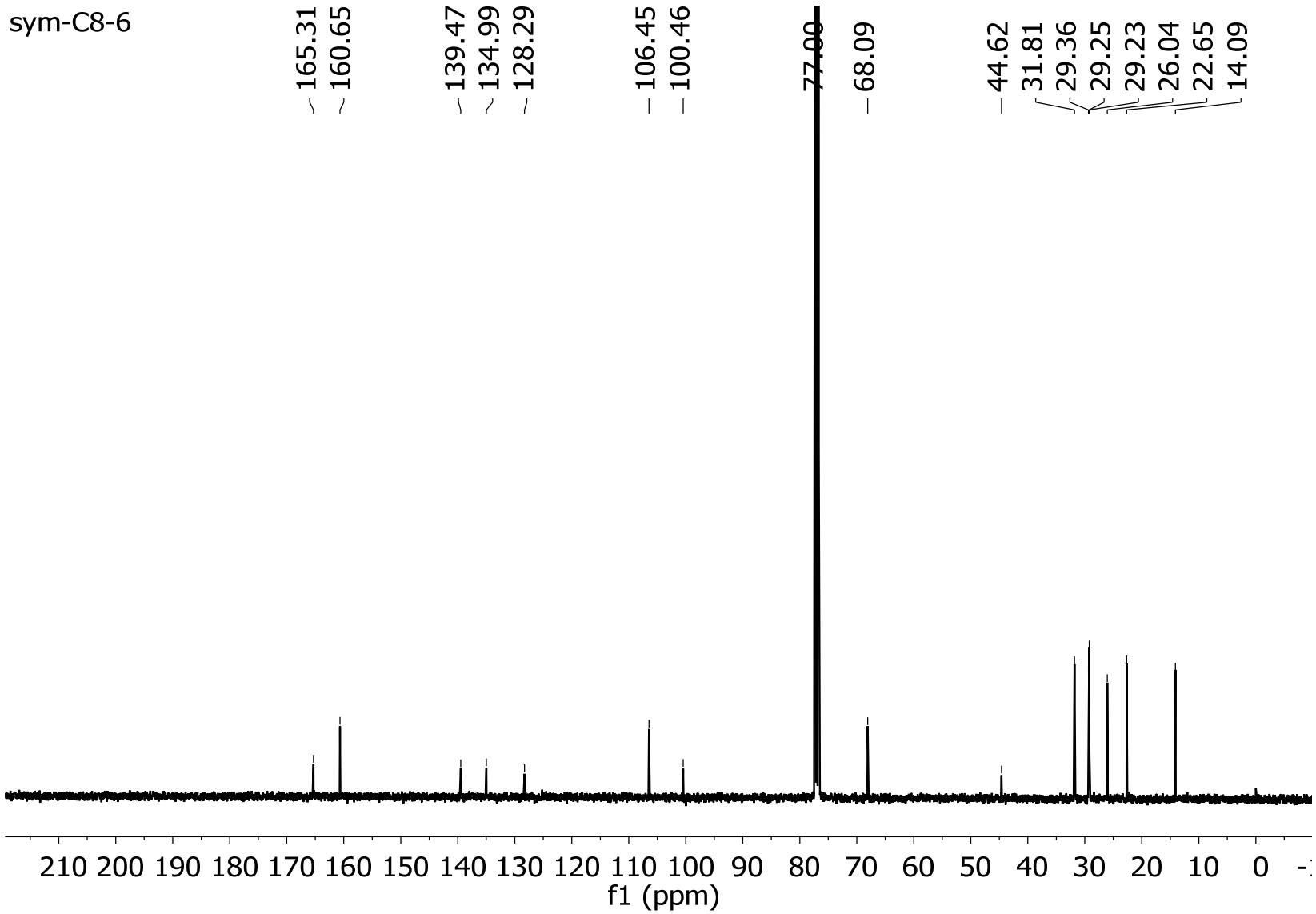
sym-C8-6
165.31
160.65
139.47
134.99
128.29
106.45
100.46
77.00
68.09
44.62
31.81
29.36
29.25
29.23
26.04
22.65
14.09
210 200 190 180 170 160 150 140 130 120 110 100 90 80 70 60 50 40 30 20 10 0
f1 (ppm)

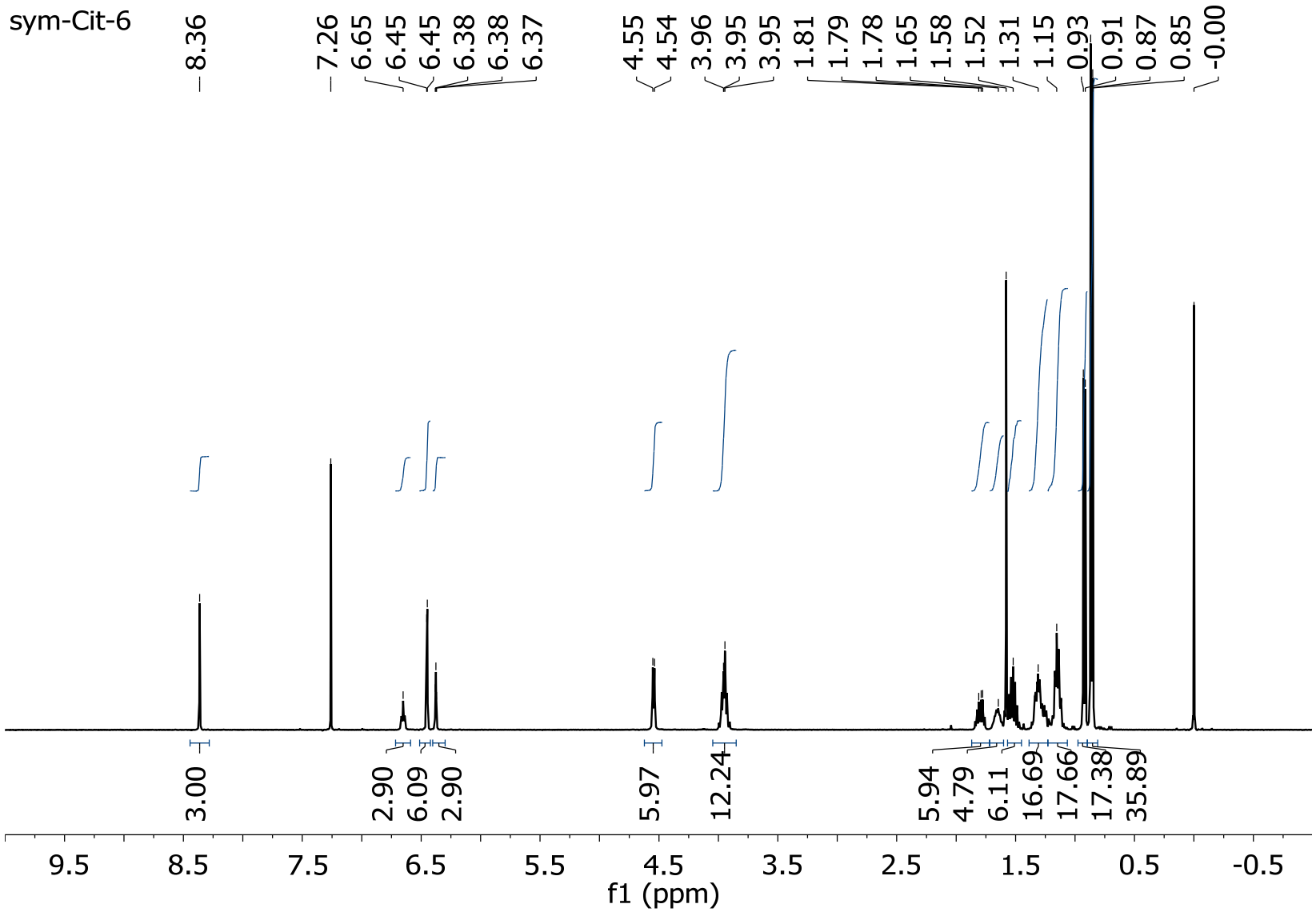
sym-Cit-6
8.36
7.26
6.65
6.45
6.45
6.38
6.38
6.37
4.55
4.54
3.96
3.95
3.95
1.81
1.79
1.78
1.65
1.58
1.52
1.31
1.15
0.93
0.91
0.87
0.85
-0.00
3.00
2.90
6.09
2.90
5.97
12.24
5.94
4.79
6.11
16.69
17.66
17.38
35.89
9.5
8.5
7.5
6.5
5.5
4.5
3.5
2.5
1.5
0.5
-0.5
f1 (ppm)

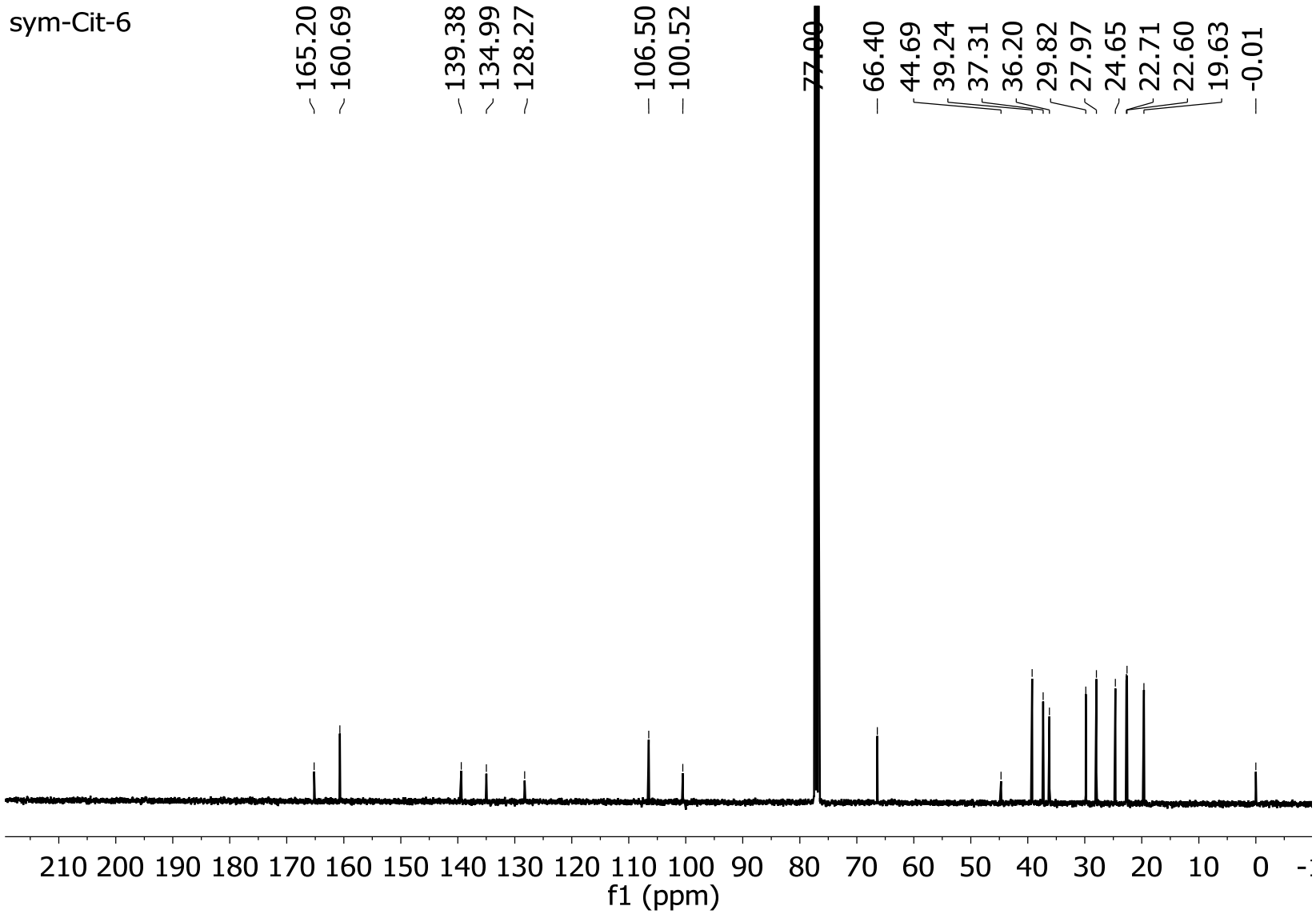
sym-Cit-6
165.20
160.69
139.38
134.99
128.27
106.50
100.52
77.00
66.40
44.69
39.24
37.31
36.20
29.82
27.97
24.65
22.71
22.60
19.63
-0.01
210 200 190 180 170 160 150 140 130 120 110 100 90 80 70 60 50 40 30 20 10 0
f1 (ppm)

DSC thermograms of the BTA derivatives

C8-3

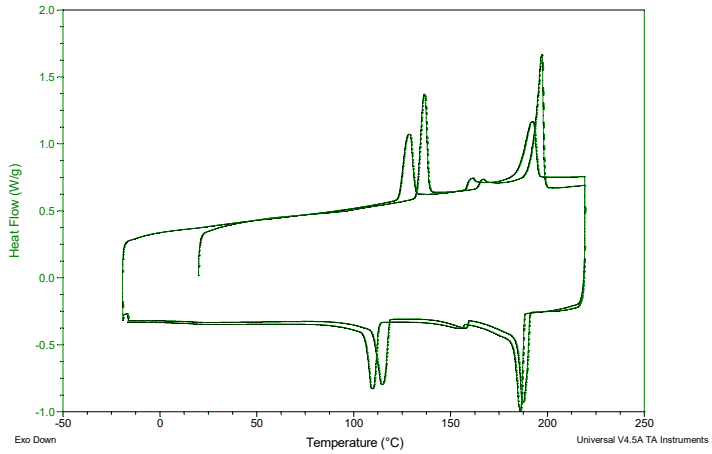

C8-3 1st heating scan

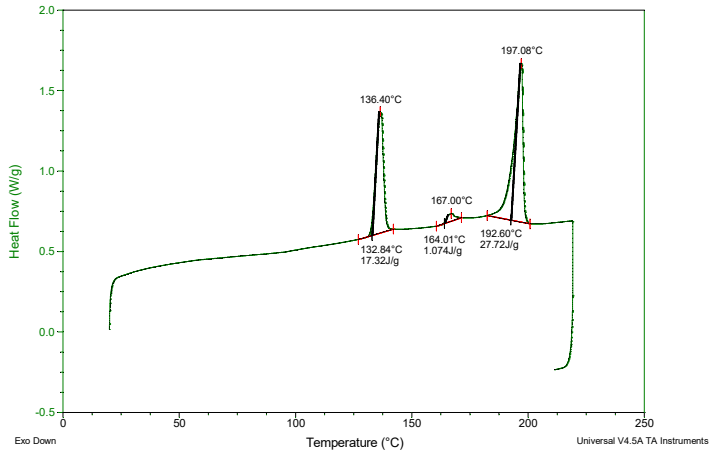

C8-3 1st cooling scan

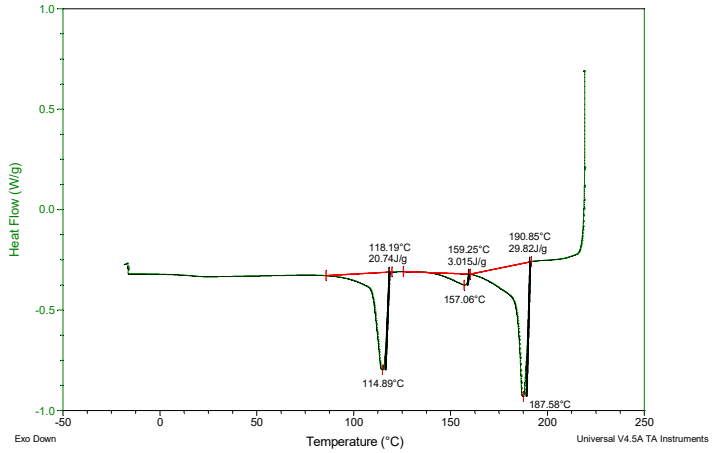

C8-3 2nd heating scan

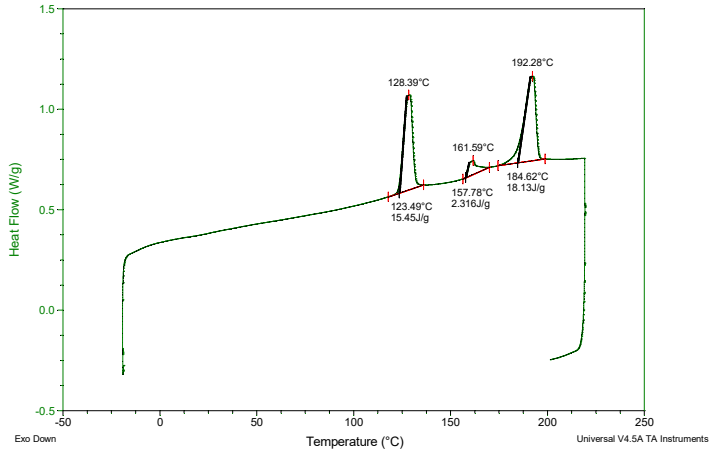

C8-3 2nd cooling scan

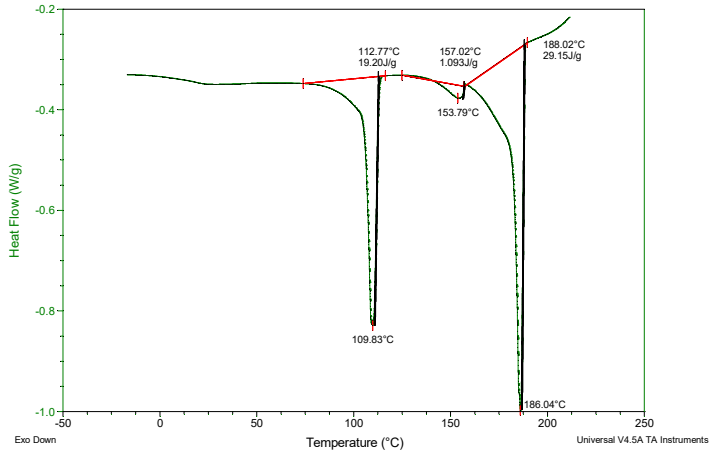

Cit-3

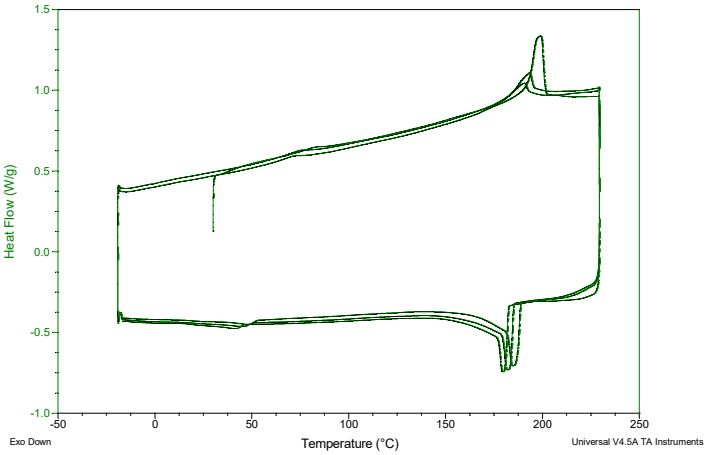

Cit-3 1st heating scan + 1st cooling scan

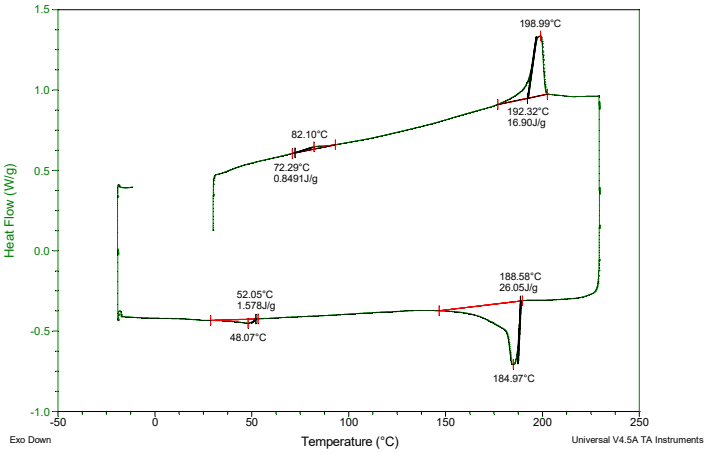

Cit-3 2nd heating scan + 2nd cooling scan

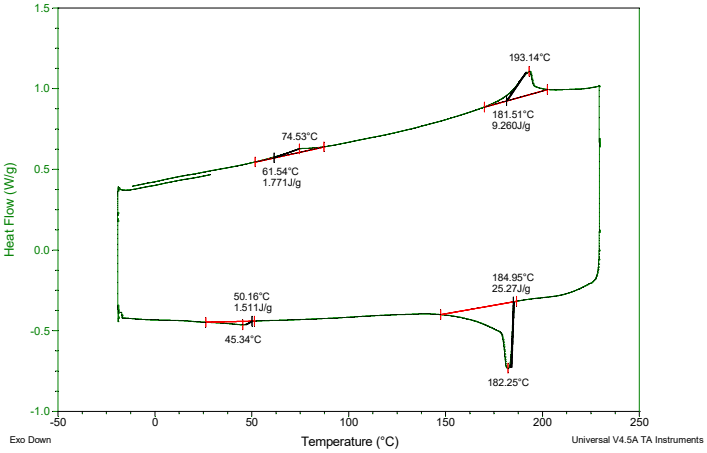

C8-6

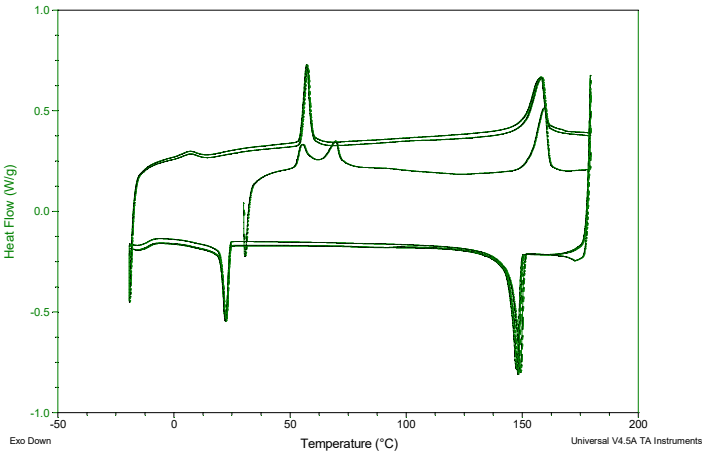

C8-6 1st heating and 1st cooling scan

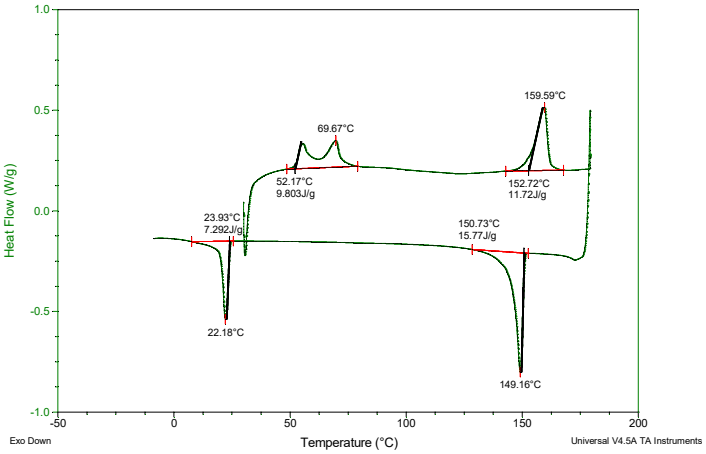

C8-6 2nd heating and 2nd cooling scan

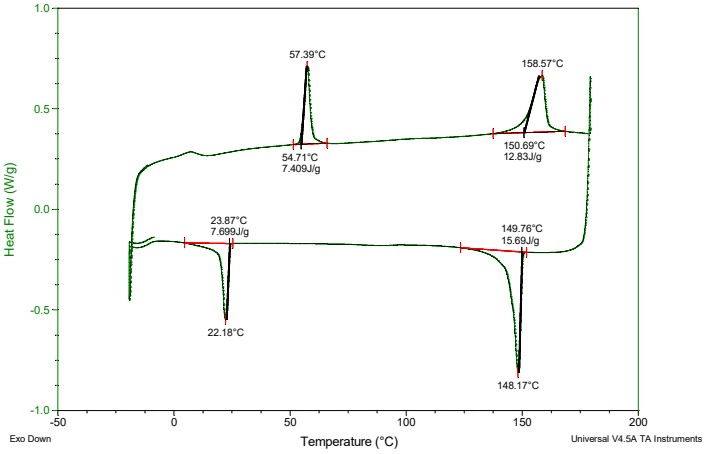

Cit-6

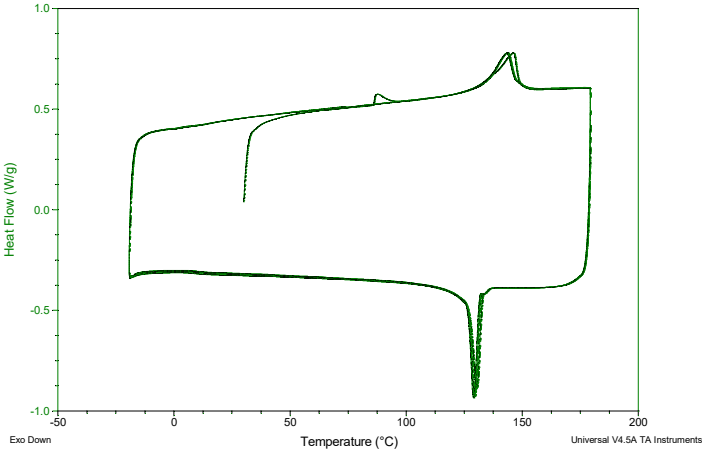

Cit-6 1st heating and 1st cooling scan

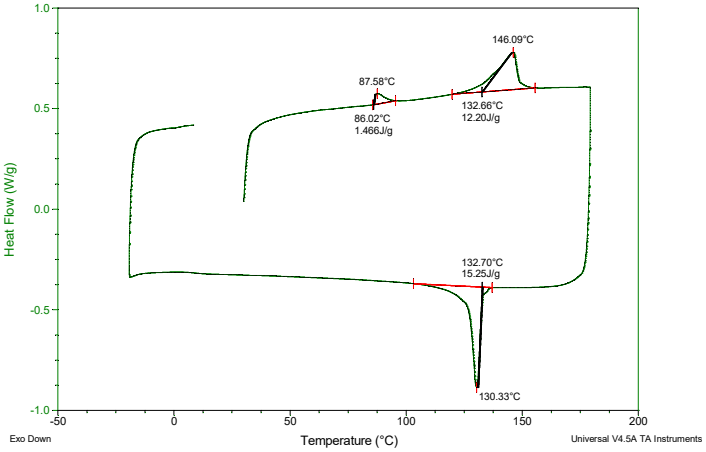

Cit-6 2nd heating and 2nd cooling scan

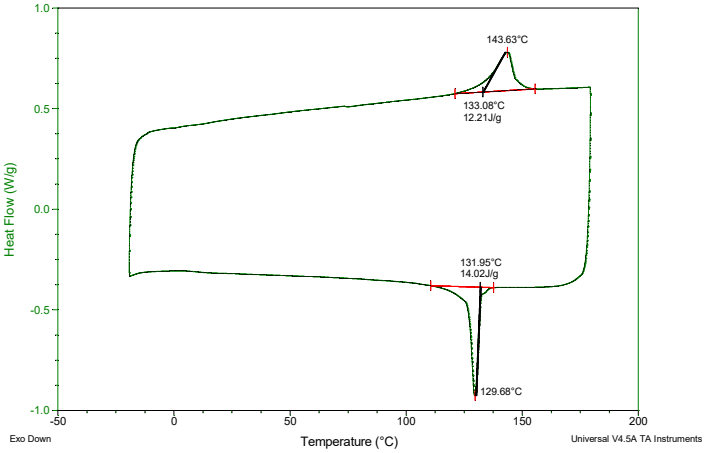

C8-9

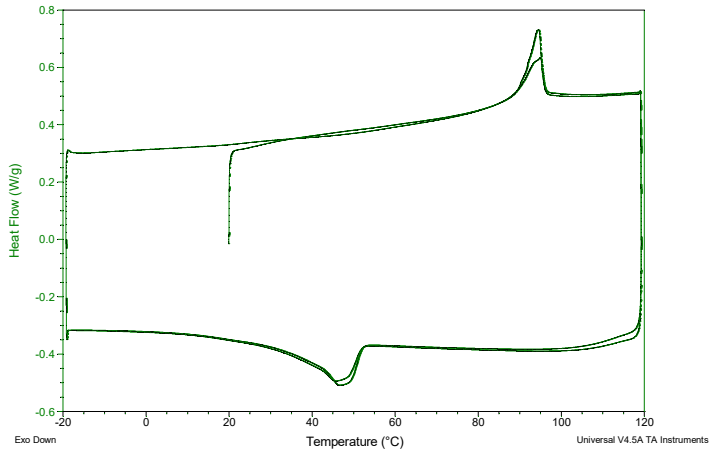

C8-9 1st heating scan and 1st cooling scan

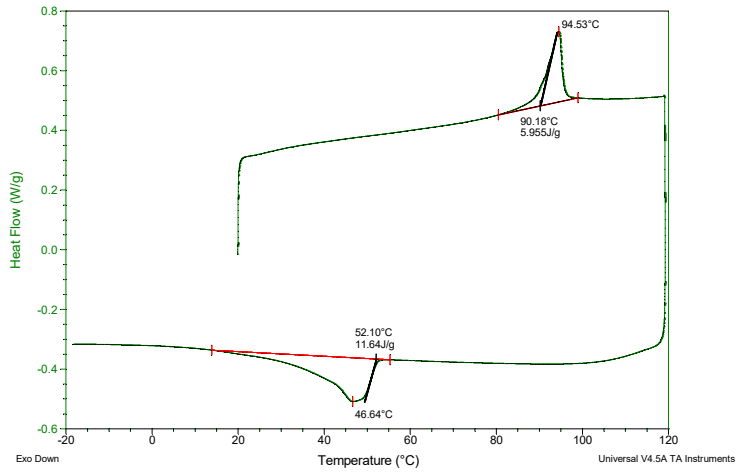

C8-9 2nd heating scan and 2nd cooling scan

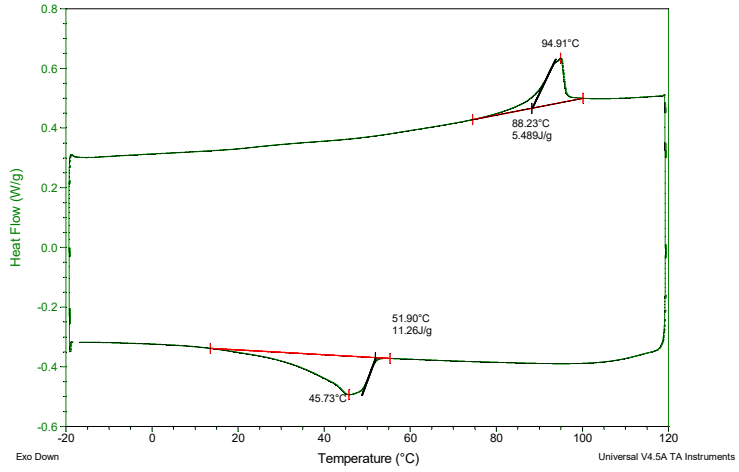

Cit-9

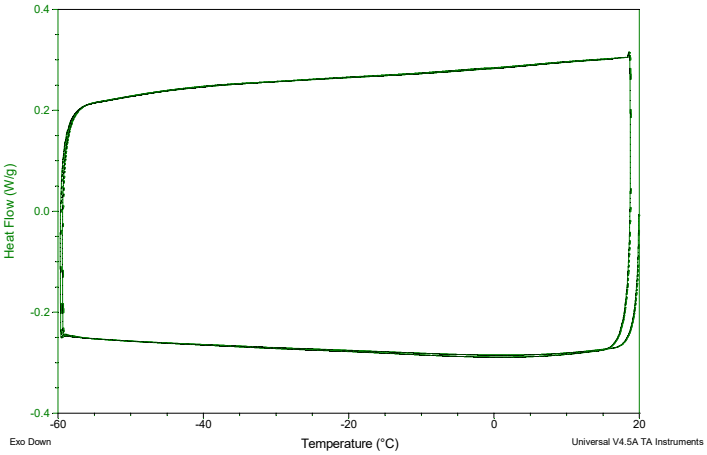
0.4
0.2
0.0
-0.2
-0.4
Heat Flow (W/g)
-60
-40
-20
0
20
Temperature (°C)
Exo Down
Universal V4.5A TA Instruments

Sym-C8-6

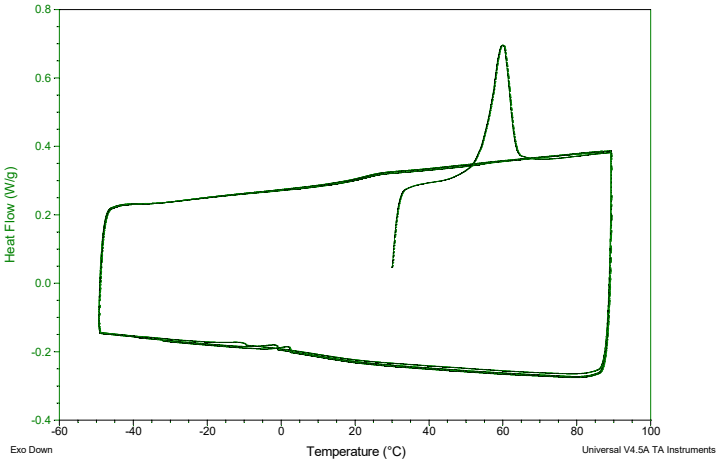

Sym-C8-6 1st heating and 1st cooling scan

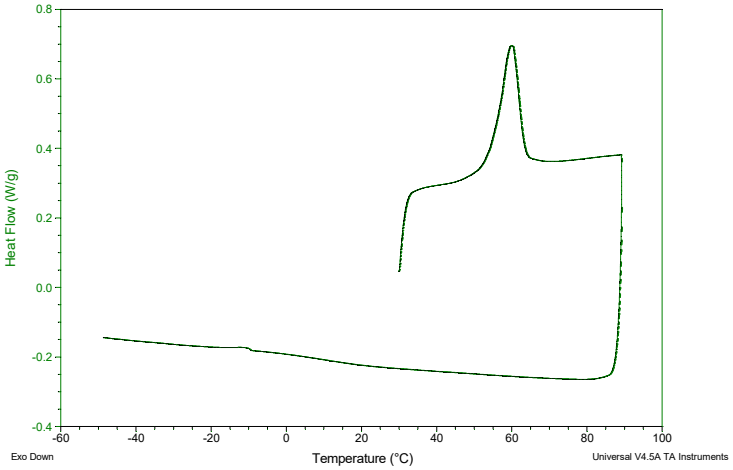

Sym-C8-6 2nd heating and 2nd cooling scan

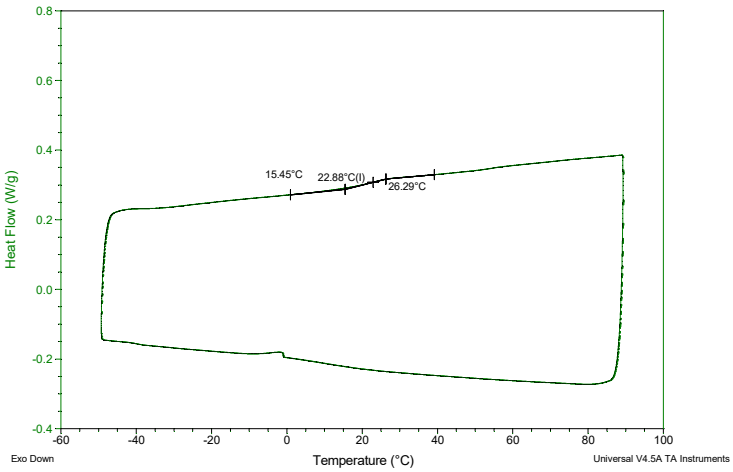

Supplementary references

[1] Klein, M. L., Shinoda, W. *Science,* 2008, **321**, 798–800.
[2] Thayumanavan, S., Pavan, G. M., Amado Torres, D., Subrahmanyam, A. V., Garzoni, M. *J. Am. Chem. Soc.,* 2014, **136**, 5385–5399.
[3] Case, D. A., Betz, R. M., Cerutti, D. S., Cheatham, T. E., Darden, T. A., Duke, R. E., Giese, T. J., Gohlke, H., Goetz, A. W., Homeyer, N., Izadi, S., Janowski, P., Kaus, J., Kovalenko, A., Lee, T.S., LeGrand, S., Li, P., Lin, C., Luchko, T., Luo, R., Madek, B., Mermelstein, D., Merz, K.M., Monard, G., Nguyen, H., Nguyen, H.T., Omelyan, I., Onufriev, A., Roe, D.R., Roitberg, A., Sagui, C., Simmerling, C. L. Swails, J., Walker, R.C., Wang, J., Wolf, R. M., Wu, X., Xiao, L., Kollman, P. A. University of California, San Francisco, 2016.
[4] Dassault Systèmes BIOVIA. Discovery Studio Visualizer Software 4.0., 2012.
[5] Wang, J., Wolf, R. M., Caldwell, J. W., Kollman, P. A., Case, D. A. *J. Comput. Chem.,* **25**, 2004, *56531.*
[6] Jakalian, A., Bush, B. L., Jack, D. B., Bayly, C. I. *J. Comput. Chem.*, 2000, **21**, 132–146.
[7] Jakalian, A., Jack, D. B., Bayly, C. I. *J. Comput. Chem.*, 2002, **23**, 1623–1641.
[8] Wang, J., Wang, W., Kollman, P. A., Case, D. A *J. Mol. Graph. Model.* 2006, **25**, 247–260.
[9] Baker, M. B., Albertazzi, L., Voets, I. K., Leenders, C. M. A., Palmans, A. R. A., Pavan, G. M., Meijer, E. W. *Nat. Commun.*, 2015, **6**, 1–12.
[10] Humphrey, W., Dalke, A., Schulten, K. *J. Molec. Graphics*, 1996, **14**, 33–38.
[11] DeLano, W. L., Version 1.8 Schrödinger, LLC.
[12] Roe, D. R., Cheatham, T. E. J. *Chem. Theory Comput.*, 2013, **9**, 3084–95.
[13] Kumar, P., Bansal, M. J Biomol Struct Dyn., 2012, **30**, 773—783.
[14] Sugeta, H., Miyazawa, T. *Biopolymers*, 1967, **5**, 673–679.
[15] P. J. M. Stals, J. F. Haveman, R. Martín-Rapún, C. F. C. Fitié, A. R. A. Palmans, E. W. Meijer, *J. Mater. Chem.* **2009**, *19*, 124 – 130.
[16] P. J. M. Stals, M. M. J. Smulders, R. Martín-Rapún, A. R. A. Palmans, E.W. Meijer, *Chem. Eur. J.* **2009**, *15*, 2071 – 2080.
[17] H. M. M. ten Eikelder, A. J. Markvoort, T. F. A. de Greef and P. A. J. Hilbers, *J. Phys. Chem. B*, 2012, **116**, 5291–5301.